ABSTRACT

Title of Dissertation:	BRAKE SQUEAL: MODELING AND ENERGY HARVESTING
	Yaqoub Y. Abdullah, Doctoral of Philosophy, 2017
Dissertation directed by:	Professor Amr Baz, Department of Mechanical Engineering

This dissertation aims at developing the fundamentals necessary for mitigating the adverse effect of vibration and noise induced by brake squeal. Such a process is achieved by embedding an array of piezoceramics into the brake system which are provided with shunted electrical networks. These piezoceramic networks offer a unique ability to convert the mechanical energy induced by the brake squeal into electrical energy which can be either harnessed to harvest the squeal energy or dissipated to enhance the damping characteristics of the brake system.

A multi-field finite element model (*FEM*) is developed to simulate the vibration, energy harvesting, and energy dissipation characteristics of a brake/piezoceramic networks assembly. The developed *FEM* is intended to establish the stability limits and the boundaries of the brake squeal of the system in an attempt to optimize the parameters that broadens the operation envelope of the system without the occurrence of the squeal.

The theoretical predictions of the *FEM* are validated against the performance characteristics of an experimental prototype of the system which is capable of reproducing the important features of brake squeal.

It is envisioned that the developed theoretical and experimental methods will present invaluable tools for understanding, analyzing, and mitigating the phenomenon of brake squeal. More importantly, these methods will provide important means for the design of automotive disc brake systems that can operate over broad ranges of operating parameters without experiencing the adverse effects of brake squeal.

BRAKE SQUEAL: MODELING AND ENERGY HARVESTING

by

Yaqoub Y. Abdullah

Dissertation submitted to the Faculty of the Graduate School of the
University of Maryland, College Park, in partial fulfillment
of the requirements for the degree of
Doctoral of Philosophy
2017

Advisory Committee:
Professor Amr Baz, Chair
Professor Balakumar Balachandran
Associate Professor Nikhil Chopra
Assistant Professor Jin-Oh Hahn
Professor Roberto Celi (Dean's Representative)

Dedication

To my family and my wife for their everlasting patience and support and to my beloved children for their never-ending joy they bring to my life.

Acknowledgements

I would like to thank my advisor, Prof. Baz for all the support he has given me during my graduate career. Because of his guidance, I continue to be a better researcher in the field of vibration and damping.

I would also like to acknowledge the University of Maryland supercomputing resources (http://hpcc.umd.edu) made available for conducting the research reported in this dissertation.

I am deeply indebted to my family, my wife and my three adorable children for their sacrifices, prayers, kindness and never-ending love.

Thanks are due to my colleagues Yaser Alsaffar, Mostafa Nouh, Mohammad Raafat, and Mohammad Maqsoud for discussions, suggestions and criticism.

Thanks are also due to Mr. Majid Aroom, Faculty Specialist at University of Maryland Machine Shop, for assisting me with the experimental set-up.

Finally yet importantly, I wish to thank my committee members Dr. Balakumar Balachandran, Dr. Nikhil Chopra, Dr. Jin-Oh Hahn and Dr. Roberto Celi for their support, encouragements and invaluable technical inputs.

Always, it is impossible to remember all, and I apologize to those I have inadvertently left out.

Table of Contents

List of Tables

List of Figures

Chapter 1: Introduction

1.1 Overview

Disc brake squeal remains an elusive problem in the automotive industry due to its immense complexity, despite substantial time and efforts devoted to reducing its occurrence during the past few decades. Even though it does not affect the performance of the brake, the noise decreases the passengers comfort and the subjective quality of the vehicle. The automotive industry also losses substantial revenue from warranty costs due to NVH (noise, vibration and harshness) problems including disc brake squeal. Automotive engines and brakes have greatly developed during the last decades; however, some of the generated mechanical energy from the engine is dissipated during a braking action in the form of heat generation and sound pressure, which is a serious potential squeal problem. Brake squeal mechanisms can result in safety-relevant failures of the brake system. Thus, eliminating squeal becomes one of the top priorities in current brake developments.

1.1.1 Definition of Brake Squeal

Brakes are one of the most important safety and performance components in automobiles. Brake noise causes customer dissatisfaction and has been there since the 1930s [1]. A wide array of brake noise exists in the literature and can be categorized into low frequency and high frequency noise. The low frequency noise includes *groan*, *judder* and *moan*. *Squeal* however, is a high frequency noise and probably the most annoying to both vehicle passengers and environment and is a large factor in warranty

costs. It is generally agreed that brake squeal is a high frequency (over 1 kHz) vibration of brake system components during a braking action. These are meant as a description of brake squeal rather than a definition, as no precise definition has gained complete acceptance [2]. The occurrence of squeal is intermittent and brakes, which are susceptible to squeal, do not do so during every braking operation. For many experimental observations, it is known that squeal usually occurs at slow rotational speeds (0-10 km/hr) towards the end of a stop.

From a theoretical perspective, disc brake squeal can be classified as a friction-induced type of vibration problem and many factors appear to affect squeal occurrence on both macroscopic and microscopic levels such as friction, stiffness, roughness, wear and temperature.

1.1.2 Disc Brake Systems

There are many types of brake systems however, the most popular brake system in modern passengers cars are floating-caliper disc systems. The popularity comes from their simpler design, lighter weight, better braking performance and their ability to dissipate heat through air ventilation. Therefore, reducing brake noise of floating-caliper disc brake systems is of great interest to researchers.

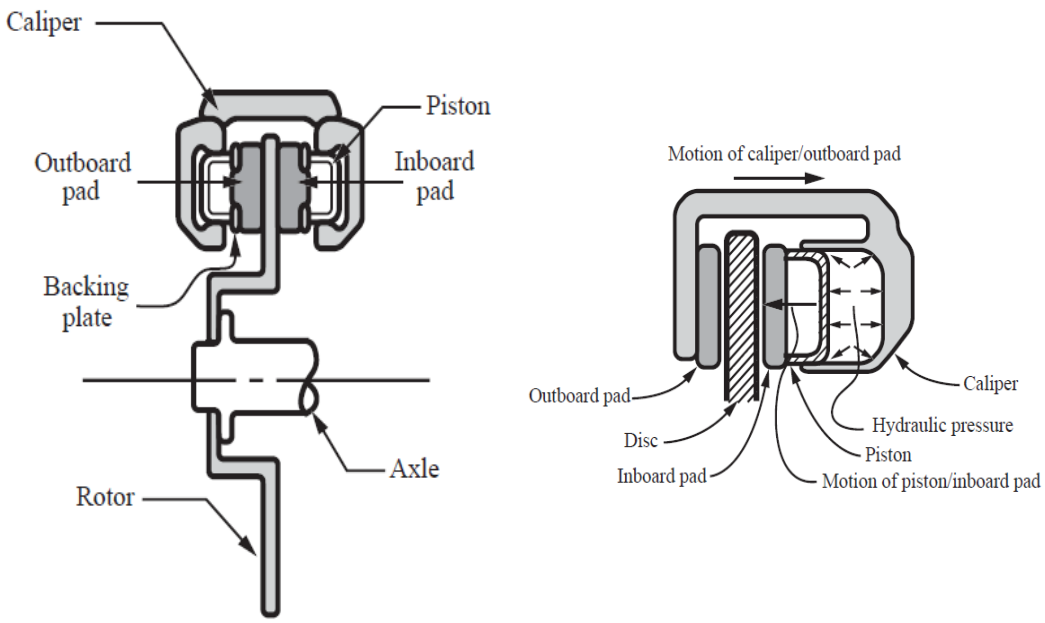

Figure 1.1: Disc brake assembly [2]

A disc brake assembly, such as the one shown in Figure 1.1, is generally consists of four main components: brake disc, caliper, two brake pads, and mounting components. Although brake discs may come in different designs (e.g. solid or vented), most of them have the same basic structure, which is the form of "top-hat" configuration. The brake disc is a rotor that rotates about the axis of the wheel and is usually made of grey cast iron [2]. The disc is designed to bolt into the spindle assembly of the axle hub. The caliper assembly is mounted to the vehicle suspension system through an anchor bracket and is used to hold the two frictional brake pads on either side of the rotor. The brake pads assemblies consists of a friction material which is mounted to a rigid pad backing plate. The mounting is achieved in a variety of manners: using rivets, using adhesives or integrally molding the friction material to the backing

plate [2]. Squeal preventions are also commonly used in the form of dampers (also known as shims) or damping substances, in the contact regions between each of the pad backing plate and the caliper, and the caliper mounting bracket and piston. Friction materials can be considered as composite materials that consist of many components. These components can be divided into five categories: matrix, fibers, metallic particulates, mineral fillers and solid lubricants [2].

During a braking action, the piston movement is controlled hydraulically in which hydraulic pressure pushes the piston in the cylinder forward to press the inner pad against the rotor while the housing is pushed in the opposite direction to press the outer pad against the rotor, which also can be described as generating a braking torque.

1.2 Literature Review

Disc brake squeal is caused by friction-induced vibrations of the brake system components. It has been a challenging problem for many engineers and researchers due to its complexity and many investigators have examined the problem with experimental, analytical, and computational techniques. The literature on disc brake squeal is diverse and it includes the study of friction mechanisms, friction-induced vibrations, self-excited systems, energy dissipation and methods to eliminate or reduce brake squeal. Detailed information on disc brake squeal can be found in the literature reviews conducted by Papinniemi *et al.* [1] in 2002 and Kinkaid *et al.* [2] in 2003. The aim of this literature review is to concentrate on the historical background and the most recent developments in disc brake squeal studies.

1.2.1 Friction Laws and Models

Friction is the non-conservative, surface force acting on bodies which are subject to relative slip or impending slip. The mathematical modeling of the frictional forces acting at the contact interface has a long and rich history and several models have been proposed and developed. These models range from very simple ones such the Coulomb's classical model of friction to very complicated models which take into account "stiction" and presliding displacement. However, most friction models commonly used in the modeling of disc brake squeal describe the friction coefficient as a function of the relative velocity of the two contact surfaces. This class of friction models is often called "static friction models". Coulomb's classical model of friction is commonly adopted in studies on brake squeal [2].

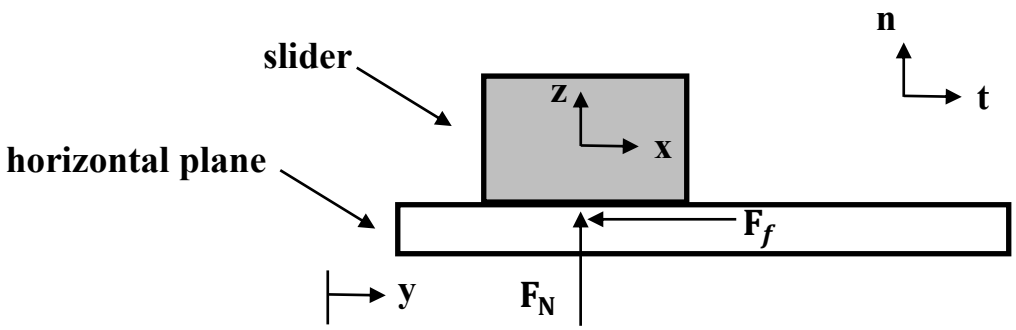

Figure 1.2: Classical model of friction

In this section, the classical model of friction is reviewed. Figure 1.2 shows the classical model of friction where the displacement of a slider on a horizontal foundation is assumed planar and equal to $x(t)\mathbf{t}$, while the displacement of the foundation is $y(t)\mathbf{t}$.

The resultant normal force is denoted by $\vec{\mathrm{F}}_{\boldsymbol{N}} = F_N\mathbf{n}$. The sliding velocity of the slider is $v_s = \dot{x} - \dot{y}$, and the resultant friction force on the slider is $\vec{\mathrm{F}}_f = F_f\mathbf{t}$.

This classical model takes into account Amontons's laws of friction and Coulomb's observation. Amontons' two laws of friction [3], are (i) F_f is independent of the contact area A and (ii) F_f is directly proportional to the normal force F_N. As a consequence of his second law, the coefficient of kinetic friction μ_k is independent of the normal force F_N. Coulomb [4] showed that μ_k could depend on v_s which is the belief that the static coefficient of friction μ_s is greater than μ_k. The relationship of the friction force and the sliding velocity $\vec{\mathrm{v}}_{\mathrm{s}} = v_s\mathbf{t}$ is expressed as

$$\vec{\mathrm{F}}_f = F_f\mathbf{t} = -\mu_k\, F_N\, \frac{\vec{\mathrm{v}}_{\mathrm{s}}}{|\vec{\mathrm{v}}_{\mathrm{s}}|} \tag{1.1}$$

The negative sign in equation (1.1) indicates that the friction force opposes the relative motion and that the magnitude of the friction force is proportional to the normal load and its direction depends on the direction of the relative velocity of the two contact surfaces. The constant of proportionality μ_k is traditionally plotted against the relative velocity as in Figure 1.3.

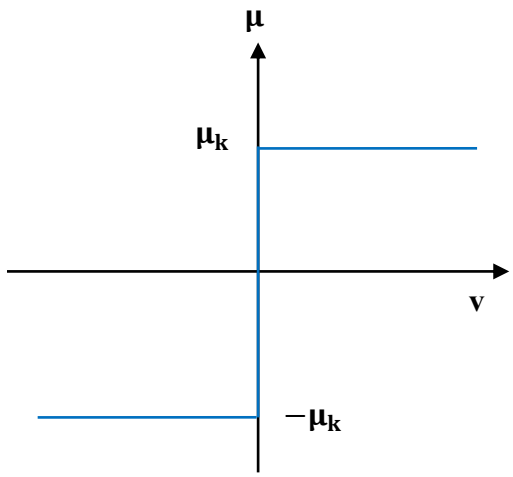

Figure 1.3: Coefficient of friction vs. velocity

1.2.2 Friction-Induced Vibrations

The subject of squeal vibrations is a subset of a larger class of problems known as “friction-induced vibrations”. The basic concept of these problems is the transfer of energy of one surface sliding on another which can result in vibrations in one or both bodies. Systems that exhibit this type of vibrations are termed as “self-excited systems” since no external loads are applied. The friction-induced vibrations are considerably different in character to the more commonly studied forced vibrations. In 1994, Ibrahim [5, 6] published two very comprehensive review papers on the subject. A non-conservative follower (circulatory) force which depends on the displacements of a system but which cannot be derived from a potential energy associated with these displacements causes self-excited vibrations [7].

There are many different types of mechanisms that can lead to friction-induced vibrations. The most commonly used in the context of brake squeal are stick-slip and

Sprag-slip oscillations. This study is about stick-slip oscillations mechanism and a brief description is given in this section. The effect of the negative slope of the friction velocity curve will also be covered in this section.

The stick-slip phenomenon of friction is observed experimentally in sliding systems. As the name implies, stick-slip oscillations are characterized by motion during which intermittent periods of sticking and of slipping between two surfaces exist. During the sticking phase of motion, the moving surface is able to transmit energy into the body of the otherwise stationary surface (in the form of strain energy in the body). During the slipping phase of motion, the friction force opposes the relative motion thereby dissipating energy in the system. Steady-state oscillations arise for the system when system conditions are such that the energy (per cycle) during the sticking phase balances the energy dissipated (per cycle) during the slipping phase. A simple system shown in Figure 1.4 was first studied by Den-Hartog in 1931 [8] and is commonly used to demonstrate “stick-slip” oscillations.

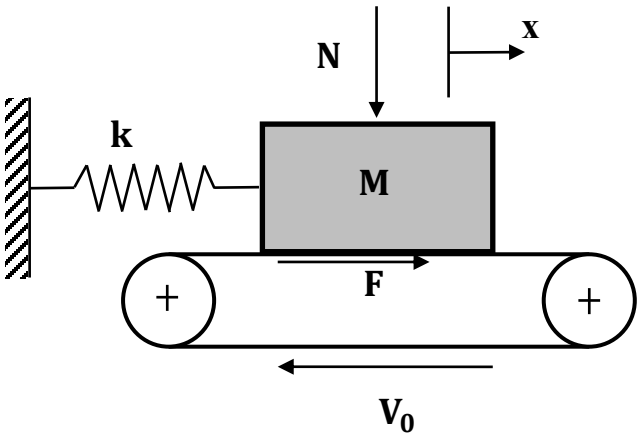

Figure 1.4: Simple elastic rubbing system

The figure shows a mass M attached to the ground via a spring of stiffness k slides on a belt moving at a constant velocity V_0. This model is characterized by a constant coefficient of friction while sliding but a higher value while sticking. During slipping phase, the equation of motion is

$$M\ddot{x} + kx = \mu_k N \tag{1.2}$$

During sticking phase, the equation of motion is

$$\dot{x} = V_0 \tag{1.3}$$

The earliest research into brake squeal suggested that the variation in the friction coefficient with sliding velocity was the cause [9]. It was commonly believed that the drop in kinetic friction with increased sliding velocity could lead to a stick-slip condition (also known as the negative slope of the friction-speed curve) and produce self-excited vibration. In this case, the coefficient of friction as a function of the relative slip velocity is given as

$$\mu_k = \mu_s \left[1 - \lambda(V_0 - \dot{x})\right] \tag{1.4}$$

where λ is the magnitude of the slope of friction-speed curve (a positive value), as illustrated in Figure 1.5.

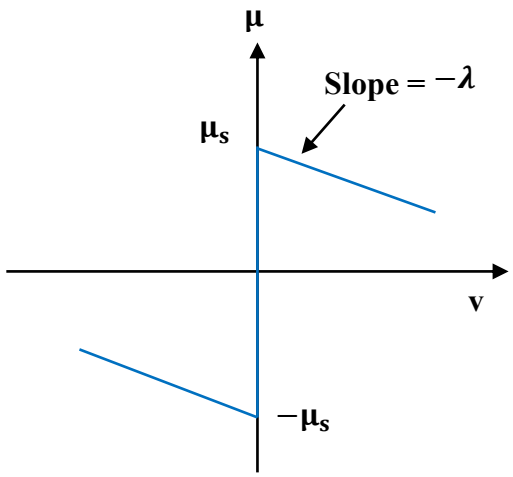

Figure 1.5: Negative friction slope

The equation of motion of the rubbing block can be written as

$$M\ddot{x} + kx = \mu_s N[1 - \lambda(V_0 - \dot{x})] \tag{1.5}$$

This equation can be re-arranged as

$$M\ddot{x} - \lambda\mu_s N\dot{x} + kx = \mu_s N(1 - \lambda V_0) \tag{1.6}$$

Since the value of λ is always positive, equation (1.6) has a negative damping term and, thus the system becomes unstable. As a result, the negative slope of the friction speed curve gives a mechanism for instability generation. However, many experimental observations show that squeal can occur in brake systems where the coefficient of kinetic friction is constant such as in the work of Hulten [10]. Eriksson *et al*. [11] and Chen *et al*. [12] also concluded that there is no correlation of squeal and negative slope of the friction curve in their experiments.

The friction coefficient μ_k in the contact region between the pads of friction material and the brake rotor was found, using brake dynamometer tests, to range from 0.2 to above 0.6 in the literature [2]. It should be noted that these values are not valid pointwise throughout the contact region between the pads of friction material and the brake rotor. Rather, they are average values for both pads. Finite element-based predictions of the interface pressure and friction forces in disc brakes can be found in papers [13, 14, 15] in which it was clear that neither of these fields are uniform.

1.2.3 Minimal Models for Disc Brake Squeal

Numerous publications on the modeling of disc brake squeal can be found in the literature. This includes but not limited to the model of Jarvis and Mills (1963), the pin-on-disc system of Earles *et al.* (1971-1987), North's models (1972, 1976), Millner's model (1978), the 12-degree-of-freedom model by Brooks *et al.* (1993), the finite element model by Ouyang *et al.* (1999-2000) and the model of Chowdhary *et al.* (2001) [2]. Due to the complexity of the problem, many researchers introduced minimal models of two-degree-of-freedom that describe the basic behavior of disc brake squeal which can easily be associated to an automotive disc brake. Recent examples of models are the work of Shin *et al.* (2002), the model by Hoffmann and Gaul (2002) and the model by Popp *et al.* (2002). The review of the previous minimal models and a new two-degree-of-freedom model can be found in Ref. [16] by Wagner, Hochlenert and Hagedorn.

In this section, the model by Hoffmann *et al.* [17] is reviewed to clarify the physical mechanisms underlying disc brake squeal. The model is analyzed with respect to its stability behavior and is shown in Figure 1.6.

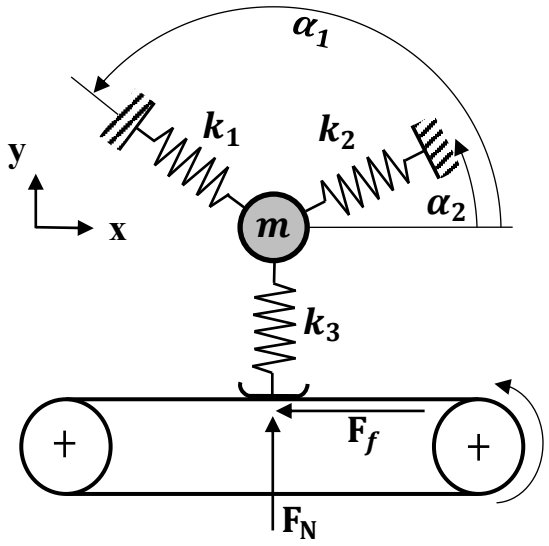

Figure 1.6: Minimal model by Hoffmann *et al.*

A conveyor belt with constant velocity v_B is pushed with constant normal force F_N against a block modeled as a particle m. The block is held in position by two linear springs with stiffness k_1 and k_2 and there is a linear spring k_3 which may be taken as a model for the normal contact stiffness between the block and the moving belt. A Coulomb-type friction force F_f with constant friction coefficient μ, is assumed. This model constitutes a two-degree-of-freedom generalization of the one-degree-of-freedom model well known from general studies on stick-slip. The equation of motion of the system is given as

$$\begin{bmatrix} m & 0 \\ 0 & m \end{bmatrix} \begin{Bmatrix} \ddot{x} \\ \ddot{y} \end{Bmatrix} + \begin{bmatrix} k_{11} & k_{12} \\ k_{21} & k_{22} \end{bmatrix} \begin{Bmatrix} x \\ y \end{Bmatrix} = \begin{Bmatrix} F_f \\ F_N \end{Bmatrix} \tag{1.7}$$

where the coefficients of the stiffness matrix are

$$k_{11} = k_1 \cos^2 \alpha_1 + k_2 \cos^2 \alpha_2$$

$$k_{12} = k_{21} = k_1 \, sin \, \alpha_1 \cos \alpha_1 + k_2 \, sin \, \alpha_2 \cos \alpha_2$$

$$k_{22} = k_1 \sin^2 \alpha_1 + k_2 \sin^2 \alpha_2 + k_3$$

Considering small perturbations around the steady sliding state and approximating the friction force by $F_f = \mu k_3 y$ the resulting system of equations of motion are

$$\begin{bmatrix} m & 0 \\ 0 & m \end{bmatrix} \begin{Bmatrix} \ddot{x} \\ \ddot{y} \end{Bmatrix} + \begin{bmatrix} k_{11} & k_{12} - \mu k_3 \\ k_{21} & k_{22} \end{bmatrix} \begin{Bmatrix} x \\ y \end{Bmatrix} = \begin{Bmatrix} 0 \\ 0 \end{Bmatrix} \tag{1.8}$$

The generalized coordinates x and y will also be called in-plane and out-of-plane displacements respectively to simplify the notation for this study.

In general, a system with a symmetric and positive definite mass matrix ($\mathbf{M^T} = \mathbf{M} > 0$), and a symmetric and positive definite stiffness matrix ($\mathbf{K^T} = \mathbf{K} > 0$) have all eigenvalues purely imaginary and the system is therefore stable in the sense of Lyapunov. However, in this model, the circulatory force results in a non-symmetric system's stiffness matrix ($\mathbf{K^T} \neq \mathbf{K}$). For certain conditions, the current model can have an unstable mode which will grow exponentially in time. The authors [17] provided a special case for instability, which is

$$m = 1 \, kg \, , k_1 = 0.18 \, N/m \, , k_2 = 2.49 \, N/m \, , k_3 = 1.33 N/m,$$

$$\alpha_1 = 150^o, \alpha_2 = 30^o \; and \; \Delta = \mu k_3$$

The system equations are then

$$\begin{bmatrix} 1 & 0 \\ 0 & 1 \end{bmatrix} \begin{Bmatrix} \ddot{x} \\ \ddot{y} \end{Bmatrix} + \begin{bmatrix} 2 & 1 - \Delta \\ 1 & 2 \end{bmatrix} \begin{Bmatrix} x \\ y \end{Bmatrix} = \begin{Bmatrix} 0 \\ 0 \end{Bmatrix} \tag{1.9}$$

The solution to equation (1.9) is assumed as

$$\begin{Bmatrix} x \\ y \end{Bmatrix} = \begin{Bmatrix} X \\ Y \end{Bmatrix} e^{st} \tag{1.10}$$

where s is Laplace complex number. The roots of the characteristic equation are

$$s_{1,2} = \pm\left[-2 \pm \sqrt{1-\Delta}\right]^{\frac{1}{2}} \tag{1.11}$$

The roots of equation (1.11) are complex in which for $\Delta < 1$ there are two normal undamped modes with different frequencies and the system is always stable. For the case of $\Delta = 1$, the frequencies coalesce and the system is also stable. However, for the case of $\Delta > 1$, a pair of unstable and a stable mode results and the system is therefore unstable. This type of instability is often termed as "mode-coupling" type instability.

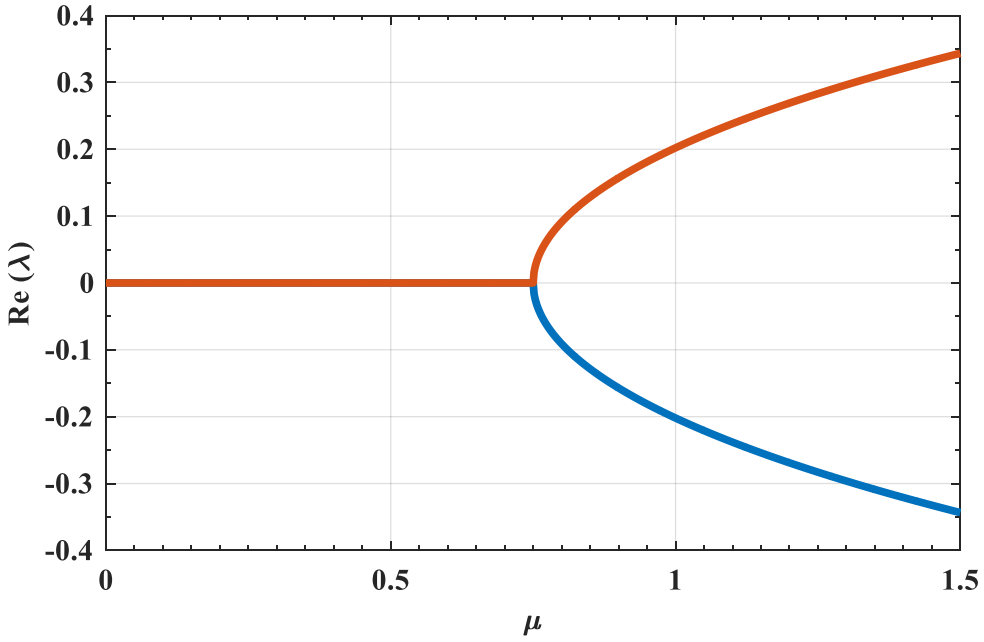

Figure 1.7: Stability of minimal model modes

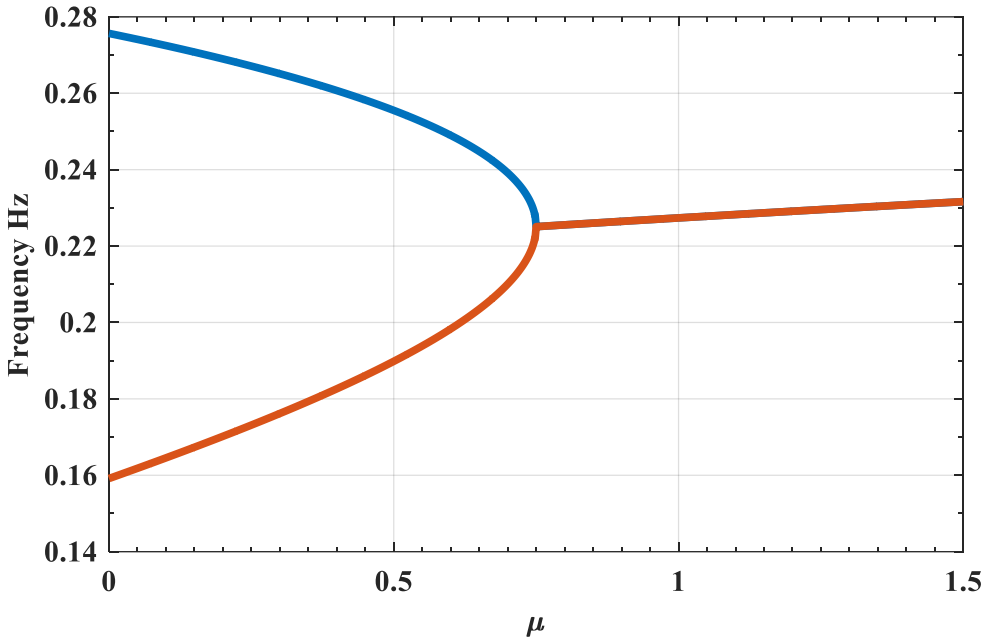

Figure 1.8: Mode-coupling behavior of self-excited systems

Figures 1.7 and 1.8 show the mode-coupling phenomenon in terms of the merging of natural frequencies and the appearance of positive real parts for $\Delta > 1$. This model has shown that the friction force acts like a structural cross-coupling force linking out-of-plane motion to the in-plane motion and that mode-coupling type instability results if these friction-induced cross-coupling forces balance the corresponding cross-coupling forces of the structural system.

1.2.4 Modeling of Brake Discs

Figure 1.9: Tophat brake disc by BOSCH

Typical brake discs usually come in the form of a top-hat structure as shown in Figure 1.9. Although, their actual shapes and sizes may vary depending on the operation requirements, the basic structure of most brake discs consists of two simple components namely (i) an annular disc and (ii) a cylinder. The models for the rotor display the greatest diversity. Hultén and Flint [18] modeled the disc rotor as a beam. Hagedorn *et al.* [19, 20, 21, 22, 23, 16, 24, 25, 26], Kang *et al.* [27, 28, 29] and Mottershead [30] modeled the brake disc as an axisymmetric thin annular Kirchhoff plate. Finite element modeling of three-dimensional top-hat brake disc is also shown in the work of Cao *et al.* [31], Ouyang and Mottershead [32] and Kang [33, 34, 35, 36].

Although, the generation of squeal noise may involve the whole disc brake assembly, it is the brake disc that can radiate squeal noise most effectively because of

its relatively large surface area. Hence, to gain a better understanding of the brake squeal phenomenon, it is convenient to study the vibration of the disc brake thoroughly.

In this study, the brake disc is modeled as an axisymmetric thin annular Kirchhoff plate, which show a good description for the dynamic behavior with regard to squeal when compared to experimental work [19]. The brake disc is assumed to have in-plane and out-of-plane deformations however, this study is only limited to transverse (out-of-plane) vibrations. Furthermore, the annular plate is subjected to clamped boundary condition at inner radius and free boundary condition at outer radius. A simplified model of annular plate is shown in Figure 1.10.

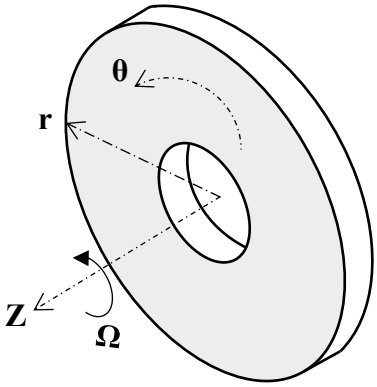

Figure 1.10: Simple annular plate

The classical equation of motion for the transverse displacement $w_0(r,\theta,t)$ of a rotating annular Kirchhoff plate is given in Ref. [19, 21, 22] as

$$\rho h \frac{\partial^2 w_0}{\partial t^2} + 2\rho h\Omega \frac{\partial^2 w_0}{\partial \theta\, \partial t} + D\nabla^4 w_0 = q(r,\theta,t) \tag{1.12}$$

where

$$\nabla^4 = \left(\frac{\partial^2}{\partial r^2} + \frac{\partial}{r\partial r} + \frac{\partial^2}{r^2\partial\theta^2}\right)^2 \tag{1.13}$$

$$D = \frac{Eh^3}{12(1-\nu^2)} \tag{1.14}$$

and ρ is the mass density, E is Young's modulus, h is the thickness, ν is Poisson ratio of the plate. Ω represents the constant rotating speed around the Z-axis and $q(r,\theta,t)$ represents the contribution of external forces and moments.

In the absence of loadings due to brake pad assemblies $q(r,\theta,t) = 0$ and ignoring the Coriolis effects, equation (1.12) reduces to

$$\rho h \frac{\partial^2 w_0}{\partial t^2} + D\nabla^4 w_0 = 0 \tag{1.15}$$

which is considered as the free vibration case of a stationary annular plate. The general solution to equation (1.15) is a double infinite sum of eigenmodes and is expressed in polar coordinates as

$$w_0(r,\theta,t) = \sum_{m=0}^{\infty}\sum_{n=0}^{\infty} R_{mn}(r)\,[\mathrm{A_{mn}}(t)\cos(n\theta) + \mathrm{B_{mn}}(t)\sin(n\theta)] \tag{1.16}$$

where $R_{mn}(r)$ are Bessel functions obtained from the solution of the eigenvalue problem and $\mathrm{A_{mn}}(t)$, $\mathrm{B_{mn}}(t)$ are generalized coordinates characterizing the vibrations of the discretized brake disc. m represents the nodal circles and n is the nodal diameters

of the mode. It should be noted here that most researchers such as Hagedorn *et al.*, Kang *et al.,* Ouyang and Mottershead believe that disc brake squeal is induced by transverse doublet modes of the brake disc which for the case of perfectly axisymmetric disc should have an identical frequency. A doublet mode is member of pair modes having the same frequency and the same number of non-zero n nodal diameters and m nodal circles.

Considering the case of doublet modes with zero nodal circles $(m = 0)$, the general solution in equation (1.16) becomes

$$w_0(r,\theta,t) = \sum_{n=1}^{\infty} R_n(r)\,[\mathrm{A_n}(t)\cos(n\theta) + \mathrm{B_n}(t)\sin(n\theta)] \qquad (1.17)$$

where

$$R_n(r) = C_n\,J_n\,(\beta r) + D_n\,Y_n\,(\beta r) + E_n\,I_n\,(\beta r) + F_n\,K_n\,(\beta r) \qquad (1.18)$$

Here J_n and Y_n are the ordinary Bessel functions of the first and second kind, and I_n and K_n are the modified Bessel functions of the first and second kind.

To satisfy the clamped boundary conditions at the inner radius, the displacement and the slope of displacement must be zero. For the free boundary conditions at outer radius, the moment and shear force must be zero. The algebraic equations resulting from enforcing the four boundary conditions are given in Ref. [27] as

$$\begin{bmatrix} J_n(\beta a) & Y_n(\beta a) & I_n(\beta a) & K_n(\beta a) \\ (p_n J_n - J_{n+1})(\beta a) & (p_n Y_n - Y_{n+1})(\beta a) & (p_n I_n + I_{n+1})(\beta a) & (p_n K_n - K_{n+1})(\beta a) \\ \{(t_n - 1) J_n + s_n J_{n+1}\}(\beta b) & \{(t_n - 1) Y_n + s_n Y_{n+1}\}(\beta b) & \{(t_n + 1) I_n - s_n I_{n+1}\}(\beta b) & \{(t_n + 1) K_n + s_n K_{n+1}\}(\beta b) \\ \{p_n(t_n + 1) J_n - (np_n s_n + 1) J_{n+1}\}(\beta b) & \{p_n(t_n + 1) Y_n - (np_n s_n + 1) Y_{n+1}\}(\beta b) & \{p_n(t_n - 1) I_n - (np_n s_n - 1) I_{n+1}\}(\beta b) & \{p_n(t_n - 1) K_n - (np_n s_n - 1) K_{n+1}\}(\beta b) \end{bmatrix} \begin{Bmatrix} C_n \\ D_n \\ E_n \\ F_n \end{Bmatrix} = \begin{Bmatrix} 0 \\ 0 \\ 0 \\ 0 \end{Bmatrix}$$

where

$$p_n(\beta r) = n/\beta r$$

$$s_n(\beta r) = (1 - \nu)/\beta r$$

$$t_n(\beta r) = n(n-1)(1 - \nu)/(\beta r)^2$$

The values of β corresponding to the zero determinant of the matrix are sought for the nth nodal diameter mode and are denoted as β_n. The coefficients $\{C_n, D_n, E_n, F_n\}$ are obtained corresponding to β_n.

1.2.5 Dynamic Instability of Disc Brake Systems

One common direction in the study of brake squeal has been the numerical linear stability analysis predicting the instabilities of the system equilibrium. Many researchers believe that the onset of instability coincides with squealing. This view is adopted here in this study. The disc-pad brake system can be discretized by means of the assumed modes method or the finite element (FE) method. The canonical form of the equations governing the linear vibrations of the disc brake assembly are given in Ref. [2, 37, 29] as

$$\mathbf{M}\ddot{\mathbf{x}} + (\mathbf{G} + \mathbf{D})\dot{\mathbf{x}} + (\mathbf{K_s} + \mathbf{K_{ns}})\mathbf{x} = \mathbf{0} \qquad (1.19)$$

where **M, G** and **D** are the symmetric mass, skew-symmetric gyroscopic and symmetric viscous damping matrices, respectively. $\mathbf{K_s}$ and $\mathbf{K_{ns}}$ are the symmetric stiffness and non-symmetric frictional mode-coupling matrices, respectively, for the system.

$\mathbf{MK_s}$ systems will have transverse doublet modes which have an identical frequencies in the case of axisymmetric brake discs. These modes are stable in the absence of contact forces. However, as mentioned in section 1.2.3, introducing frictional forces in $\mathbf{K_{ns}}$, lead to mode-coupling type instability in the system in which frequency separation in doublet mode influences squeal propensity [2].

In the disc brake literature, $\mathbf{K_{ns}}$ has been constructed from two non-conservative friction loadings which are the frictional follower force [30] and the friction couple [32]. The conclusion was that frictional follower force in application to disc brake system has an insignificant influence on response stability. Kang *et al.* [27] found that the contact area (contact angle) strongly influences the flutter instability. The gyroscopic term $\mathbf{G\dot{x}}$ are typically ignored on the basis that brake squeal vibrations normally occur at low operational speeds. However, (Ouyang *et al.*, 2004) [32] and (Hochlenert *et al.*, 2007) [24] investigated the gyroscopic effects and their conclusion is that the rotation speed influences the destabilization of the disc brake system. Lastly, the $\mathbf{D\dot{x}}$ term is the effect of damping on the system. The damping types used in the previous disc brake models are the positive structural damping and the negative frictional damping. While it is clear that in $\mathbf{MDK_s}$ system, with $\mathbf{D} > 0$ and $\mathbf{K_s} > 0$, all the eigenvalues have a negative real part and the system is stable, this system becomes unstable when $\mathbf{G} \neq 0$ and more so for $\mathbf{K_{ns}} \neq 0$ [38]. Hochlenert *et al.* [24] showed that the system damping decreases at a rate of $1/\Omega$, where Ω is the rotation rate. The effect

of damping in circulatory systems was studied extensively in the work of (Hagedorn *et al.*, 2014) [38]. It turns out that the structure of the damping matrix is of utmost importance, and the common assumption, namely, representing the damping matrix as a linear combination of the mass and the stiffness matrices, may give completely misleading results for the problem of instability and the onset of self-excited vibrations. A comprehensive stability analysis of disc brake vibrations including gyroscopic, negative friction slope and mode-coupling mechanisms can be found in the work of (Kang *et al.*, 2009) [29]. It has also been observed that certain features, such as bolt assemblies or geometric imperfections, destroy the rotational symmetry of the disc, leading to frequency splitting [2]. Recent studies on asymmetric discs can be found in the work of (Wagner *et al.*, 2014) and (Kang, 2017) [39, 40].

1.2.6 Energy Dissipation

The purpose of the present section is to provide some perspective on the dissipation rates sustained in modern disc brake systems. Table 1.1 contains pertinent data for some representative production automobiles and the calculations are based on a constant deceleration [41, 42, 43, 2]. Nearly all of this mechanical dissipation takes the form of heat generation at the interface between the brake rotor and the pads. However, sounds of over 100 dB (as measured at a reasonable distance from the source) represent orders of magnitude less mechanical power. For example, a sound pressure level of 100 dB measured at a distance of 2 m from a source, has a sound power of approximately 0.25 W [2]. Thus, any mechanism, which transforms even a tiny fraction of the dissipated mechanical energy into sound pressure, represents a serious potential squeal problem.

Table 1.1: Dissipation rates in brakes for stops from 70 mph at impending brake lockup

Make & model	Average dissipation (kW)	Maximum dissipation (kW)
Ford Explorer	134.4	526.9
Porsche Boxster	139.6	434.9
Honda Civic LX	73.4	278.8

1.2.7 Methods to Eliminate Brake Squeal

The earliest discussion of methods to eliminate disc brake squeal can be found in the papers of Fosberry and Holubecki [44, 45]. They examined the effects of several design changes such as increasing the damping between the brake pad and backing plate and the backing plate and the brake piston, changing the caliper geometry and stiffness, modifying the backing plate. Their study about increasing viscous damping in the brake system was reflected in some commonly used treatments to suppress brake squeal in the automotive maintenance community. This includes the use of anti-squeal products between backing plates and calipers, application of a grease to the piston-backing plate contact area and the use of vibration shims which consist of constrained layer damping between backing pads and calipers [2]. Fieldhouse [46] presents an explanation for the effects of chamfering and/or slotting of the pads of friction material on squeal which is also a remedy used by automotive industry. His study center on the interplay between angular extent of contact between the pads and friction material and the modes of vibration of the stationary rotor. Another method includes sanding the

surfaces of brake rotor is still used in the automotive industry and was investigated by Rhee *et al.* [47]. They found that the roughness of the rotor is related to the friction film formation, but the precise correlation remains to be established.

Several novel methods for the suppression of brake squeal were discussed in the literature. These methods include the use of constrained layer damping [48], replacing piezoelectric transducer in contact with the backing plate of the inboard pad of friction material in a floating caliper disc brake [49], and reshaping the hat of the brake rotor to destroy the its symmetry [50].

1.2.8 Vibration Damping Using Shunted Piezoceramics

Piezoceramic elements have the unique ability to transfer mechanical energy into electrical energy and vice versa. By connecting suitable networks containing resistive and inductive elements to the electrodes of the piezoceramic element, an electromechanical vibration damper or vibration absorber can be created. These networks can be tuned to minimize the maximum amplitude of the frequency response function and thus resulting in broadband damping [51].

In the simplest and desired way, the impedance is built of passive electronic circuits, and no power supply is necessary. The electrical resonance must be tuned to one structural mode, which is the frequency of squealing in the context of disc brake squeal.

The performance of LR shunts are limited to a narrow frequency range around the resonance. Therefore, they are not suitable for systems with varying or multiple frequencies. Negative capacitance shunts have been discussed in (Behrens *et al.*, 2003) for a broadband control of structural vibrations [52]. A negative capacitance forms in

combination with passive LR shunts an *active-passive hybrid piezoelectric network* (APPN) [53, 54]. Previous works show that a negative capacitance in the electrical network has a similar effect like increasing the coupling coefficient of the piezoceramics. This results in a broader frequency range and a higher maximum energy dissipation.

1.2.9 Recent Developments in Brake Squeal Literature

In 2008, Kang *et al.* [27] studied the dynamic instability of a thin annular plate with friction interface using one-doublet mode model, two- degree-of-freedom discrete model, and a finite element model. They first modeled the frictional pads as stiffness elements and ignored their mass. The conclusion was that their model exhibits mode-coupling instability and that the contact span angle is an influential parameter in the instability of a brake disc. They then in 2009 modeled the pads as annular sector plates and found that pad natural frequencies are highly sensitive to the thickness variation which also means that any amount of wear difference between the two pads can be one of the factors contributing to squeal propensity [28]. In Ref. [33], (Kang, 2009) studied two types of instabilities of gyroscopic disc brake systems namely (i) mode-coupling type and (ii) negative slope type. He demonstrated the negative slope effect on generating squeal of in-plane torsion modes. The effect of contact area variation on squeal was also studied by (Kang, 2012) in Ref. [34]. The conclusion was that the contact span angle was again the influencing factor on squeal induced by the transverse doublet modes. Also for transverse doublet mode, the increase in the contact span angle produces certain periodic pattern in squeal propensity whereas it slightly decreases the squeal tendency of the in-plane dominant modes. The radial contact length was also an

important parameter in squeal occurrence. As it increased, in general, the squeal propensity was increased in both the transverse and in-plane modes. Investigation of in-plane modes and damping shims in disc brake squeal was studied by (Kang, 2012) in Ref. [35]. It was highlighted in the study that the damping shims cannot suppress the squeal propensity of the in-plane torsion dominant modes.

Although brake squeal is mostly known as a comfort problem, there are cases in which self-excited vibrations of the brake system not only cause an audible noise but also result in safety-relevant failures of the system. In particular, this can occur if lightweight design rims having very low damping are used (Hochlenert *et al.*, 2010) [55].

In Ref. [19, 20, 22, 23], (Hagedorn *et al.*, 2004-2006) proposed new technique to study and suppress brake squeal using active control via piezoceramic pads. As the piezoceramic elements can be used both as actuators as well as sensors, the smart pads were also useful in experimental investigations such as measuring transfer functions. The piezoceramic elements were placed between the pad's metallic back plate and the caliper as shown in Figure 1.11 and the smart pads performed very well under all conditions tested. However, according to Neubauer and Oleskiewicz [56], this method requires extensive sensing electronics and additional piezoceramics as sensors, complex amplifiers and power supply, which makes it expensive. Also, stability issues arise in the case that a sensor or actuator fails.

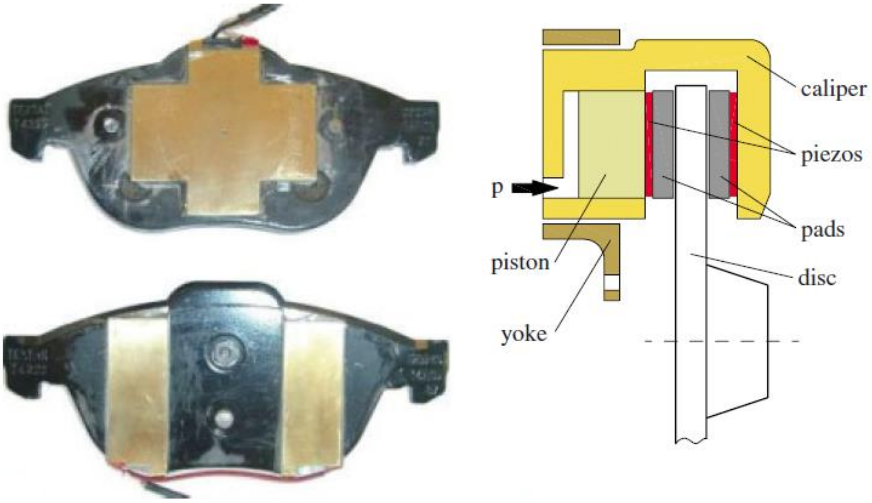

Figure 1.11: Smart pads designed by (Hagedorn *et al.*, 2004-2006)

Shunted piezoceramics have been proposed by (Neubauer and Oleskiewicz, 2008) in Ref. [57, 58] and proven to be an alternative to suppress brake squeal. The method involves the connection of an electrical impedance to a piezoceramic element. The electronic circuit was modeled as passive and semi-active circuit and the effect of negative capacitance was studied. Stability analysis provided the robustness of passive LR and semi-active LRC shunts for variations of the squealing frequency. It has been found that a negative capacitance shunt significantly increases the frequency range with a stabilized brake, which is necessary for a robust performance.

1.3 Scope of the Dissertation

In the last three decades, there has been a great deal of research done to model, predict, understand and eliminate brake squeal in disc brakes. During braking action, brakes produce irritant noise that causes customer dissatisfaction, energy dissipation, and in some cases safety-relevant failures of the brake system. Shunted piezoceramics have been used to suppress brake squeal and maximize energy dissipation associated with a single squealing frequency. The literature however lacks the study on harvesting the energy dissipated by brake squeal and the integration of shunted piezoceramic networks using finite element methods.

The aim of this dissertation is to develop the theory governing energy harvesting of brake squeal and to integrate the shunted piezoceramic networks with the vibrating disc brake system using finite element methods. This objective can be achieved by using passive or semi-active shunted piezoceramics with proper tuning of system parameters to maximize the power output. In the same time, this method will also increase the stability regions of the brake system with respect to squealing.

The dissertation is organized in five chapters. Chapter 1 briefly summarizes the literature review and introduces the concept of brake squeal and shunted piezoceramics. In Chapter 2, a finite element model of a brake disc with contact forces is developed and validated by considering two different simulations. Chapter 3 presents the theory of shunted piezoceramics attached to a brake system. In addition, the chapter provides numerical examples to emphasize the potential and merit of the proposed method in increasing the stability of the system. In Chapter 4, the predictions of the finite element modeling is validated against the performance of experimental prototype of both the

conventional and newly proposed disc brake systems. Chapter 5 summarizes the conclusions of the theoretical and experimental results. Furthermore, a brief summary of the future extension of this dissertation is outlined and the major contributions of this study are presented.

1.4 Summary

This chapter has presented the major components regarding disc brake squeal with a brief review of the literature underlying the physical phenomenon. The role of shunted piezoceramics in suppressing brake squeal has been briefly introduced. The significance, objectives and structure of the present work have also been discussed.

Chapter 2: Finite Element Modeling of Disc Brake Systems

2.1 Overview

This chapter presents the development of a finite element model of a brake disc. The *FEM* is based on *Kirchhoff plate theory* or simply the *classical plate theory* (CPT) which is an extension of the Euler-Bernoulli beam theory. The theory is based on *Kirchhoff hypotheses* which are discussed in details in this chapter.

Energy equations and the non-conservative work by the frictional pads are derived based on *Kirchhoff hypotheses* and discretized using the appropriate interpolating functions of an annular plate element. The equations of motion of the disc brake system are extracted by employing Lagrange dynamics approach. The resulting equations of motion are exercised to predict the brake disc modal parameters and stability of the system at different design parameters.

Computational algorithm is developed using commercial software package *MATLAB*® and validation of the performance of the developed *FEM* is achieved by performing two different numerical simulations. The chapter also includes the design of a laboratory scale brake disc system prototype that can resemble dynamic instabilities leading to brake squeal.

2.2 Disc Brake Model

Typical brake discs usually come in the form of a top-hat structure however, many researchers modeled the brake disc as an axisymmetric annular plate to simplify the complex geometry and gain more understanding on the squeal phenomenon.

These models differ in their configurations and their predictions of squeal. Therefore, in this chapter we consider the model developed by (Kang *et al.*, 2008) in Ref. [27] as shown in Figure 2.1.

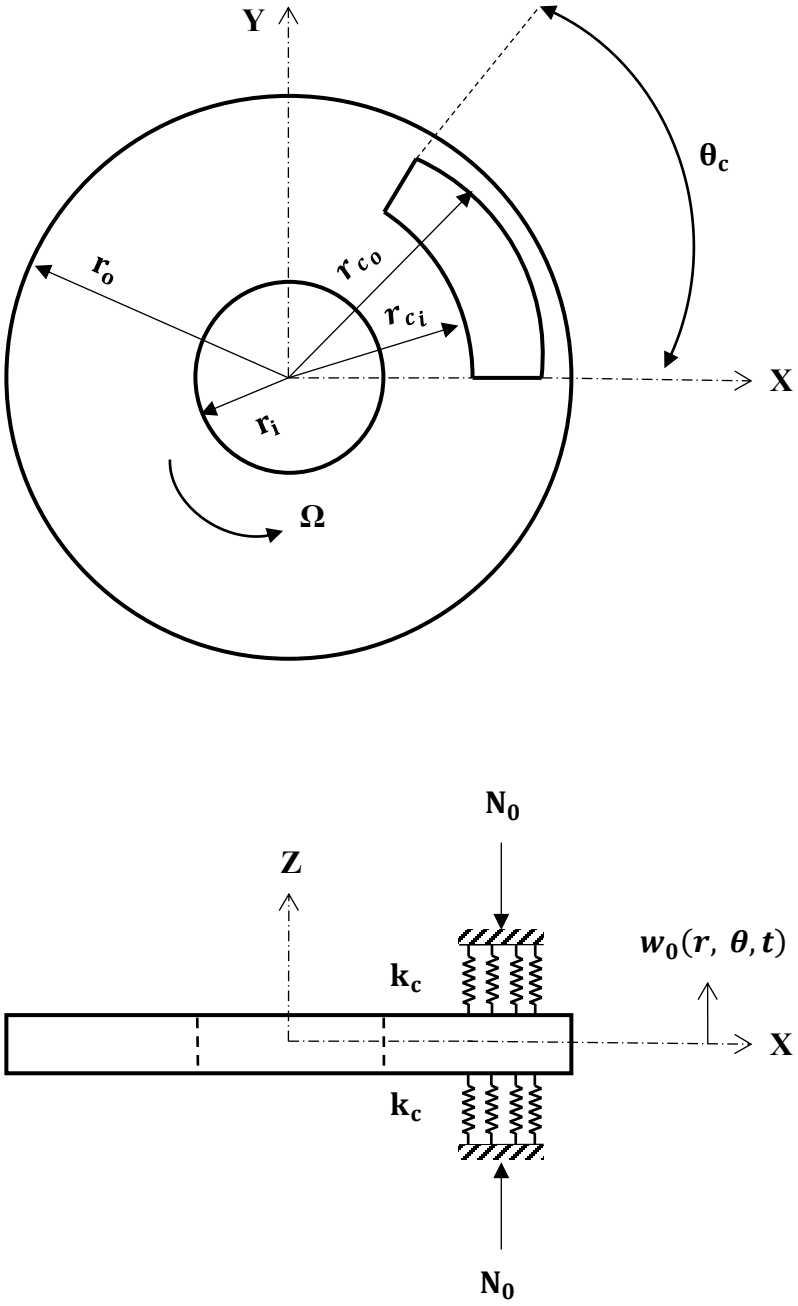

Figure 2.1: Rotating thin annular plate with annular sector friction interface

The brake disc system is modeled as an axisymmetric annular plate with two fixed annular sector contact interfaces. The model is assumed to be linear with homogenous and isotropic elastic material. Here, the preloads exerted on the back-plates of two pads by brake pressure are assumed to be identical under steady braking condition. The pre-stress is assumed to be uniformly distributed over the contact area such as $p_0 = N_0/A_C$ where N_0 is the preload and A_C is the contact area. Also, the coefficient of friction is assumed to be uniformly constant over the contact area of the disc.

2.2.1 Kirchhoff Plate Theory

The small deflection theory of thin plates, called *Kirchhoff theory,* is based on the following assumptions, known as the *Kirchhoff hypotheses* [59]:

1. The thickness of the plate (h_{pl}) is small compared to its lateral dimensions.
2. The middle plane of the plate does not undergo in-plane deformation. Thus, the midplane remains as the neutral plane after deformation or bending.
3. The displacement components of the midsurface of the plate are small compared to the thickness of the plate.
4. The influence of the transverse shear deformation is neglected. This implies that plane sections normal to the midsurface before deformation remain normal to the midsurface even after deformation or bending.
5. The transverse normals do not experience elongation (i.e., they are inextensible).

The fourth assumption implies that the transverse shear strains, ε_{xz} and ε_{yz}, are negligible, where *z* denotes the thickness direction. Also, the fifth assumption implies

that the transverse normal strain ε_{zz} under transverse loading can be neglected as well as the transverse normal stress σ_{zz} which is small compared to other stress components.

2.2.2 Displacements Field

The displacements field $(w_r\ , w_\theta\ , w_z)$ along the coordinates $(r, \theta,\ z)$ are [60]

$$\{w\} = \begin{Bmatrix} w_r(r,\theta,z,t) \\ w_\theta(r,\theta,z,t) \\ w_z(r,\theta,z,t) \end{Bmatrix} = \begin{Bmatrix} -z\left(\dfrac{\partial w_0}{\partial r}\right) \\ -z\left(\dfrac{1}{r}\dfrac{\partial w_0}{\partial \theta}\right) \\ w_0(r,\theta,t) \end{Bmatrix} \tag{2.1}$$

where $w_0(r,\theta,t)$ is the transverse displacement at point (x,y) in the annular plate which has an inner radius r_i and an outer radius r_o.

2.2.3 Stress-Strain Relations

The linear strain components referred to the cylindrical coordinate system are given as:

$$\varepsilon_{rr} = \frac{\partial w_r}{\partial r}$$

$$\varepsilon_{\theta\theta} = \frac{w_r}{r} + \frac{1}{r}\frac{\partial w_\theta}{\partial \theta}$$

$$\varepsilon_{zz} = \frac{\partial w_z}{\partial z} \tag{2.2}$$

$$\varepsilon_{r\theta} = \frac{1}{2}\left(\frac{1}{r}\frac{\partial w_r}{\partial \theta} + \frac{\partial w_\theta}{\partial r} - \frac{w_\theta}{r}\right)$$

$$\varepsilon_{z\theta} = \frac{1}{2}\left(\frac{\partial w_\theta}{\partial z} + \frac{1}{r}\frac{\partial w_z}{\partial \theta}\right)$$

$$\varepsilon_{rz} = \frac{1}{2}\left(\frac{\partial w_r}{\partial z} + \frac{\partial w_z}{\partial r}\right)$$

For the choice of the displacements field in equation (2.1), the only nonzero strains are

$$\{\varepsilon\} = \begin{Bmatrix} \varepsilon_{rr} \\ \varepsilon_{\theta\theta} \\ \varepsilon_{r\theta} \end{Bmatrix} = \begin{Bmatrix} \dfrac{\partial w_r}{\partial r} \\ \dfrac{\partial w_r}{r} + \dfrac{1}{r}\dfrac{\partial w_\theta}{\partial \theta} \\ \dfrac{1}{2}\left(\dfrac{1}{r}\dfrac{\partial w_r}{\partial \theta} + \dfrac{\partial w_\theta}{\partial r} - \dfrac{w_\theta}{r}\right) \end{Bmatrix} \tag{2.3}$$

The strain vector in equation (2.3) can also be expressed in terms of the transverse displacement $w_0(r, \theta, t)$ as

$$\{\varepsilon\} = \begin{Bmatrix} \varepsilon_{rr} \\ \varepsilon_{\theta\theta} \\ \gamma_{r\theta} \end{Bmatrix} = -z \begin{Bmatrix} \left(\dfrac{\partial^2 w_0}{\partial r^2}\right) \\ \dfrac{1}{r}\left(\dfrac{\partial w_0}{\partial r} + \dfrac{1}{r}\dfrac{\partial^2 w_0}{\partial \theta^2}\right) \\ \dfrac{2}{r}\left(\dfrac{\partial^2 w_0}{\partial r\, \partial \theta} - \dfrac{1}{r}\dfrac{\partial w_0}{\partial \theta}\right) \end{Bmatrix} \tag{2.4}$$

where $\gamma_{r\theta}$ is the engineering shear strain and is defined in terms of normal strain $\varepsilon_{r\theta}$ as $\gamma_{r\theta} = 2\varepsilon_{r\theta}$. Therefore, the nonzero stresses are

$$\{\sigma\} = \begin{Bmatrix} \sigma_{rr} \\ \sigma_{\theta\theta} \\ \tau_{r\theta} \end{Bmatrix} \tag{2.5}$$

Considering a plate made of an isotropic material where the material matrix $[C]$ is given as

$$[C] = \frac{E}{(1-\nu^2)}\begin{bmatrix} 1 & \nu & 0 \\ \nu & 1 & 0 \\ 0 & 0 & \dfrac{(1-\nu)}{2} \end{bmatrix} \tag{2.6}$$

where E is Young's modulus of elasticity and ν is the Poisson's ratio of the material. The stress-strain vectors are related by the material matrix and the relationship is expressed as

$$\{\sigma\} = [C]\{\varepsilon\} \tag{2.7}$$

which also permit stresses to be expressed in terms of the transverse displacement, $w_0(r, \theta, t)$ as:

$$\{\sigma\} = -z\,\frac{E}{(1-\nu^2)}[\bar{C}]\{\bar{\varepsilon}\} \tag{2.8}$$

where

$$[\bar{C}] = \begin{bmatrix} 1 & \nu & 0 \\ \nu & 1 & 0 \\ 0 & 0 & \dfrac{(1-\nu)}{2} \end{bmatrix} \tag{2.9}$$

and

$$\{\bar{\varepsilon}\} = \begin{Bmatrix} \left(\dfrac{\partial^2 w_0}{\partial r^2}\right) \\ \dfrac{1}{r}\left(\dfrac{\partial w_0}{\partial r} + \dfrac{1}{r}\dfrac{\partial^2 w_0}{\partial \theta^2}\right) \\ \dfrac{2}{r}\left(\dfrac{\partial^2 w_0}{\partial r\,\partial \theta} - \dfrac{1}{r}\dfrac{\partial w_0}{\partial \theta}\right) \end{Bmatrix} \tag{2.10}$$

2.2.4 Kinetic Energy

The total kinetic energy T of a rotating plate due to only transverse motion is given as:

$$T = \frac{1}{2}\int_m v^2\, dm \tag{2.11}$$

where v is the velocity of the transverse deflection from the midsurface and dm is the mass of an infinitesimal element of the plate. The following relations can also be used to expand the kinetic energy:

$$dm = \rho\, dV = \rho\, r\, dr\, d\theta\, dz \tag{2.12}$$

$$v = \left[\frac{\partial w_0(r,\theta,t)}{\partial t} + \Omega_z \frac{\partial w_0(r,\theta,t)}{\partial \theta}\right] \tag{2.13}$$

Substituting equations (2.12) and (2.13) in equation (2.11) yields

$$T = \frac{1}{2}\,\rho \iiint_V \left[\frac{\partial w_0(r,\theta,t)}{\partial t} + \Omega_z \frac{\partial w_0(r,\theta,t)}{\partial \theta}\right]^2 dV \tag{2.14}$$

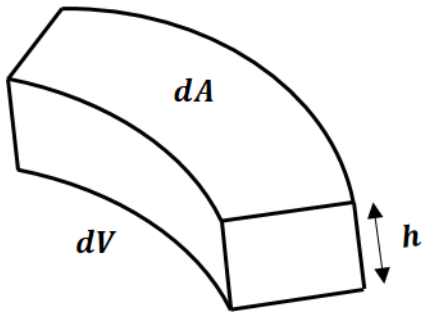

Figure 2.2: Infinitesimal volume element

The volume of an infinitesimal element shown in Figure 2.2 can be expressed as

$$dV = dA\, dz \tag{2.15}$$

Integrating the kinetic energy with respect to z yields

$$\int_{-\frac{h_{pl}}{2}}^{\frac{h_{pl}}{2}} dz = h_{pl} \tag{2.16}$$

For annular plates, the limits of the integral over area are given as:

$$\int_0^{2\pi} \int_{r_i}^{r_o} r\, dr\, d\theta \tag{2.17}$$

Expanding the kinetic energy of the plate yields three terms. The first term T_1 is due to traverse motion, the second term T_2 is linear in Ω_z, constant spin speed, which is linked with the Coriolis and gyroscopic effects, and a third term T_3 which is related to the centripetal acceleration.

$$T_1 = \frac{1}{2}\, \rho\, h_{pl} \int_0^{2\pi} \int_{r_i}^{r_o} \left[\frac{\partial w_0(r,\theta,t)}{\partial t}\right]^2 r\, dr\, d\theta \tag{2.18}$$

$$T_2 = \rho\, h_{pl}\, \Omega_z \int_0^{2\pi} \int_{r_i}^{r_o} \left[\frac{\partial w_0(r,\theta,t)}{\partial t} \cdot \frac{\partial w_0(r,\theta,t)}{\partial \theta}\right] r\, dr\, d\theta \tag{2.19}$$

$$T_3 = \frac{1}{2}\, \rho\, h_{pl}\, \Omega_z^2 \int_0^{2\pi} \int_{r_i}^{r_o} \left[\frac{\partial w_0(r,\theta,t)}{\partial \theta}\right]^2 r\, dr\, d\theta \tag{2.20}$$

2.2.5 Strain Energy

The strain energy U of an axisymmetric plate is given as

$$U = \frac{1}{2}\iiint_V \{\varepsilon\}^T\{\sigma\}\, dV \tag{2.21}$$

Equation (2.21) can be expressed in terms of the strain vector as

$$U = \frac{1}{2}\iiint_V \{\varepsilon\}^T[C]\{\varepsilon\}\, dV \tag{2.22}$$

The strain vector $\{\varepsilon\}$ given in equation (2.4) contains the variable z. Therefore, integrating the strain energy with respect to z yields

$$\int_z z^2\, dz = \int_{-\frac{h_{pl}}{2}}^{\frac{h_{pl}}{2}} z^2\, dz = \frac{h_{pl}^3}{12} \tag{2.23}$$

The final form of the strain energy is then given as

$$U = \frac{1}{2}\, D \int_0^{2\pi}\int_{r_i}^{r_o} \{\bar{\varepsilon}\}^T[\bar{C}]\{\bar{\varepsilon}\}\; r\, dr\, d\theta \tag{2.24}$$

where $[\bar{C}]$ and $\{\bar{\varepsilon}\}$ are given in equations (2.9) and (2.10), respectively. D is also given in equation (1.4) as $D = \frac{E\, h_{pl}^3}{12\,(1-\nu^2)}$.

2.2.6 Virtual Work

The virtual work due to force acting on the component is the scalar product of the force and virtual displacement

$$\delta W = \vec{F}.\delta\vec{r} \tag{2.25}$$

Here, we consider the work done by contact forces over the contact area. The virtual work can be decomposed as

$$\delta W = \delta W^{Top} + \delta W^{Bottom} \tag{2.26}$$

where δW^{Top} is the virtual work done by the top pad and δW^{Bottom} is the virtual work done by the bottom pad.

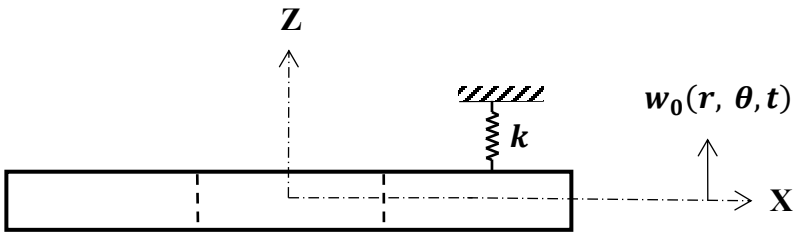

Figure 2.3: rotating plate in point contact with a spring

Figure 2.3 represents the top configuration of brake disc in point contact with the top pad where the force vector can be expressed as:

$$\begin{gathered}\vec{F} = F_N\,\hat{e}_z - F_f\,\hat{e}_\theta \\ \vec{F} = -k\,w_0(r,\theta,t)\,\hat{e}_z - \mu\,k\,w_0(r,\theta,t)\,\hat{e}_\theta\end{gathered} \tag{2.27}$$

The displacement vector $\vec{r}$ at any point on the structure is given by

$$\vec{r} = w_r(r,\theta,z\,,t)\;\hat{e}_r + w_\theta(r,\theta,z\,,t)\;\hat{e}_\theta + w_z(r,\theta,z\,,t)\;\hat{e}_z \tag{2.28}$$

which can also be expressed in terms of the transverse deflection $w_0(r,\theta,t)$

$$\vec{r} = -z\left(\frac{\partial w_0}{\partial r}\right)\hat{e}_r - z\left(\frac{1}{r}\frac{\partial w_0}{\partial \theta}\right)\hat{e}_\theta + w_0(r,\theta,t)\;\hat{e}_z \tag{2.29}$$

The virtual displacement is derived from the displacement vector as

$$\begin{aligned} \delta\vec{r} &= \delta w_r\,\hat{e}_r + \delta w_\theta\,\hat{e}_\theta + \delta w_z\,\hat{e}_z \\ \delta\vec{r} &= \left[-z\left(\frac{\partial}{\partial r}\right)\hat{e}_r - z\left(\frac{1}{r}\frac{\partial}{\partial \theta}\right)\hat{e}_\theta + \hat{e}_z\right]\delta w_0 \end{aligned} \tag{2.30}$$

From equations (2.25), (2.27) and (2.30), the virtual work due to forces from the top pad can be expressed as

$$\delta W^{Top} = -k\,w_0(r,\theta,t)\;\delta w_0 - \mu\,k\,w_0(r,\theta,t)\;\delta w_\theta \tag{2.31}$$

From equation (2.1)

$$w_\theta(r,\theta,z\,,t) = -z\left(\frac{1}{r}\frac{\partial w_0}{\partial \theta}\right)$$

and at the top surface of the annular plate

$$\begin{aligned} w_\theta(r,\theta,z^{Top},t) &= -\left(\frac{h_{pl}}{2}\right)\left(\frac{1}{r}\frac{\partial w_0}{\partial \theta}\right) \\ \delta w_\theta(r,\theta,z^{Top},t) &= -\left(\frac{h_{pl}}{2}\right)\left(\frac{1}{r}\frac{\partial}{\partial \theta}\right)\delta w_0 \end{aligned} \tag{2.32}$$

Therefore, the virtual work due to forces from the top pad is expressed in terms of the transverse deflection $w_0(r,\theta,t)$ as

$$\delta W^{Top} = \left\{-k\, w_0(r,\theta,t) + \mu\, k \left(\frac{h_{pl}}{2}\right) \left(\frac{1}{r}\frac{\partial w_0}{\partial \theta}\right)\right\} \delta w_0 \qquad (2.33)$$

Similarly, for the bottom pad of the same stiffness

$$W^{Bottom} = \left\{-k\, w_0(r,\theta,t) + \mu\, k \left(\frac{h_{pl}}{2}\right) \left(\frac{1}{r}\frac{\partial w_0}{\partial \theta}\right)\right\} \delta w_0 \qquad (2.34)$$

Considering the contact to be in area A_C rather than in a point as shown in Figure 2.4.

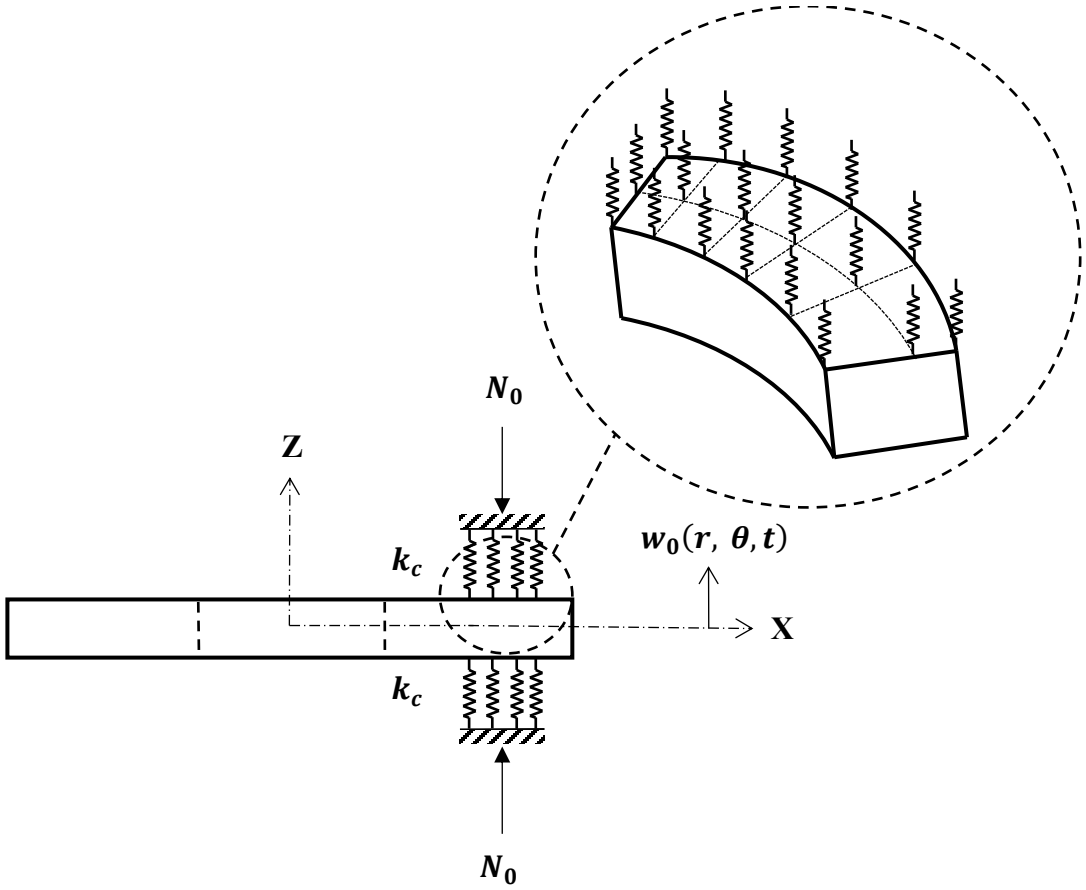

Figure 2.4: Area of contact (top configuration)

The total virtual work done by top and bottom pads is

$$\delta W = \int_0^{\theta_c} \int_{r_{c_i}}^{r_{c_o}} \Big[-2\, k_c\, w_0(r,\theta,t) + 2\, \mu\, k_c \left(\frac{h_{pl}}{2}\right)\left(\frac{1}{r}\frac{\partial w_0}{\partial \theta}\right)\Big]\, r\; dr\; d\theta \quad \delta w_0 \tag{2.35}$$

where k_c is the stiffness of a pad per unit volume. r_{c_i} and r_{c_o} refer to inner and outer radiuses of the contact surface whereas θ_c refers to the contact angle of the contact surface.

2.3 Finite Element Discretization

In this section, the dynamics of the brake disc modeled in section 2.2 are discretized using finite element methods. The discretization is guided by the work of Olson and Lindberg [61] and Kang *et al.* [27]. The brake disc is divided into N_{elm} number of elements with N_m nodal circles and N_n nodal diameters as shown in Figure 2.5. The contact interface in actual disc brake systems have the shape of the pad as in Figure 2.6. It is modeled as an annular plate sector and this sector is divided into N_c number of contact elements with N_{m_c} nodal circles and N_{n_c} nodal diameters as shown in Figure 2.7.

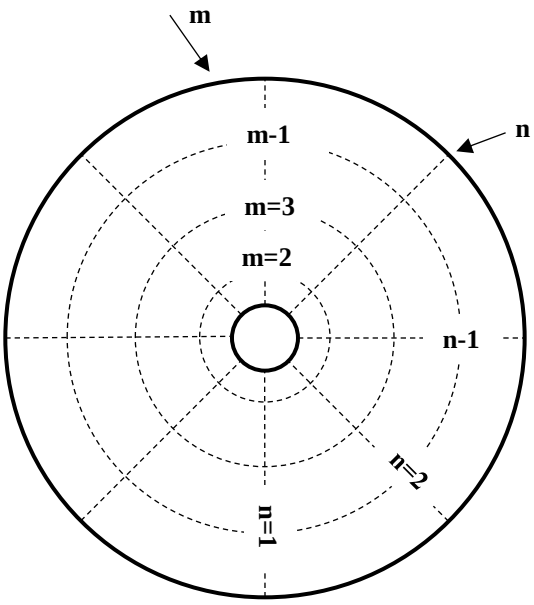

Figure 2.5: Finite element mesh of the brake disc

Figure 2.6: Actual pad in disc brake systems by BOSCH

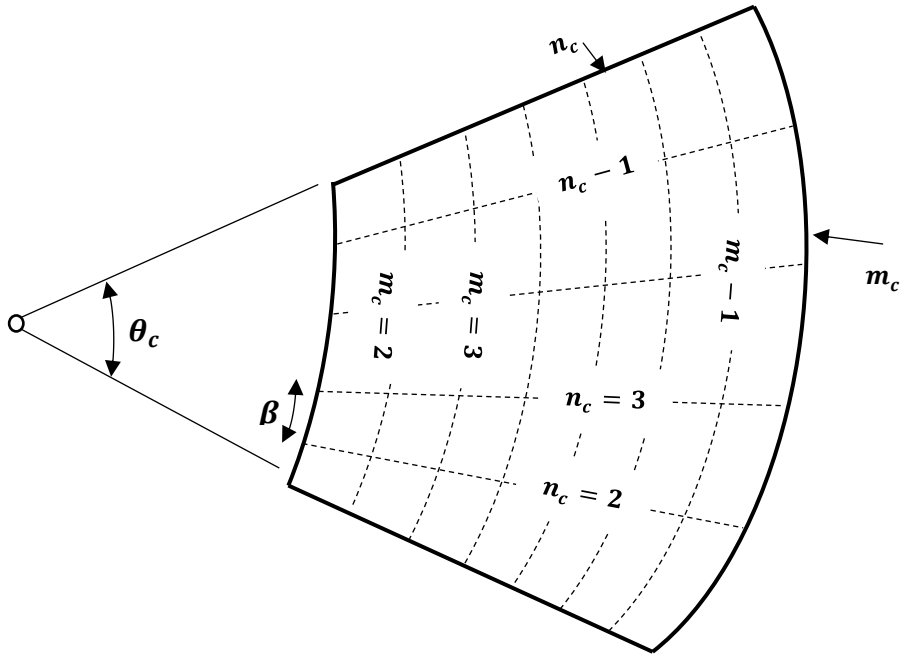

Figure 2.7: Finite element mesh of contact interface

2.3.1 Annular Plate Element

The finite element to be considered is shown in Figure 2.8. The element is a sector of an annular plate with inside radius r_1, outside radius r_2 and an angle β. The local nodes are numbered 1 to 4. Each node has three-degree-of-freedom defining its motions in polar coordinates. The translational DOF is denoted as w, the rotational DOF around r axis is denoted as $w_r = \frac{\partial w}{\partial r}$ and the rotational DOF around θ axis denoted as $w_\theta = \frac{\partial w}{\partial \theta}$.

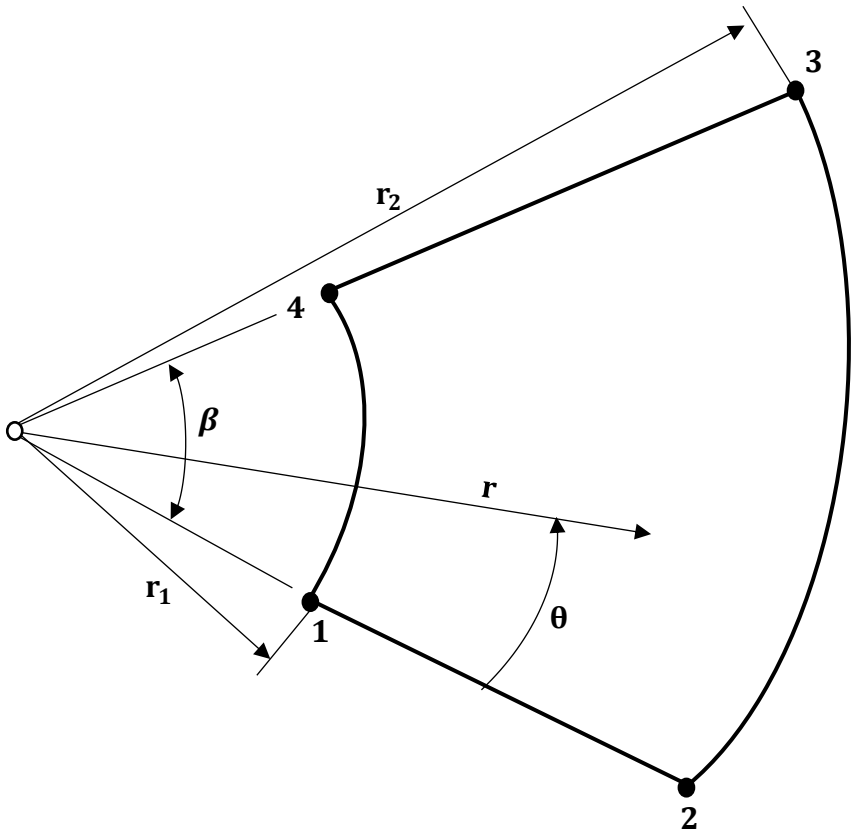

Figure 2.8: Annular sector finite element

The displacement vector of the annular sector finite element then becomes the twelve term column vector

$$\{\Delta^e\}^T = \left\{w_{r_1}, w_{\theta_1}, w_1, w_{r_2}, w_{\theta_2}, w_2, w_{r_3}, w_{\theta_3}, w_3, w_{r_4}, w_{\theta_4}, w_4\right\} \qquad (2.36)$$

2.3.2 Shape Functions

The displacement function of this element is assumed in the form

$$w(r,\theta) = a_1 + a_2\, r + a_3\, \theta + a_4\, r\, \theta + a_5\, r^2 + a_6\, \theta^2 + a_7\, r^2\, \theta + a_8\, r\, \theta^2 + a_9\, r^3 + a_{10}\, \theta^3 + a_{11}\, r^3\theta + a_{12}\, r\, \theta^3 \tag{2.37}$$

It can also be expressed as

$$w(r,\theta) = \{f_w\}\{A\} \tag{2.38}$$

where

$$\{f_w\} = \{1 \quad r \quad \theta \quad r\,\theta \quad r^2 \quad \theta^2 \quad r^2\,\theta \quad r\,\theta^2 \quad r^3 \quad \theta^3 \quad r^3\,\theta \quad r\,\theta^3\} \tag{2.39}$$

$$\{A\}^T = \{a_1 \quad a_2 \quad a_3 \quad a_4 \quad a_5 \quad a_6 \quad a_7 \quad a_8 \quad a_9 \quad a_{10} \quad a_{11} \quad a_{12}\} \tag{2.40}$$

The twelve corner displacements used in equation (2.36) may be evaluated from equation (2.37). Carrying this out leads to the matrix relation

$$\{\Delta^e\} = [T]\{A\} \tag{2.41}$$

where $[T]$ is the 12x12 transformation matrix. The unknown coefficients of $\{A\}$ are then obtained using

$$\{A\} = [T]^{-1}\{\Delta^e\} \tag{2.42}$$

Substituting equation (2.42) in equation (2.38) will lead to

$$w_0(r,\theta,t) = \{f_w\}[T]^{-1}\{\Delta^e\} \tag{2.43}$$

or

$$w_0(r,\theta,t) = \{N\}\{\Delta^e\} \tag{2.44}$$

where $\{N\}$ is the vector of shape functions

$$\{N\} = \{f_w\}[T]^{-1} \tag{2.45}$$

The final form of the vector of shape functions can be expressed as

$$\{N\} = \{N_1 \quad N_2 \quad N_3 \quad N_4 \quad N_5 \quad N_6 \quad N_7 \quad N_8 \quad N_9 \quad N_{10} \quad N_{11} \quad N_{12}\} \tag{2.46}$$

where

$$N_1 = \frac{\Delta_{r_1}\Delta_{r_2}^2\Delta_{\beta\theta}}{\Delta_{r_{12}}^2\,\beta} \qquad N_2 = \frac{\Delta_{r_2}\Delta_{\beta\theta}^2\,\theta}{\Delta_{r_{12}}\,\beta^2}$$

$$N_3 = \frac{\Delta_{r_2}\left\{-\Delta_{r_2}\Delta_1\beta^3 + \Delta_{r_1}\Delta_2\theta\beta^2 - 3\Delta_{r_{12}}^2\,\theta^2\beta + 2\Delta_{r_{12}}^2\theta^3\right\}}{\Delta_{r_{12}}^3\beta^3}$$

$$N_4 = \frac{\Delta_{r_1}^2\Delta_{r_2}\Delta_{\beta\theta}}{\Delta_{r_{12}}^2\,\beta} \qquad N_5 = -\frac{\Delta_{r_1}\Delta_{\beta\theta}^2\,\theta}{\Delta_{r_{12}}\,\beta^2}$$

$$N_6 = \frac{\Delta_{r_1}\left\{\Delta_{r_1}\Delta_1\beta^3 - \Delta_{r_2}\Delta_2\theta\beta^2 - 3\Delta_{r_{12}}^2\theta^2\beta - 2\Delta_{r_{12}}^2\theta^3\right\}}{\Delta_{r_{12}}^3\beta^3}$$

$$N_7 = \frac{\Delta_{r_1}^2\Delta_{r_2}\,\theta}{\Delta_{r_{12}}^2\,\beta} \qquad N_8 = \frac{\Delta_{r_1}\Delta_{\beta\theta}\,\theta^2}{\Delta_{r_{12}}\,\beta^2}$$

$$N_9 = \frac{\Delta_{r_1}\theta\left\{\Delta_{r_2}\Delta_2\beta^2 - 3\Delta_{r_{12}}^2\theta\beta + 2\Delta_{r_{12}}^2\theta^2\right\}}{\Delta_{r_{12}}^3\beta^3}$$

$$N_{10} = \frac{\Delta_{r_1}\Delta_{r_2}^2\,\theta}{\Delta_{r_{12}}^2\,\beta} \qquad N_{11} = \frac{\Delta_{r_2}\Delta_{\beta\theta}\,\theta^2}{\Delta_{r_{12}}\,\beta^2}$$

$$N_{12} = \frac{\Delta_{r_2}\theta\left\{-\Delta_{r_1}\Delta_2\beta^2 + 3\Delta_{r_{12}}^2\theta\beta - 2\Delta_{r_{12}}^2\theta^2\right\}}{\Delta_{r_{12}}^3\beta^3}$$

where

$$\Delta_{r_1} = (r - r_1)\ ,\ \Delta_{r_2} = (r - r_2)\ ,\ \Delta_{r_{12}} = (r_1 - r_2)\ ,\ \Delta_{\beta\theta} = (\beta - \theta)$$

$$\Delta_1 = (2\,r - 3\,r_1 + r_2)\ , \qquad \Delta_2 = (2\,r - r_1 - r_2)$$

2.3.3 Element Kinetic Energy

The kinetic energy of the annular plate yields three terms as discussed in section 2.2.4. The three terms can be discretized using equation (2.44) as

$$T_1 = \frac{1}{2}\left\{\dot{\Delta}^e\right\}^T\left(\rho h_{pl}\int_0^{\beta}\int_{r_1}^{r_2}\{N\}^T\{N\}\ \ r\,dr\,d\theta\right)\left\{\dot{\Delta}^e\right\} \tag{2.47}$$

$$T_2 = \frac{1}{2}\left\{\dot{\Delta}^e\right\}^T\left(2\rho h_{pl}\Omega_z\int_0^{\beta}\int_{r_1}^{r_2}\{N\}^T\frac{\partial\{N\}}{\partial\theta}\ \ r\,dr\,d\theta\right)\left\{\dot{\Delta}^e\right\} \tag{2.48}$$

$$T_3 = \frac{1}{2}\left\{\dot{\Delta}^e\right\}^T\left(\rho h_{pl}\Omega_z^2\int_0^{\beta}\int_{r_1}^{r_2}\frac{\partial\{N\}^T}{\partial\theta}\frac{\partial\{N\}}{\partial\theta}\ \ r\,dr\,d\theta\right)\left\{\dot{\Delta}^e\right\} \tag{2.49}$$

Note that the limits of integration have been changed to describe a single element instead of the whole plate and the area of a finite element is shown in Figure 2.9.

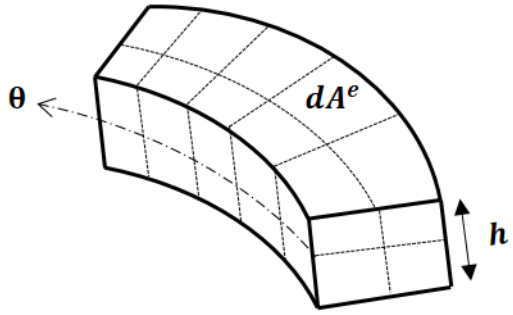

Figure 2.9 : Area of finite element

2.3.4 Element Strain Energy

The strain energy of the annular plate was derived in section 2.2.5 and the final form was given in equation (2.24). For a single annular finite element the strain energy is

$$U = \frac{1}{2}\{\Delta^e\}^T \left(D \int_0^{\beta} \int_{r_1}^{r_2} [\bar{\varepsilon}^e]^T [\bar{C}][\bar{\varepsilon}^e] \; r \, dr \, d\theta \right) \{\Delta^e\} \tag{2.50}$$

where

$$[\bar{\varepsilon}^e] = [\bar{\varepsilon}]_{3x12} = \begin{bmatrix} \left(\dfrac{\partial^2\{N\}}{\partial r^2}\right) \\ \dfrac{1}{r}\left(\dfrac{\partial\{N\}}{\partial r} + \dfrac{1}{r}\dfrac{\partial^2\{N\}}{\partial\theta^2}\right) \\ \dfrac{2}{r}\left(\dfrac{\partial^2\{N\}}{\partial r\,\partial\theta} - \dfrac{1}{r}\dfrac{\partial\{N\}}{\partial\theta}\right) \end{bmatrix} \tag{2.51}$$

2.3.5 Element Generalized Forces

The total virtual work done by top and bottom pads was derived in section 2.2.6 and was expressed in equation (2.35). The displacement function obtained by finite element methods was also given in equation (2.44) as

$$w_0(r,\theta,t) = \{N\}\{\Delta^e\} = \{\Delta^e\}^T\{N\}^T$$

and the discretized virtual displacement can be expressed as

$$\delta w_0 = \delta(\{N\}\{\Delta^e\}) = \{N\}\,\delta(\{\Delta^e\}) = \delta(\{\Delta^e\})\,\{N\}^T \tag{2.52}$$

Therefore, the generalized forces acting on a single element in the contact interface can be expressed using equations (2.35), (2.44) and (2.52) as

$$\begin{gathered}\{Q^e\} = -(k_c\,[\bar{A}^e] + \mu k_c\,[\bar{B}^e])\,\{\Delta^e\} \\ \{Q^e\} = -([A^e] + [B^e])\,\{\Delta^e\}\end{gathered} \tag{2.53}$$

where

$$[\bar{A}^e] = 2\int_0^{\beta}\int_{r_1}^{r_2}\{N\}^T\,\{N\}\,r\;dr\;d\theta \tag{2.54}$$

$$[\bar{B}^e] = -2\left(\frac{h_{pl}}{2}\right)\int_0^{\beta}\int_{r_1}^{r_2}\{N\}^T\left(\frac{1}{r}\frac{\partial\{N\}}{\partial\theta}\right)\,r\;dr\;d\theta \tag{2.55}$$

2.3.6 Element Equations of Motion

The equations of motion of an annular element in the contact interface can be derived using Lagrange's energy method as

$$\frac{d}{dt}\left[\frac{\partial \mathcal{L}}{\partial\{\dot{\Delta}^e\}}\right] - \left[\frac{\partial \mathcal{L}}{\partial\{\Delta^e\}}\right] = \{Q^e\} \tag{2.56}$$

where $\mathcal{L} = T - U$ denotes the Lagrangian.

Following the differentiation steps and utilizing Equations (2.47), (2.48), (2.49) and (2.53) into equation (2.56) results in the element matrices. The first kinetic energy term results in element mass matrix $[M^e]$ whereas the second term results in the element gyroscopic matrix $[G^e]$. The third kinetic energy term produces the element centrifugal matrix $[R^e]$ and the potential energy U results in the element stiffness matrix $[K^e]$. The element contact stiffness matrix $[A^e]$ and the non-conservative work matrix produced by friction couple $[B^e]$ are a result of the generalized force vector $\{Q^e\}$. The element equations of motion with element matrices of the size 12x12 becomes

$$[M^e]\{\ddot{\Delta}^e\} + [G^e]\{\dot{\Delta}^e\} + ([K^e] + [A^e] + [B^e] - [R^e])\{\Delta^e\} = \{0\} \tag{2.57}$$

where $[M^e]$, $[K^e]$, $[A^e]$ and $[R^e]$ are symmetric matrices, $[G^e]$ is a skew symmetric matrix and $[B^e]$ is a non-symmetric matrix.

2.3.7 Element Matrices Assembly

The assembly of the element matrices of the individual plate elements in contact with two stationary pads aims at forming the global matrices of the entire disc brake system. During such a process, the compatibility of the deflections of the neighboring

elements at the common nodes connecting them must be ensured. Also, the equilibrium conditions of the forces and moments acting at the nodes must be guaranteed.

The full system equations of motion is given as

$$[M]\{\ddot{\Delta}\} + [G]\{\dot{\Delta}\} + ([K] + [A] + [B] - [R])\{\Delta\} = \{0\} \quad (2.58)$$

The size of the global matrices $[M]$, $[G]$, $[K]$, $[A]$, $[B]$ and $[R]$ is calculated based on the following formula

$$size = 2(N_n\, N_m)(ndof)\; X\; 2(N_n\, N_m)(ndof) \quad (2.59)$$

where

N_n is number of nodal diameters of the mesh

N_m is number of nodal circles of the mesh

$ndof$ is number of degree-of-freedom per node

2.3.8 Boundary Conditions

The full disc brake system equations of motion obtained in section 2.3.7 are subjected to boundary conditions. In this study, the disc brake system is subjected to clamped boundary conditions at the inner radius and free boundary conditions at outer radius. In this case, the process is achieved by restraining all degree-of-freedom corresponding to the nodes at the inner radius. The resulting overall system equations of motion are

$$[M_o]\{\ddot{\Delta}_o\} + [G_o]\{\dot{\Delta}_o\} + ([K_o] + [A_o] + [B_o] - [R_o])\{\Delta_o\} = \{0\} \quad (2.60)$$

The length of the square overall matrices $[M_o]$, $[G_o]$, $[K_o]$, $[A_o]$, $[B_o]$ and $[R_o]$ is

$$length = 2(N_n\, N_m)(ndof) - 2(N_n)(ndof) \tag{2.61}$$

2.4 Modal and System Stability Analysis

This section discusses the modal analysis and disc brake system stability. The vibration characteristics of the system, namely, the natural frequencies and mode shapes are discussed and three cases are covered which are: (i) the vibration of a stationary brake disc (annular plate), (ii) the vibration of a stationary brake disc in contact with two stationary pads and (iii) the vibration of a rotating brake disc in contact with two stationary pads.

2.4.1 Free Vibration of Stationary Brake Disc

In this case, the overall system equations of motion expressed in equation (2.60) are reduced to

$$[M_o]\{\ddot{\Delta}_o\} + [K_o]\{\Delta_o\} = \{0\} \tag{2.62}$$

Assuming a solution of the form

$$\Delta_o(t) = \{V\}\, e^{\lambda t} \tag{2.63}$$

The characteristic equation for the system becomes

$$\det([K_o] + \lambda^2\, [M_o]) = 0 \tag{2.64}$$

where λ represents the poles of the system. The appearance of positive real parts of λ indicates an unstable mode which results in an unstable system. It is well known that for symmetric $[M_o]$ and $[K_o]$, the system is always stable.

2.4.2 Free Vibration of Stationary Disc Brake System

This case represents the full assembly of the stationary brake disc in contact with two fixed pads. The linear system equations obtained in (2.60) are reduced to

$$[M_o]\{\ddot{\Delta}_o\} + ([K_o] + [A_o] + [B_o])\{\Delta_o\} = \{0\} \tag{2.65}$$

Substituting equation (2.63) in equation (2.65) yields the system characteristic equation

$$\det([H_o] + \lambda^2\,[M_o]) = 0 \tag{2.66}$$

where $[H_o] = [K_o] + [A_o] + [B_o]$ and the appearance of positive real λ indicates an unstable mode due to friction couple which is also known as the onset of squeal or mode-coupling instability.

2.4.3 Free Vibration of Rotating Disc Brake System

In this case, the full assembly consisting of a rotating disc in contact with two stationary pads is considered. The full system equations are given in equation (2.60) and is expressed here in a simplified notation as

$$[M_o]\{\ddot{\Delta}_o\} + [G_o]\{\dot{\Delta}_o\} + [H_o]\{\Delta_o\} = \{0\} \tag{2.67}$$

here $[H_o] = ([K_o] + [A_o] + [B_o] - [R_o])$ is the augmented overall stiffness matrix which takes into account the brake disc stiffness matrix, the normal contact force matrix, the friction couple matrix and the centrifugal effects of the annular plate.

In order to study the system stability, the equations of motion expressed in equation (2.67) are casted in state space form as

$$\{\dot{x}\} = [\mathbf{A}]\{x\} \tag{2.68}$$

where $\{x\}$ is the state space vector and is represented in terms of the physical DOF as

$$\{x\} = \begin{Bmatrix} \{x_1\} \\ \{x_2\} \end{Bmatrix} = \begin{Bmatrix} \{\Delta_o\} \\ \{\Delta_o\} \end{Bmatrix} \tag{2.69}$$

and

$$[\mathbf{A}] = \begin{bmatrix} [0] & [I] \\ -[M_o]^{-1}\,[H_o] & -[M_o]^{-1}\,[G_o] \end{bmatrix} \tag{2.70}$$

The characteristic equation of such system is given as

$$\det(\lambda\,[I] - [\mathbf{A}]) = 0 \tag{2.71}$$

For a linear time-invariant system, the system is stable in the sense of Lyapunov if

$$Re\{\lambda([\mathbf{A}])\} < 0 \tag{2.72}$$

2.5 Model Verification

In this section, the obtained *FEM* formulation of the system assembly and the computational algorithm developed using software package *MATLAB*® are validated against some published work in the literature. Modal and system stability analyses are also studied to predict the onset of squealing.

2.5.1 Numerical Simulations

In order to examine the capabilities of the developed computational algorithm on performing modal and stability analyses, two different numerical simulations are considered.

2.5.1.1 Simulation I

This simulation aims to test the accuracy of the finite element model developed in this chapter. The obtained non-dimensional frequencies of the stationary disc are compared with exact solutions in Ref. [62, 63] and numerical solution of software package *ANSYS*® for radius ratio 0.3 as most commercial brake discs have inner to outer radius ratios of 0.2 to 0.3. The frequency constants, λ_{nm}^2, are independent of the disc dimensions and the disc material except for a modest dependence on Poisson's ratio. The actual frequencies can be found from the frequency constants as follows

$$f_{nm} = \frac{\lambda_{nm}^2}{2\,\pi\,r_o^2}\sqrt{\frac{\rho\,h}{D}} \tag{2.73}$$

FE mesh specifications used in this section are given in Table 2.1 and the frequency constants of the transverse doublet modes of the disc with Poisson's ratio 0.3 are summarized in Table 2.2

Table 2.1: Finite element mesh specifications used in simulation I

FE mesh specification	Symbol	Value
Disc nodal circles	N_m	80
Disc nodal diameters	N_n	30
Element angle	β	6^o
Disc elements	N_{elm}	4740

Table 2.2: Frequency constants of transverse doublet modes for stationary annular disc with radius ratio 0.3 and Poisson's ratio 0.3 subject to clamped-free boundary conditions

	Radius Ratio 0.3 λ_{nm}^2				
n	Exact [62, 63]	*ANSYS*®	Error %	*FEM*	Error %
0	6.6604	6.675	0.21%	6.658	0.03%
1	6.552	6.568	0.24%	6.546	0.09%
2	7.957	7.970	0.17%	7.942	0.18%
3	13.276	13.281	0.04%	13.261	0.11%
4	22.074	22.071	0.01%	22.064	0.04%
5	33.557	33.548	0.03%	33.556	0.00%

The maximum error of the developed finite element model obtained from Table 2.2 is 0.18%. Therefore, the FE model can be considered of a high accuracy and can be used in analyzing the system stability.

2.5.1.2 Simulation II

In this simulation, the results obtained by (Kang *et al.*, 2008) [27] based on the assumed modes method will be compared to the developed *FEM* of this work. System parameters are summarized in Table 2.3 and FE mesh specifications used in this section are given in Table 2.4. FE mesh of disc and contact area are also shown in Figure 2.10.

Table 2.3: Nominal values of system parameters

Parameter	Symbol	Value
Outer radius of the disc	r_o	150 mm
Inner radius of the disc	r_i	40 mm
Outer radius of contact area	r_{c_o}	142 mm
Inner radius of contact area	r_{c_i}	100 mm
Thickness of the disc	h	26 mm
Contact angle	θ_c	60^o
Young's modulus	E	88.9 GPa
Density	ρ	7150 kg/m^3
Poisson's ratio	ν	0.285
Nominal contact stiffness	k_{nom}	0.35 x 10^{11} N/m^3

Table 2.4: Finite element mesh specifications used in simulation II

FE mesh specification	Symbol	Value
Disc nodal circles	N_m	56
Disc nodal diameters	N_n	36
Element angle	β	5^o
Disc elements	N_{elm}	3960
Contact area nodal circles	N_{m_c}	22
Contact area nodal diameters	N_{n_c}	13
Contact area elements	N_c	252

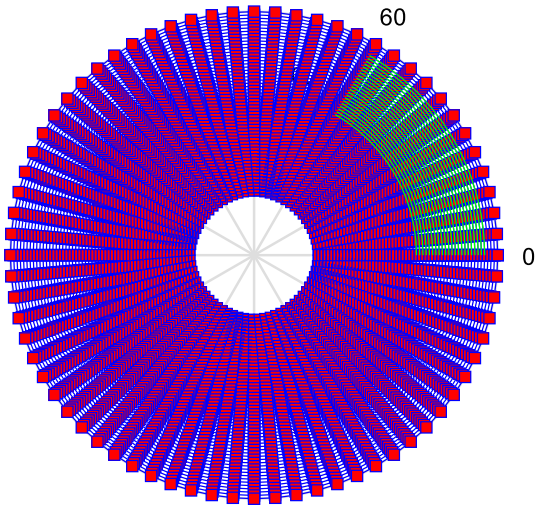

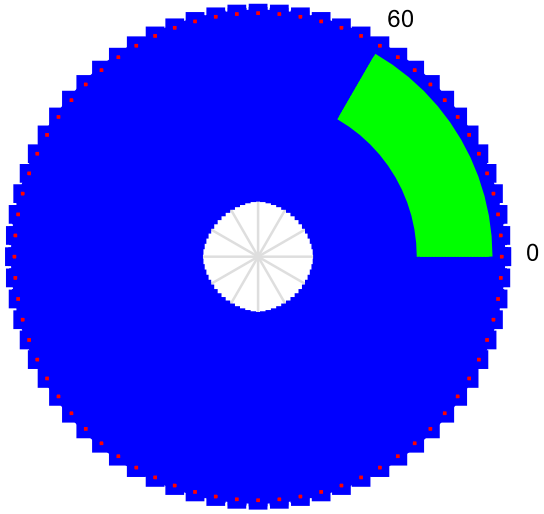

Figure 2.10: Finite element mesh of disc and contact area

The corresponding modal frequencies for the free vibration case of the brake disc (without contact) are obtained by solving the boundary value problem as detailed in section 1.2.4 (exact solution) and are given by (Kang *et al.*, 2008) in Ref. [27]. The exact frequencies are compared to frequencies obtained using the *FEM* and the results are summarized in Table 2.5.

Table 2.5: Natural frequencies of the transverse doublet modes of annular plate subject to clamped-free boundary conditions

Doublet Modes $\boldsymbol{n}$	Exact $\boldsymbol{f_n\ (Hz)}$ [27]	*FEM* $\boldsymbol{f_n\ (Hz)}$	Error %
1	1153	1152	0.06%
2	1447	1445	0.12%
3	2553	2551	0.08%
4	4318	4317	0.03%
5	6589	6587	0.02%
6	9308	9309	0.01%
7	12 461	12 465	0.03%
8	16 040	16 049	0.05%

The transverse doublet modes 4 and 5 are shown in Figures 2.11 and 2.12, respectively. Software package *ANSYS*® was used in this simulation only to generate the mode shapes figures.

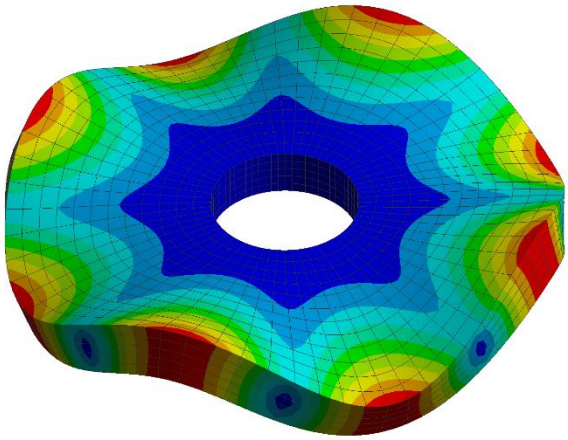

Figure 2.11: Disc transverse doublet mode n = 4 with corresponding f_4 = 4318 Hz

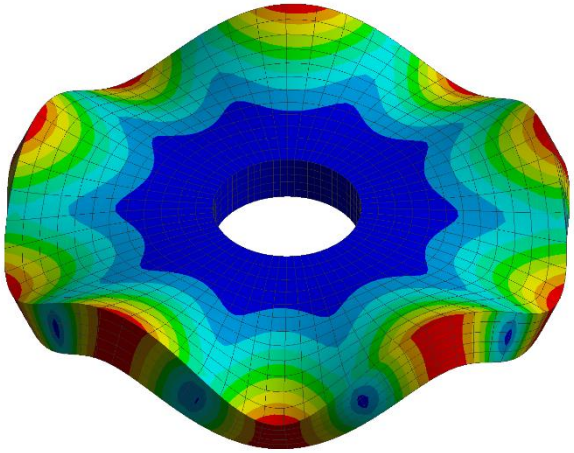

Figure 2.12: Disc transverse doublet mode n = 5 with corresponding f_5 = 6589 Hz

Figures 2.13-2.16, illustrate the stability of the transverse doublet modes 4 and 5 and their corresponding mode-coupling frequency behavior. The critical values of the coefficient of friction μ_{cr} can be extracted from the figures to be 0.33 and 0.36 for modes 4 and 5, respectively. Squealing occurs at typical values of $\mu_{cr} = 0.2 - 0.6$ as

discussed in section 1.2.2. Therefore, Modes 1, 2, 3, 6, 7 and 8 do not experience flutter instability in the range of typical values of μ_{cr}.

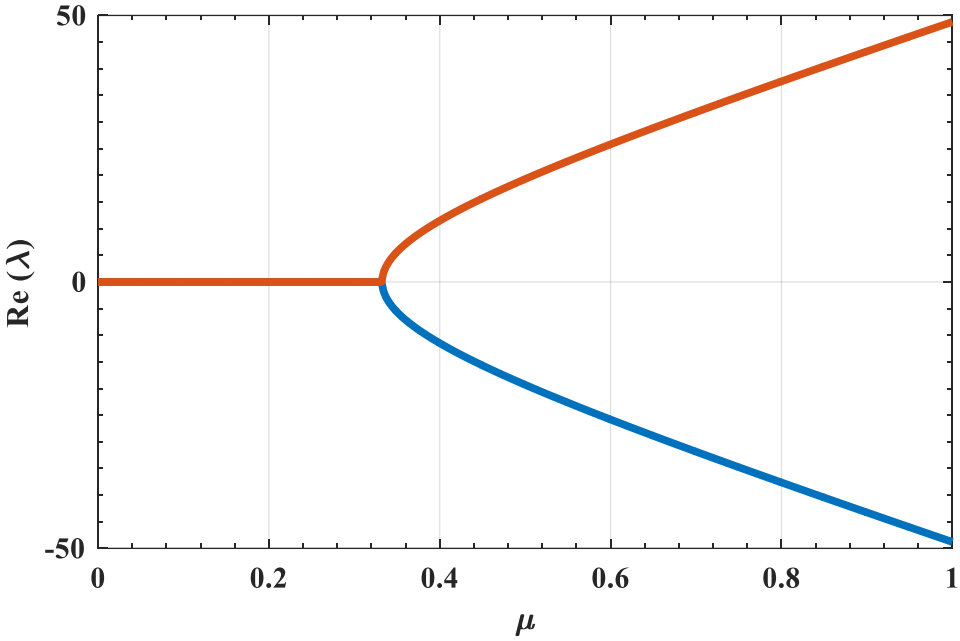

Figure 2.13: Stability of transverse doublet mode 4

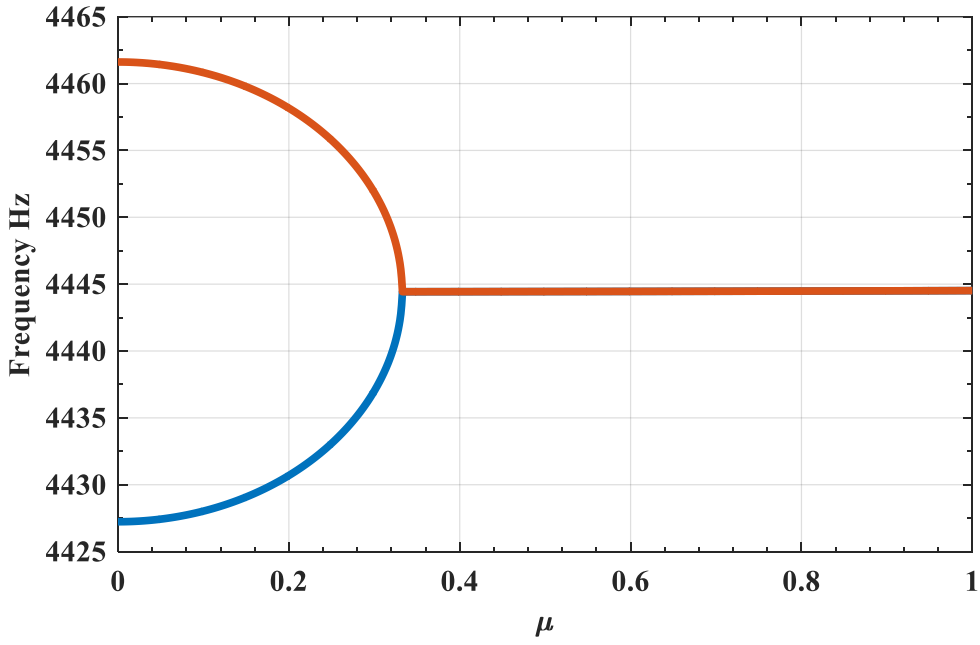

Figure 2.14: Mode-coupling behavior of transverse doublet mode 4

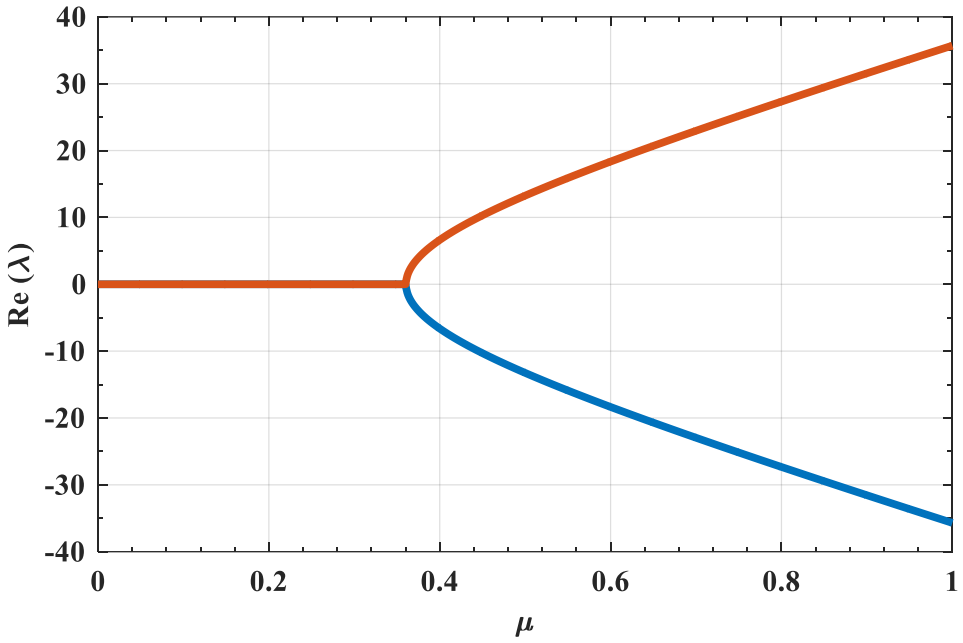

Figure 2.15: Stability of transverse doublet mode 5

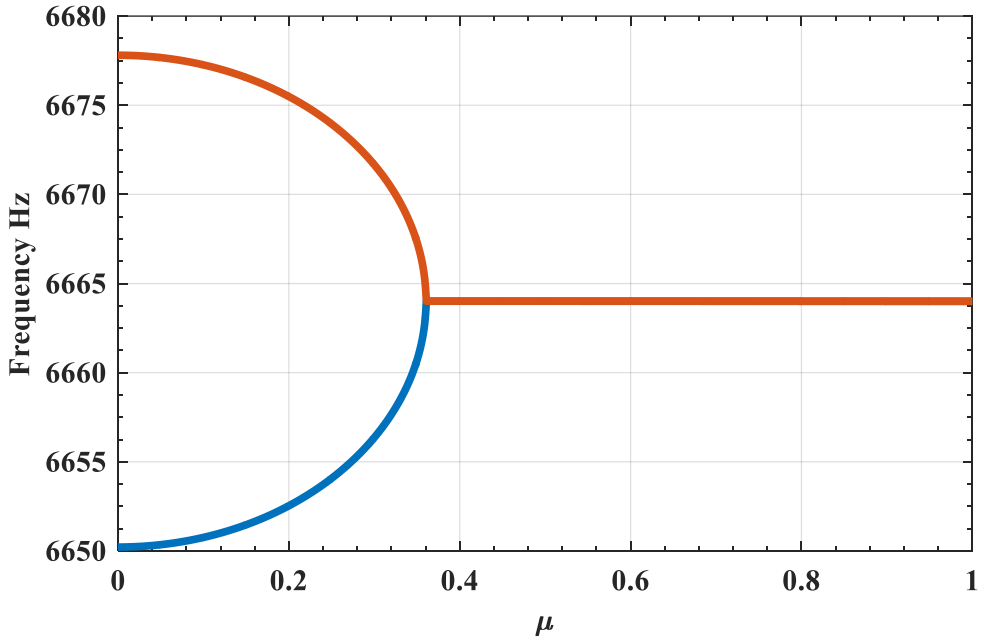

Figure 2.16: Mode-coupling behavior of transverse doublet mode 5

2.6 Design of Disc Brake System Prototype

This section aims at designing a new disc brake system prototype that can produce important brake squeal features. The design can be used in laboratories and is compared later in Chapter 4 against the experimental results. The process of developing such a design can be performed using *FEM* formulation that has been developed and verified in this chapter. The section includes modal and stability analyses and will be broken down into three sections which are design of stationary brake disc, design of stationary disc brake system, and Coriolis effects on brake discs.

2.6.1 Design of Stationary Brake Disc

The new brake disc is assumed to be made out of aluminum and will have the same radius ratio of 0.3 as most commercial brake discs have. System parameters and FE mesh specifications are summarized in Tables 2.6 and 2.7, respectively.

Table 2.6: System parameters of new brake disc prototype

Parameter	Symbol	Value
Outer radius of the disc	r_o	120 mm
Inner radius of the disc	r_i	36 mm
Thickness of the disc	h	0.88 mm
Young's modulus	E	71 GPa
Density	ρ	2770 kg/m^3
Poisson's ratio	ν	0.33

Table 2.7: Finite element mesh specifications of new brake disc prototype

FE mesh specification	Symbol	Value
Disc nodal circles	N_m	43
Disc nodal diameters	N_n	36
Element angle	β	5^o
Disc elements	N_{elm}	3024

The boundary conditions of the brake disc are assumed to be clamped at the inner edge and free at the outer edge. The system equations are solved and the natural frequencies of the transverse doublet modes of the disc are presented in Table 2.8 using the developed *FEM* and were compared against numerical solution of *ANSYS*® Workbench and exact solution in Ref. [62, 63]. Figure 2.17 shows the frequency response of the brake disc subjected to a harmonic unit force at the outer edge.

Table 2.8: Natural Frequencies of transverse doublet modes of new brake disc prototype subject to clamped-free boundary conditions

	Natural Frequency $f\ (Hz)$				
n	Exact [62, 63]	*ANSYS*®	Error %	*FEM*	Error %
1	98.67	100.12	1.47	98.73	0.06
2	119.81	119.62	0.16	118.31	1.25
3	199.91	197.34	1.29	196.73	1.59
4	322.40	327.58	1.61	327.64	1.63
5	505.31	498.19	1.41	498.87	1.27

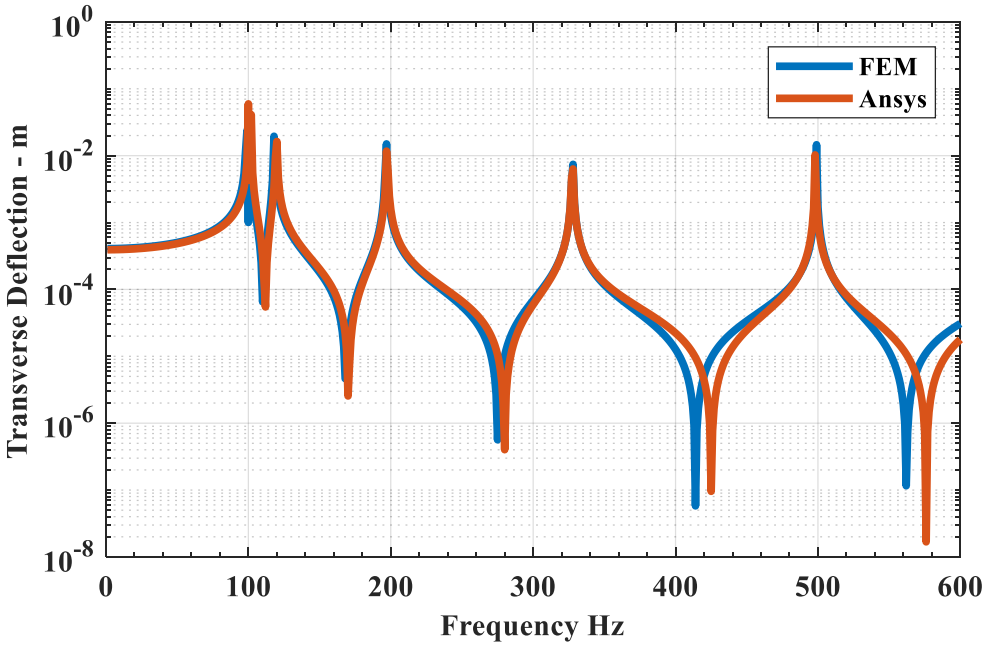

Figure 2.17: Collocated frequency response of brake disc prototype

2.6.2 Design of Stationary Disc Brake System

Disc brake system includes brake disc and brake pads. The contact effect of the pads leads to dynamic instability in the system and therefore squealing noise. It is therefore essential to design the brake pads of the prototype to produce dynamic instability.

The effect of the contact pads of the adopted brake system model discussed in Chapter 2 is summarized in the contact stiffness parameter k_c, contact area A_c and contact angle θ_c. The contact stiffness parameter is optimized in this section to produce dynamic instability in the brake system. Such a process is done using an iterative approach. The dimensions of the contact region are assumed to be proportional to those in commercial automobiles. The critical coefficient of friction between the brake disc and the pads is assumed to be 0.4. Table 2.9 presents the contact region dimensions in the new prototype and the effect of varying contact stiffness k_c on the first five doublet modes is demonstrated in Figure 2.18.

Table 2.9: Contact region dimensions of brake pads in disc brake system prototype

Parameter	Symbol	Value
Outer radius of contact area	r_{c_o}	110 mm
Inner radius of contact area	r_{c_i}	80 mm
Contact angle	θ_c	60^o

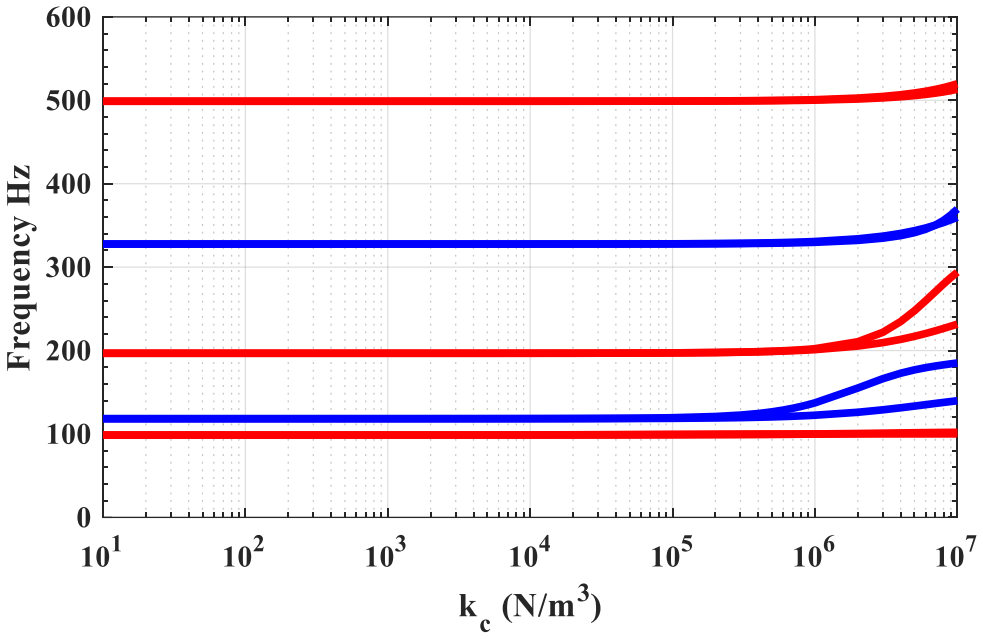

Figure 2.18: Frequency plot of the effect of varying contact stiffness k_C on the first five doublet modes in the new prototype

Doublet modes 2 and 3 experience frequency separation at contact stiffness range of 10^5 to 10^7 (N/m^3). However to demonstrate the dynamic instability, it is essential to solve for the real parts of the system eigenvalues. The effect of varying the contact stiffness on dynamic instability of modes 2 and 3 is shown in Figure 2.19.

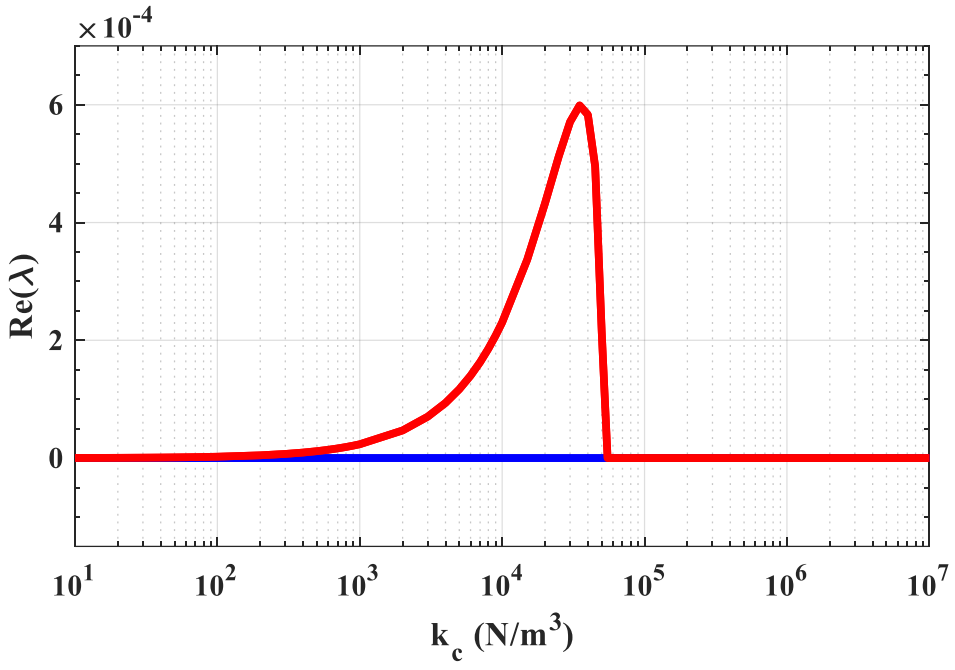

Figure 2.19: Effect of varying contact stiffness k_C on the dynamic instability of doublet modes 2 (-) and 3 (-) in the new prototype

It is obvious from Figure 2.19 that doublet mode 2 is marginally stable and that doublet mode 3 becomes unstable when k_c is between 10^2 and 10^5 (N/m^3). Therefore, doublet mode 3 is the mode that is going to cause brake squeal and the maximum instability occurs at critical contact stiffness $k_c = 5x10^4\ (N/m^3)$.

Figures 2.20 and 2.21 illustrate the stability of the transverse doublet mode 3 and the corresponding mode-coupling frequency behavior in the new disc brake system prototype. It should be noted here that the maximum frequency separation in mode 3 is 0.0025 Hz at $\mu = 0$.

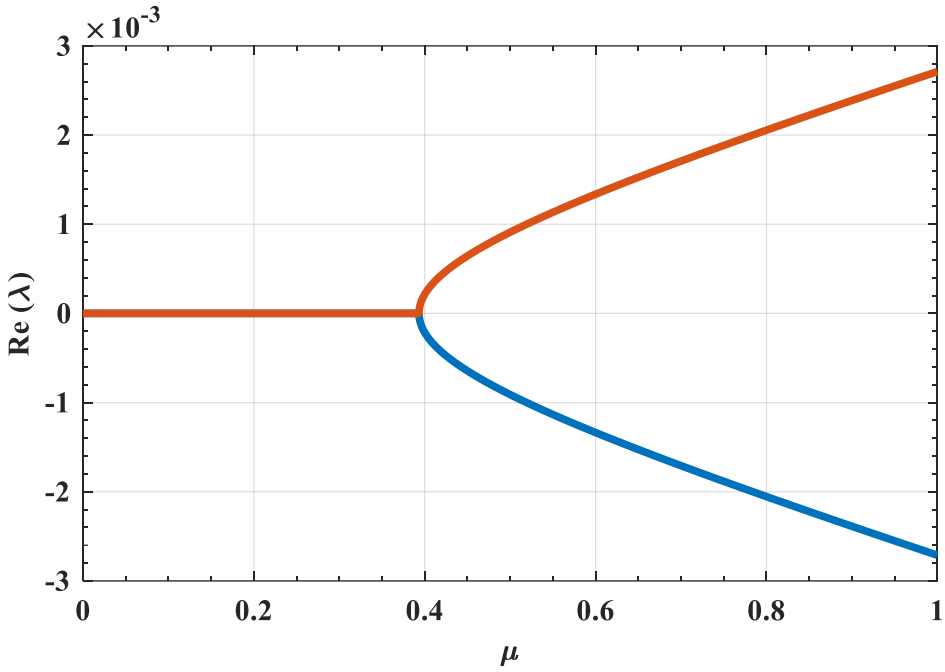

Figure 2.20: Stability of transverse doublet mode 3 in the new prototype

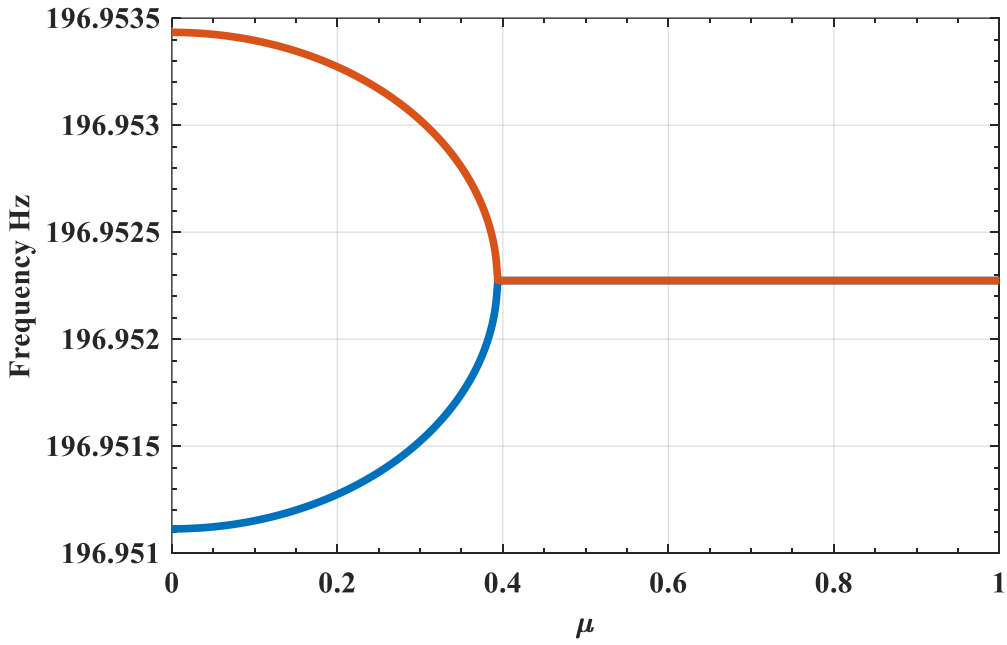

Figure 2.21: Mode-coupling behavior of transverse doublet mode 3 in the new prototype

2.6.3 Coriolis Effects on Brake Discs

The brake disc is a rotating component that experience Coriolis effects which may also play a role in the dynamic instability of the system. In this section, the brake disc is examined under the influence of Coriolis effects at different rotational speeds.

Table 2.10 presents the natural frequencies of the brake disc for different rotational speeds. The results are obtained using the developed *FEM* and compared against numerical solution of *ANSYS*® Workbench. Campbell diagram of the first five doublet modes under the influence of Coriolis effects is shown in Figure 2.22.

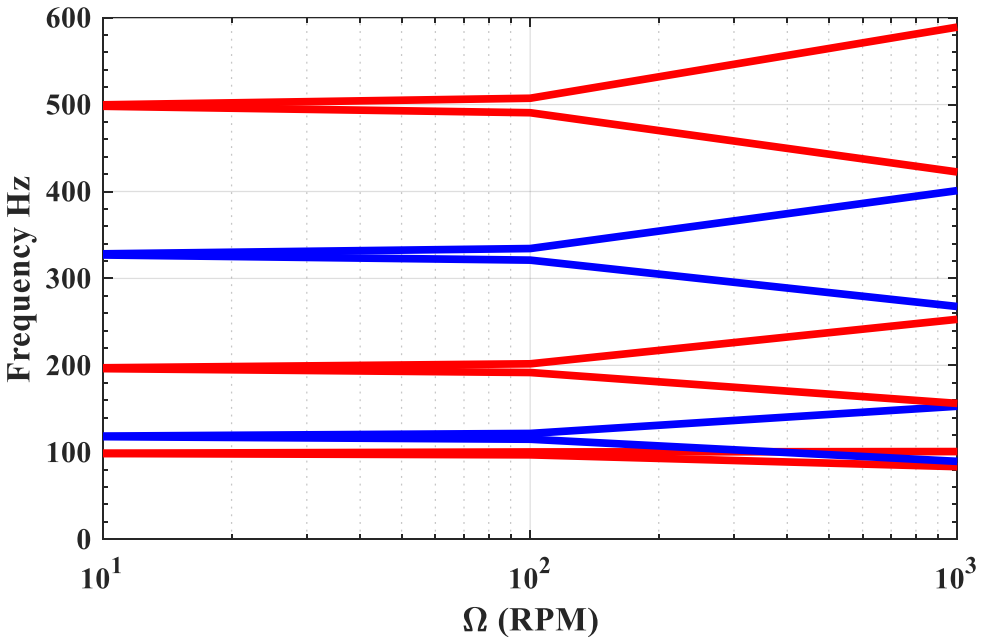

Figure 2.22: Campbell diagram including the first five doublet modes of the brake disc prototype

Table 2.10: Natural Frequencies of transverse doublet modes of new brake disc prototype at different rotational speeds

	Natural Frequency $f\ (Hz)$					
	$\Omega = 0\ RPM$		$\Omega = 100\ RPM$		$\Omega = 1000\ RPM$	
Doublet Modes						
n	*ANSYS®*	*FEM*	*ANSYS®*	*FEM*	*ANSYS®*	*FEM*
1	100.12	98.73	98.47	97.08	84.83	83.46
			101.80	100.41	90.84	89.58
2	119.62	118.31	116.33	115.02	118.17	116.79
			123.00	121.69	153.59	152.99
3	197.34	196.73	192.41	191.79	157.50	156.25
			202.40	201.79	253.56	252.99
4	327.58	327.64	320.98	321.04	267.65	267.69
			334.31	334.38	400.93	401.02
5	498.19	498.87	489.93	490.60	421.82	422.45
			506.59	507.27	588.39	589.11

The new brake disc prototype is influenced by Coriolis effects at high rotational speeds as shown in Campbell diagram. However, the Coriolis effects play a minor role at slow rotational speeds. Brake squeal normally occurs at very slow rotational speeds

(< 100 RPM) as reported in Ref. [22] and therefore in this study the gyroscopic effects are neglected.

2.7 Summary

This chapter has presented the development of a finite element model of a disc brake system based on Kirchhoff plate theory. The finite element formulations were integrated into a computational algorithm to obtain the vibration characteristics of the disc brake system. The validation of the generated *MATLAB*® routine was achieved by performing two numerical simulations. An insight into squeal propensity and flutter instability was demonstrated in simulation II. The chapter has also presented a new design of a disc brake system prototype that is capable of producing brake squeal features in laboratories. The influence of Coriolis effects on the dynamic instability at slow rotational speeds was found to be negligible.

Chapter 3: Shunted Piezoelectric Networks

3.1 Overview

Piezoelectric shunt damping is a popular technique for vibration suppression in smart structures. The damping is achieved by placing an electrical impedance across the terminals of a piezoelectric transducer, which is normally bonded to the flexible mechanical structure. By designing an appropriate electrical impedance across the terminals of the transducer, the circuit network is capable of increasing the mechanical damping of the host structure.

In this chapter, the theory of shunted piezoelectric networks is presented and applied to the disc brake system in an attempt to minimize the friction-induced vibration, maximize the stability of the unstable modes that result in squeal noise and harvest the dissipated energy. Numerical examples of shunted disc brake systems are provided and compared with the conventional disc brake models discussed in Chapter 1 and Chapter 2.

3.2 Piezoelectricity

Piezoelectricity refers to the generation of electricity under mechanical pressure. Piezoelectric elements have the unique ability to transfer mechanical energy into electrical energy and vice versa. This section summarizes the piezoelectric effects, constitutive relations and electromechanical coupling efficiency.

3.2.1 Fundamentals of Piezoelectricity

Piezoelectric effects can be summarized as direct effect and converse effect. A strict definition of the direct effect is "electric polarization produced by mechanical strain, being directly proportional to the applied strain." A converse effect also exists and is the appearance of mechanical strain as a result of an applied electric field [64]. As seen in Figure 3.1, direct effect makes the piezo film act as a sensor whereas converse effect makes it act as an actuator.

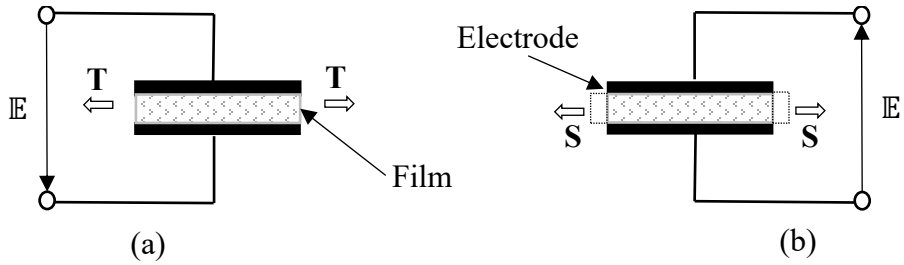

Figure 3.1: Piezoelectric effects; (a) direct effect (b) converse effect

The piezoelectric effect can be expressed in terms of constitutive relations as

$$S_i = s_{ij}^{\mathbb{E}}\, T_j + d_{ik}\, \mathbb{E}_k \tag{3.1}$$

$$D_k = d_{ki}\, T_i + \varepsilon_{kl}^{T}\, \mathbb{E}_l \tag{3.2}$$

where S_i is the mechanical strain vector, T_j is the mechanical stress vector, ε_{kl}^{T} is the permittivity matrix, $s_{ij}^{\mathbb{E}}$ is the compliance matrix, and d_{ik} or d_{ki} is the piezoelectric coefficients matrix.

3.2.2 Piezoceramic Constitutive Relations

The discovery of piezoceramics exhibiting much larger piezo effect than natural materials expanded the domain of applications considerably. They can be

manufactured easily in large quantities and in specific shapes, which makes them ideally suited for adaptive-structures applications [64]. The most commonly used piezoceramics are based on PZT compounds. Therefore, the remainder of this study focusses on the properties and constitutive equations of a typical PZT composition, PZT-5H and PZT-5A.

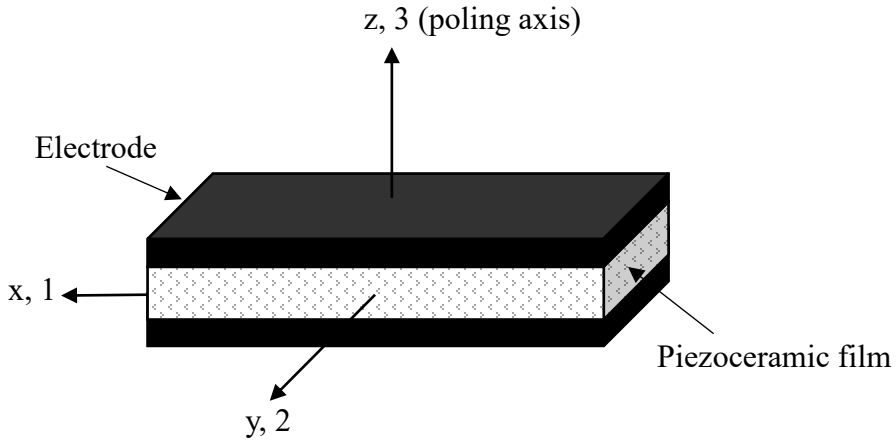

Figure 3.2: Piezoceramic sheet with coordinate axes

A typical piezoceramic sheet is shown in Figure 3.2. The initial polarization direction is expressed as the z-axis (or 3-axis). The axes x and y (or 1-axis and 2-axis) are defined in a plane normal to the z-axis, in a conventional right-handed system. The constitutive relations of a piezoceramic sheet are given in equations (3.1) and (3.2). However, due to the specific crystal structure of PZT, several elements of the coefficient matrices become equal to each other or to zero. Considering an isotropic piezoceramic sheet, the constitutive relations are

$$\{S\} = [s^{\mathbb{E}}]\{T\} + [d^c]\,\{\mathbb{E}\} \tag{3.3}$$

$$\{D\} = [d^d]\,\{T\} + [\varepsilon^T]\{\mathbb{E}\} \tag{3.4}$$

where

$\{S\}$, is the mechanical strain vector given as

$$\{S\}^T = \{S_1 \quad S_2 \quad S_3 \quad \gamma_{23} \quad \gamma_{31} \quad \gamma_{12}\} \tag{3.5}$$

$\{T\}$ (N/m^2), is the mechanical stress vector given as

$$\{T\}^T = \{T_1 \quad T_2 \quad T_3 \quad \tau_{23} \quad \tau_{31} \quad \tau_{12}\} \tag{3.6}$$

$\{\mathbb{E}\}$ (V/m) or (N/C), is the electric field vector given as

$$\{\mathbb{E}\}^T = \{\mathbb{E}_1 \quad \mathbb{E}_2 \quad \mathbb{E}_3\} \tag{3.7}$$

$\{D\}$ (C/m^2), is the electric displacement vector given as

$$\{D\}^T = \{D_1 \quad D_2 \quad D_3\} \tag{3.8}$$

$[s^{\mathbb{E}}]$ (m^2/N), is the compliance matrix given as

$$[s^{\mathbb{E}}] = \begin{bmatrix} s_{11}^{\mathbb{E}} & s_{12}^{\mathbb{E}} & s_{13}^{\mathbb{E}} & 0 & 0 & 0 \\ s_{12}^{\mathbb{E}} & s_{11}^{\mathbb{E}} & s_{13}^{\mathbb{E}} & 0 & 0 & 0 \\ s_{13}^{\mathbb{E}} & s_{13}^{\mathbb{E}} & s_{33}^{\mathbb{E}} & 0 & 0 & 0 \\ 0 & 0 & 0 & s_{44}^{\mathbb{E}} & 0 & 0 \\ 0 & 0 & 0 & 0 & s_{44}^{\mathbb{E}} & 0 \\ 0 & 0 & 0 & 0 & 0 & s_{66}^{\mathbb{E}} \end{bmatrix} \tag{3.9}$$

$[d^c] = [d^d]^T$ (m/V) or (C/N), is the piezoelectric coefficient matrix given as

$$[d^c] = [d^d]^T = \begin{bmatrix} 0 & 0 & d_{31} \\ 0 & 0 & d_{32} \\ 0 & 0 & d_{33} \\ 0 & d_{24} & 0 \\ d_{15} & 0 & 0 \\ 0 & 0 & 0 \end{bmatrix} \tag{3.10}$$

$[\varepsilon^T]$ (F/m) or (C^2/N-m^2), is electric permittivity matrix given as

$$[\varepsilon^T] = \begin{bmatrix} \varepsilon_{11}^T & 0 & 0 \\ 0 & \varepsilon_{11}^T & 0 \\ 0 & 0 & \varepsilon_{33}^T \end{bmatrix} \tag{3.11}$$

The electric voltage is directly proportional to the electric field by the thickness

$$V_k = t_k \mathbb{E}_k \tag{3.12}$$

where the subscript $k = 1, 2$ and 3 represents the direction of the electric field. In addition, the relationship between the electric current and the electric displacement is given by

$$D_k = \frac{1}{A} Q_k = \frac{1}{A} \int I_k \, dt = \frac{I_k}{A \, s} \tag{3.13}$$

where $k = 1, 2$ and 3 represents the direction of the electric displacement and the electric current. A is the area perpendicular to the direction of the electric displacement and s is Laplace complex number. Using equations (3.12) and (3.13), the constitutive relations given in equations (3.3) and (3.4) can be expressed in terms of the electric voltage and current. The actuator constitutive relations are therefore

$$\begin{Bmatrix} S_1 \\ S_2 \\ S_3 \\ \gamma_{23} \\ \gamma_{31} \\ \gamma_{12} \end{Bmatrix} = \begin{bmatrix} s_{11}^{\mathbb{E}} & s_{12}^{\mathbb{E}} & s_{13}^{\mathbb{E}} & 0 & 0 & 0 \\ s_{12}^{\mathbb{E}} & s_{11}^{\mathbb{E}} & s_{13}^{\mathbb{E}} & 0 & 0 & 0 \\ s_{13}^{\mathbb{E}} & s_{13}^{\mathbb{E}} & s_{33}^{\mathbb{E}} & 0 & 0 & 0 \\ 0 & 0 & 0 & s_{44}^{\mathbb{E}} & 0 & 0 \\ 0 & 0 & 0 & 0 & s_{44}^{\mathbb{E}} & 0 \\ 0 & 0 & 0 & 0 & 0 & s_{66}^{\mathbb{E}} \end{bmatrix} \begin{Bmatrix} T_1 \\ T_2 \\ T_3 \\ \tau_{23} \\ \tau_{31} \\ \tau_{12} \end{Bmatrix} + \begin{bmatrix} 0 & 0 & d_{31}/t_3 \\ 0 & 0 & d_{32}/t_3 \\ 0 & 0 & d_{33}/t_3 \\ 0 & d_{24}/t_2 & 0 \\ d_{15}/t_1 & 0 & 0 \\ 0 & 0 & 0 \end{bmatrix} \begin{Bmatrix} V_1 \\ V_2 \\ V_3 \end{Bmatrix} \tag{3.14}$$

and the sensor constitutive relations are

$$\begin{Bmatrix} I_1 \\ I_2 \\ I_3 \end{Bmatrix} = \begin{bmatrix} 0 & 0 & 0 & 0 & d_{15} A_{23}\, s & 0 \\ 0 & 0 & 0 & d_{24}\, A_{13}\, s & 0 & 0 \\ d_{31}\, A_{12}\, s & d_{32}\, A_{12}\, s & d_{33}\, A_{12}\, s & 0 & 0 & 0 \end{bmatrix} \begin{Bmatrix} T_1 \\ T_2 \\ T_3 \\ \tau_{23} \\ \tau_{31} \\ \tau_{12} \end{Bmatrix} + \begin{bmatrix} \dfrac{\varepsilon_{11}^{T}\, A_{23}\, s}{t_1} & 0 & 0 \\ 0 & \dfrac{\varepsilon_{11}^{T}\, A_{13}\, s}{t_2} & 0 \\ 0 & 0 & \dfrac{\varepsilon_{33}^{T}\, A_{12}\, s}{t_3} \end{bmatrix} \begin{Bmatrix} V_1 \\ V_2 \\ V_3 \end{Bmatrix} \tag{3.15}$$

3.2.3 Piezoelectric Coupling Coefficients

A piezoelectric transducer is basically an energy-conversion device. The direct piezoelectric effect results in the conversion of mechanical energy into electrical energy, whereas the converse piezoelectric effect results in the conversion of electrical energy into mechanical energy. The coupling coefficients k_{ij} are a measure of the efficiency of this energy conversion. To illustrate the significance of coupling, a simple one-dimensional analysis is described in this section.

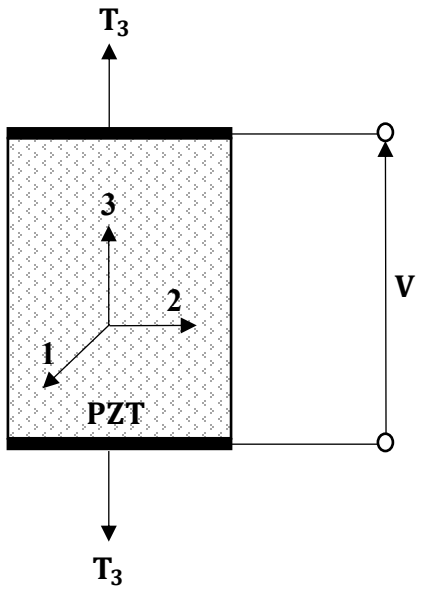

Figure 3.3: one-dimensional piezoceramic sheet

The one-dimensional constitutive relations along the 3-axis for the piezoceramic sheet shown in Figure 3.3 are given as

$$\begin{Bmatrix} S_3 \\ D_3 \end{Bmatrix} = \begin{bmatrix} s_{33}^{\mathbb{E}} & d_{33} \\ d_{33} & \varepsilon_{33}^{T} \end{bmatrix} \begin{Bmatrix} T_3 \\ \mathbb{E}_3 \end{Bmatrix} \tag{3.16}$$

or in terms of the electric voltage and current as

$$\begin{Bmatrix} S_3 \\ I_3 \end{Bmatrix} = \begin{bmatrix} s_{33}^{\mathbb{E}} & \dfrac{d_{33}}{t_3} \\ s\, d_{33} A_{12} & s\, \varepsilon_{33}^{T} \dfrac{A_{12}}{t_3} \end{bmatrix} \begin{Bmatrix} T_3 \\ V_3 \end{Bmatrix} = \begin{bmatrix} s_{33}^{\mathbb{E}} & \dfrac{d_{33}}{t_3} \\ s\, d_{33} A_{12} & Y^D \end{bmatrix} \begin{Bmatrix} T_3 \\ V_3 \end{Bmatrix} \tag{3.17}$$

where $Y^D = s\, C^T$ is the admittance of the piezoceramic sheet in Siemens (1/Ω) and Ω is Ohm. C^T is the capacitance of the piezoceramic sheet given as

$$C^T = \varepsilon_{33}^T \frac{A_{12}}{t_3} \tag{3.18}$$

The piezoceramic sheet is subjected to mechanical and electrical boundary conditions. Electrical boundary conditions are short circuit BC (V = 0) and open circuit BC (I = 0). For the short circuit boundary condition

$$S_3 = s_{33}^{\mathbb{E}}\, T_3 \tag{3.19}$$

And for the open circuit boundary condition

$$V_3 = -\frac{d_{33}\, t_3}{\varepsilon_{33}^T}\, T_3 \tag{3.20}$$

Substituting equations (3.19) and (3.20) into equation (3.17) yields

$$S_3 = s_{33}^{\mathbb{E}}\, [1 - k_{33}^2\,] T_3 = s_{33}^D T_3 \tag{3.21}$$

where k_{33} is the electromechanical coupling factor which defines the relationship of mechanical energy stored in 3-direction and electrical energy applied in 3-direction

$$k_{33}^2 = \frac{d_{33}^2}{s_{33}^{\mathbb{E}}\, \varepsilon_{33}^T} \tag{3.22}$$

and s_{33}^D is the compliance of the material in 3-direction at a constant electric displacement

$$s_{33}^D = s_{33}^{\mathbb{E}}\, [1 - k_{33}^2\,] \tag{3.23}$$

3.3 Shunted Piezoceramic Networks

3.3.1 Electrical Basics

Basic electrical components including resistors, capacitors and inductors are mathematically equivalent to mechanical components. Table 3.1 explains the similarity and summarizes the constitutive equations for various electrical components along with their electrical impedance.

Table 3.1: Constitutive equations of electrical components

Mechanical Element	Electrical Element	Source	Electrical Voltage $\boldsymbol{v(t)}$	Electrical Impedance Z(s)
Mass	Inductor	Inertia	$L\frac{di}{dt}$	$L\ s$
Damper	Resistor	Damping	$R\ i(t)$	R
Spring	Capacitor	Stiffness	$\frac{1}{C}\int i(t)\ dt$	$\frac{1}{C\ s}$

3.3.2 Basics of Shunted Piezoelectric Networks

Figure 3.4 shows a piezocermaic sheet with a shunted circuit that has an admittance of $Y^{SH}(s)$.

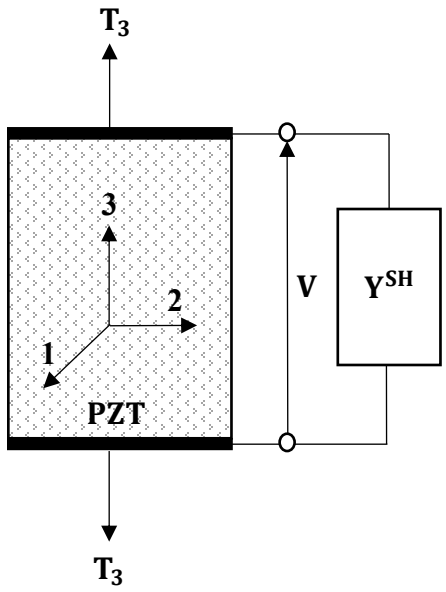

Figure 3.4: Shunted piezoceramic network

The one-dimensional constitutive relations along the 3-axis for the piezoceramic sheet are expressed in equation (3.17). The shunt constitutive relations is given in matrix form as

$$\begin{Bmatrix} S_3 \\ I_3 \end{Bmatrix} = \begin{bmatrix} 0 & 0 \\ 0 & Y^{SH} \end{bmatrix} \begin{Bmatrix} T_3 \\ V_3 \end{Bmatrix} \tag{3.24}$$

The combined effect of shunted piezoceramic network is then expressed as

$$\begin{Bmatrix} S_3 \\ I_3 \end{Bmatrix} = \begin{bmatrix} s_{33}^{\mathbb{E}} & \dfrac{d_{33}}{t_3} \\ s\, d_{33} A_{12} & Y^D + Y^{SH} \end{bmatrix} \begin{Bmatrix} T_3 \\ V_3 \end{Bmatrix} = \begin{bmatrix} s_{33}^{\mathbb{E}} & \dfrac{d_{33}}{t_3} \\ s\, d_{33} A_{12} & Y^{EL} \end{bmatrix} \begin{Bmatrix} T_3 \\ V_3 \end{Bmatrix} \tag{3.25}$$

where $Y^{EL} = Y^D + Y^{SH}$ is the admittance of the parallel combination of piezoceramic sheet and a shunted circuit. The effect of the shunted network on the constitutive

relations of the piezoceramic sheet can be determined by considering open circuit boundary condition ($I = 0$) as

$$V_3 = -\frac{s\, d_{33}\, A_{12}}{Y^{EL}}\, T_3 \tag{3.26}$$

Substituting equation (3.26) into equation (3.25) yields

$$S_3 = s_{33}^{\mathbb{E}}\left[1 - k_{33}^2\, \frac{Y^D}{Y^{EL}}\right] T_3 = s_{33}^{\mathbb{E}}[1 - k_{33}^2\, \bar{Y}^{EL}]\, T_3 = s^{SH}\, T_3 \tag{3.27}$$

where $\bar{Y}^{EL}$ is the admittance ratio of the piezoceramic sheet to the total shunted piezoceramic network and s^{SH} is the compliance of the shunted piezoceramic network expressed as

$$\bar{Y}^{EL} = \frac{Y^D}{Y^{EL}} = \frac{Z^{EL}}{Z^D} = \bar{Z}^{EL} \tag{3.28}$$

$$s^{SH} = s_{33}^{\mathbb{E}}\left[1 - k_{33}^2\, \frac{Y^D}{Y^{EL}}\right] \tag{3.29}$$

Comparing equations (3.23) and (3.29) indicates that the compliance of the piezoceramic sheet is real whereas the compliance of the shunted piezoceramic network can be complex depending on the configuration of the shunted circuit. Accordingly, the piezoceramic sheet has an elastic modulus of $1/s_{33}^D$ whereas the shunted piezoceramic network has a complex elastic modulus of $1/s^{SH}$. Hence, the shunted piezoceramic network has a storage modulus as well as a loss factor and acts as a conventional viscoelastic damping material.

Equation (3.21) can be expressed in terms of force and deflection as

$$F_3 = K^D \Delta L_3 \tag{3.30}$$

where K^D is the stiffness of the piezoceramic sheet (real)

$$k^D = \frac{A_{12}}{s_{33}^D \, L_3} \tag{3.31}$$

Similarly, expressing equation (3.27) in terms of force and deflection yields

$$F_3 = K^{SH} \Delta L_3 \tag{3.32}$$

and K^{SH} is the stiffness of the shunted piezoceramic network

$$K^{SH} = \frac{A_{12}}{s^{SH} \, L_3} = k^p \frac{1}{[1 - k_{33}^2 \, \bar{Y}^{EL}]} \tag{3.33}$$

where k^p is the stiffness of the passive piezoceramic sheet (spring)

$$k^p = \frac{A_{12}}{s_{33}^{\mathbb{E}} \, L_3} \tag{3.34}$$

A better quantification of the effect of shunting a piezoceramic sheet on its mechanical characteristics can be achieved by considering the concept of mechanical impedance Z^{ME} which is defined as

$$Z^{ME} = \frac{Force}{Velocity} = \frac{F}{\dot{x}} = \frac{F}{s \, X(s)} = \frac{stiffness}{s} \tag{3.35}$$

For one-dimensional piezoceramic sheet, the stiffness is given in equation (3.31). Therefore the mechanical impedance becomes

$$Z^{ME} = \frac{k^D}{s} \tag{3.36}$$

The ratio of the mechanical impedance of the shunted network to that of the open-circuit piezoceramic sheet is denoted $\bar{Z}^{ME}$ and is expressed as

$$\bar{Z}^{ME} = \frac{(Z^{ME})^{SH}}{(Z^{ME})^{D}} = \frac{(1 - k_{33}^2)}{(1 - k_{33}^2\ \bar{Z}^{EL})} \tag{3.37}$$

3.3.3 Shunted Piezoceramic Networks

Shunted piezoceramic networks come in different forms depending on the circuit configuration which includes resistive shunted circuits, resistive and inductive shunted circuits and *RLC* shunted circuits. In this section, the simplest form with a resistive circuit is considered. For a resistive shunt *R*,

$$\bar{Y}^{EL} = \frac{C^T R\ \ s}{C^T R\ \ s + 1} \tag{3.38}$$

Substituting equation (3.38) into equation (3.33) yields

$$K^{SH} = k^p \left[\frac{C^T R\ \ s + 1}{(1 - k_{33}^2)\ C^T R\ \ s + 1} \right] = k^p \left[\frac{\tau s + 1}{(1 - k_{33}^2)\ \tau s + 1} \right] \tag{3.39}$$

where $\tau = C^T R$ has unit of seconds and K^{SH} is the complex stiffness of the shunted piezoceramic network. Figure 3.5 shows a piezoceramic sheet with a resistive shunt.

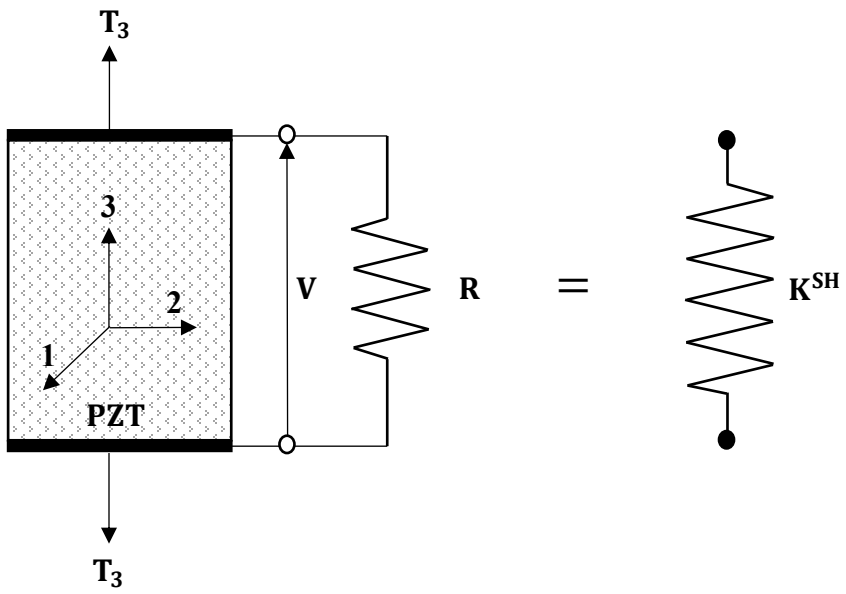

Figure 3.5: Resistive Shunted Piezoceramic patch

The mechanical impedance ratio is determined for a resistive shunt from equation (3.37) as

$$\bar{Z}^{ME} = \frac{C^s R\ s + (1 - k_{33}^2)}{C^s R\ s + 1} \tag{3.40}$$

where $C^s = (1 - k_{33}^2)\ C^T$. $\bar{Z}^{ME}$ can be expressed in frequency domain, by replacing s with $j\omega$ as

$$\bar{Z}^{ME} = \frac{C^s R\ j\omega + (1 - k_{33}^2)}{C^s R\ j\omega + 1} \tag{3.41}$$

Let $\Omega = C^s R\ \omega$ be a dimensionless frequency, then the above equation reduces to

$$\bar{Z}^{ME} = \frac{(1 - k_{33}^2) + j\ \Omega}{1 + j\ \Omega} = E'[1 + j\ \eta] \tag{3.42}$$

where E' is the dimensionless storage modulus and η is the dimensionless loss factor given as

$$E' = 1 - \frac{k_{33}^2}{1 + \Omega^2} \tag{3.43}$$

$$\eta = \frac{k_{33}^2\ \Omega}{(1 - k_{33}^2) + \Omega^2} \tag{3.44}$$

The loss factor is maximum when

$$\frac{d\eta}{d\Omega} = 0 \tag{3.45}$$

which occurs at a dimensionless frequency

$$\Omega^* = \sqrt{1 - k_{33}^2} \tag{3.46}$$

and the corresponding maximum loss factor

$$\eta^{max} = \frac{k_{33}^2}{2\sqrt{1 - k_{33}^2}} \tag{3.47}$$

It is therefore essential to use a piezoceramic sheet with high electro-mechanical coupling factor to achieve the highest possible loss factor. For maximum loss factor

$$\tau = \frac{1}{2\,\pi\sqrt{1 - k_{33}^2}\,f_{Hz}} \tag{3.48}$$

3.4 Modeling Disc Brake Systems with Shunted Piezoceramic Networks

This section is devoted to the integration of shunted piezoceramic networks in disc brake systems. Different models are considered and modal analysis and disc brake system stability are covered. FE formulation of disc brake system shunted with one-dimensional piezoceramic network is discussed.

3.4.1 Brake systems with 1-D Shunted Piezoceramic Network

Shunted piezoceramic networks are integrated with the minimal model by Hoffmann *et al.* [17] discussed in section 1.2.3.

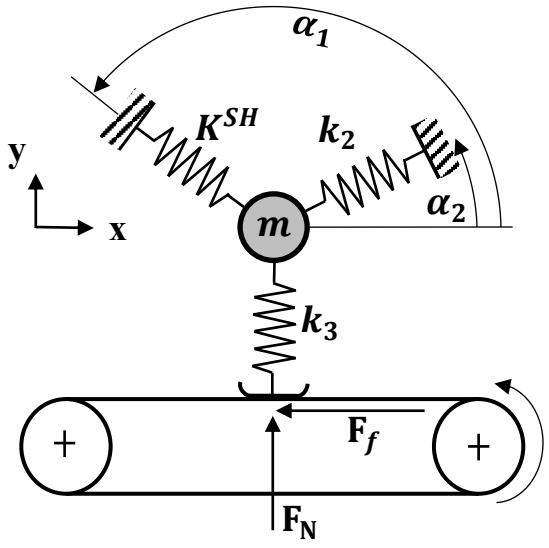

Figure 3.6: Modified minimal model for disc brake squeal with shunted piezoceramic spring

The modified model is shown in Figure 3.6 with one of the springs replaced by a shunted piezoceramic spring. The system equations of motion given in equation (1.8)

are modified by replacing k_1 with K^{SH} given in equation (3.39). The passive piezoceramic spring is assumed to have an equal stiffness of the replaced spring $k^p = k_1$. The new system equations of motion are expressed as

$$\begin{bmatrix} m & 0 \\ 0 & m \end{bmatrix} \begin{Bmatrix} \ddot{x} \\ \ddot{y} \end{Bmatrix} + \begin{bmatrix} K_{11} & K_{12} - \mu k_3 \\ K_{12} & K_{22} \end{bmatrix} \begin{Bmatrix} x \\ y \end{Bmatrix} = \begin{Bmatrix} 0 \\ 0 \end{Bmatrix} \tag{3.49}$$

where

$$K_{11} = \frac{k_{11} + \bar{k}_{11}\, \tau\, s}{(1 - k_{33}^2)\, \tau\, s + 1}$$

$$k_{11} = k_1 \cos^2 \alpha_1 + k_2 \cos^2 \alpha_2$$

$$\bar{k}_{11} = k_1 \cos^2 \alpha_1 + (1 - k_{33}^2)\, k_2 \cos^2 \alpha_2$$

And

$$K_{12} = \frac{k_{12} + \bar{k}_{12}\, \tau\, s}{(1 - k_{33}^2)\, \tau\, s + 1}$$

$$k_{12} = k_1 \cos \alpha_1 \sin \alpha_1 + k_2 \cos \alpha_2 \sin \alpha_2$$

$$\bar{k}_{12} = k_1 \cos \alpha_1 \sin \alpha_1 + (1 - k_{33}^2)\, k_2 \cos \alpha_2 \sin \alpha_2$$

And

$$K_{22} = \frac{k_{22} + \bar{k}_{22}\, \tau\, s}{(1 - k_{33}^2)\, \tau\, s + 1}$$

$$k_{22} = k_1 \sin^2 \alpha_1 + k_2 \sin^2 \alpha_2 + k_3$$

$$\bar{k}_{22} = k_1 \sin^2 \alpha_1 + (1 - k_{33}^2)\, k_2 \sin^2 \alpha_2 + (1 - k_{33}^2)\, k_3$$

Expressing the system equations (3.49) in Laplace domain and multiplying by the denominator $[(1 - k_{33}^2)\, \tau\, s + 1]$ then writing the system back in time domain yields a new representation of the system equations as third order differential equations

$$[a_1]\{\dddot{\Delta}\} + [a_2]\{\ddot{\Delta}\} + [a_3]\{\dot{\Delta}\} + [a_4]\{\Delta\} = \{0\} \tag{3.50}$$

where

$$\{\Delta(t)\} = \begin{Bmatrix} x(t) \\ y(t) \end{Bmatrix}$$

$$[a_1] = (1 - k_{33}^2)\,\tau \begin{bmatrix} m & 0 \\ 0 & m \end{bmatrix}$$

$$[a_2] = [M] = \begin{bmatrix} m & 0 \\ 0 & m \end{bmatrix}$$

$$[a_3] = \tau \begin{bmatrix} \bar{k}_{11} & \bar{k}_{12} - \mu k_3 (1 - k_{33}^2) \\ \bar{k}_{12} & \bar{k}_{22} \end{bmatrix}$$

$$[a_4] = \begin{bmatrix} k_{11} & k_{12} - \mu k_3 \\ k_{12} & k_{22} \end{bmatrix}$$

In order to study the system stability, the equations of motion in equation (3.50) are casted in state space form as in equation (2.68). Here the system matrix $[\mathbf{A}]$ is given by

$$[\mathbf{A}] = \begin{bmatrix} [0] & [I] & [0] \\ [0] & [0] & [I] \\ -[a_1]^{-1}\,[a_4] & -[a_1]^{-1}\,[a_3] & -[a_1]^{-1}\,[a_2] \end{bmatrix} \tag{3.51}$$

3.4.2 FE Model with Shunted Piezoceramic Networks

The *FEM* developed in section 2.3 is considered in this section. The disc-pad contact represented by distributed springs is replaced by distributed shunted piezoceramic springs as shown in Figure 3.7.

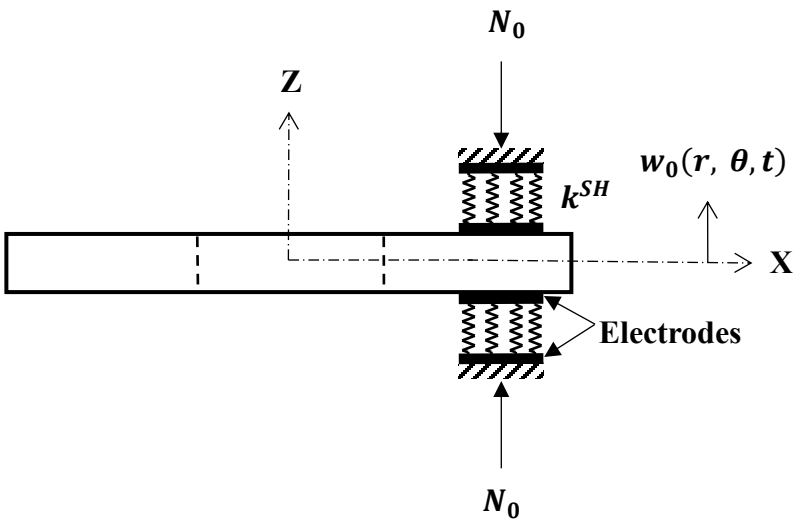

Figure 3.7: Modified disc brake system with shunted piezoceramic interface

The overall system equations are given in equation (2.60) as

$$[M_o]\{\ddot{\Delta}_o\} + [G_o]\{\dot{\Delta}_o\} + ([K_o] + [A_o] + [B_o] - [R_o])\{\Delta_o\} = \{0\}$$

The disc-pad contact is represented in matrices $[A_o]$ and $[B_o]$. Both matrices have common terms and can be expressed using equation (2.53) as

$$[M_o]\{\ddot{\Delta}_o\} + [G_o]\{\dot{\Delta}_o\} + ([K_o] + k_c[\bar{A}_o] + \mu k_c[\bar{B}_o] - [R_o])\{\Delta_o\} = \{0\} \quad (3.52)$$

Replacing the distributed springs k_c by K^{SH} given in equation (3.39) with $k^p = k_c$ and multiplying by the denominator $[(1 - k_{33}^2)\,\tau s + 1]$ yields a new third order system differential equations

$$[a_1]\{\dddot{\Delta}_o\} + [a_2]\{\ddot{\Delta}_o\} + [a_3]\{\dot{\Delta}_o\} + [a_4]\{\Delta_o\} = \{0\} \quad (3.53)$$

where

$$[a_1] = (1 - k_{33}^2)\,\tau\,[M_o]$$

$$[a_2] = [M_o] + (1 - k_{33}^2)\,\tau\,[G_o]$$

$$[a_3] = [G_o] + \tau\,([A_o] + [B_o]) + (1 - k_{33}^2)\,\tau\,([K_o] - [R_o])$$

$$[a_4] = [K_o] + [A_o] + [B_o] - [R_o]$$

The stability analysis can then be performed using equation (3.51).

3.4.3 Coupled Electromechanical Field Approach of Shunted Piezoceramic Networks

In this approach, both the structural and the electrical degrees of freedom will be simultaneously considered to describe the interaction between the dynamics of the shunted piezoceramic networks and the vibrating structure. The equations governing such an interaction are based on rewriting the constitutive relations of the piezoceramic sheet in equations (3.3) and (3.4). The piezoceramic patch is modelled as a 2D Kirchhoff plate which follows the Kirchhoff Plate Theory assumptions mentioned earlier in section 2.2.1. The displacements field and the stress-strain relations will also be the same as covered in sections 2.2.2 and 2.2.3. However, due to the coupling between the mechanical and electrical degrees of freedom, the piezoceramic plate will also have some coupling constants as well as electrical properties. Therefore, equations (3.3) and (3.4) become:

$$\begin{Bmatrix} S_1 \\ S_2 \\ \gamma_{12} \\ \cdots \\ D_1 \\ D_2 \\ D_3 \end{Bmatrix} = \begin{bmatrix} s_{11}^{\mathbb{E}} & s_{12}^{\mathbb{E}} & 0 & \vdots & 0 & 0 & d_{31} \\ s_{12}^{\mathbb{E}} & s_{11}^{\mathbb{E}} & 0 & \vdots & 0 & 0 & d_{31} \\ 0 & 0 & s_{66}^{\mathbb{E}} & \vdots & 0 & 0 & 0 \\ \cdots & \cdots & \cdots & \cdots & \cdots & \cdots & \cdots \\ 0 & 0 & 0 & \vdots & \varepsilon_{11}^{T} & 0 & 0 \\ 0 & 0 & 0 & \vdots & 0 & \varepsilon_{11}^{T} & 0 \\ d_{31} & d_{31} & 0 & \vdots & 0 & 0 & \varepsilon_{33}^{T} \end{bmatrix} \begin{Bmatrix} T_1 \\ T_2 \\ \tau_{12} \\ \cdots \\ \mathbb{E}_1 \\ \mathbb{E}_2 \\ \mathbb{E}_3 \end{Bmatrix} \tag{3.54}$$

The focus in this study is to generate electrical charge in the 3 direction as this direction has the largest surface area. Therefore, the generated charges in 1 and 2 directions will be neglected. This will reduce equation (3.54) to

$$\begin{Bmatrix} \{S\} \\ \cdots \\ D_3 \end{Bmatrix} = \begin{bmatrix} [s^{\mathbb{E}}] & \vdots & \{d_{31}\} \\ \cdots & \cdots & \cdots \\ \{d_{31}\}^T & \vdots & \varepsilon_{33}^{T} \end{bmatrix} \begin{Bmatrix} \{T\} \\ \cdots \\ \mathbb{E}_3 \end{Bmatrix}$$

$$\begin{Bmatrix} S_1 \\ S_2 \\ \gamma_{12} \\ \cdots \\ D_3 \end{Bmatrix} = \begin{bmatrix} s_{11}^{\mathbb{E}} & s_{12}^{\mathbb{E}} & 0 & \vdots & d_{31} \\ s_{12}^{\mathbb{E}} & s_{11}^{\mathbb{E}} & 0 & \vdots & d_{31} \\ 0 & 0 & s_{66}^{\mathbb{E}} & \vdots & 0 \\ \cdots & \cdots & \cdots & \cdots & \cdots \\ d_{31} & d_{31} & 0 & \vdots & \varepsilon_{33}^{T} \end{bmatrix} \begin{Bmatrix} T_1 \\ T_2 \\ \tau_{12} \\ \cdots \\ \mathbb{E}_3 \end{Bmatrix} \tag{3.55}$$

The previous equation can also be expressed as

$$\begin{Bmatrix} \{T\} \\ \cdots \\ \mathbb{E}_3 \end{Bmatrix} = \begin{bmatrix} [c^D] & \vdots & \{h_{31}\} \\ \cdots & \cdots & \cdots \\ \{h_{31}\}^T & \vdots & \varepsilon\varepsilon_{33}^{T} \end{bmatrix} \begin{Bmatrix} \{S\} \\ \cdots \\ D_3 \end{Bmatrix}$$

$$\begin{Bmatrix} T_1 \\ T_2 \\ \tau_{12} \\ \cdots \\ \mathbb{E}_3 \end{Bmatrix} = \begin{bmatrix} c_{11}^{D} & c_{12}^{D} & 0 & \vdots & h_{31} \\ c_{12}^{D} & c_{11}^{D} & 0 & \vdots & h_{31} \\ 0 & 0 & c_{66}^{D} & \vdots & 0 \\ \cdots & \cdots & \cdots & \cdots & \cdots \\ h_{31} & h_{31} & 0 & \vdots & \varepsilon\varepsilon_{33}^{T} \end{bmatrix} \begin{Bmatrix} S_1 \\ S_2 \\ \gamma_{12} \\ \cdots \\ D_3 \end{Bmatrix} \tag{3.56}$$

where

$$c_{11}^{D} = \frac{\varepsilon_{33}^{T}\, s_{11}^{\mathbb{E}} - d_{31}^{2}}{(s_{11}^{\mathbb{E}} - s_{12}^{\mathbb{E}})\,\{\varepsilon_{33}^{T}\,(s_{11}^{\mathbb{E}} + s_{12}^{\mathbb{E}}) - 2\,d_{31}^{2}\}}$$

$$c_{12}^{D} = \frac{d_{31}^{2} - \varepsilon_{33}^{T}\, s_{12}^{\mathbb{E}}}{(s_{11}^{\mathbb{E}} - s_{12}^{\mathbb{E}})\,\{\varepsilon_{33}^{T}\,(s_{11}^{\mathbb{E}} + s_{12}^{\mathbb{E}}) - 2\,d_{31}^{2}\}}$$

$$c_{66}^{D} = \frac{1}{s_{66}^{\mathbb{E}}}$$

are the elastic constants of the piezoceramic plate and

$$h_{31} = \frac{d_{31}}{2\,d_{31}^{2} - \varepsilon_{33}^{T}\,(s_{11}^{\mathbb{E}} + s_{12}^{\mathbb{E}})}$$

$$\varepsilon\varepsilon_{33}^{T} = \frac{(s_{11}^{\mathbb{E}} + s_{12}^{\mathbb{E}})}{\varepsilon_{33}^{T}\,(s_{11}^{\mathbb{E}} + s_{12}^{\mathbb{E}}) - 2\,d_{31}^{2}}$$

have the reciprocal units of piezoceramic coefficients and permittivity respectively.

The kinetic energy T_p of the piezoceramic plate can be determined as

$$T_p = \frac{1}{2}\,\rho_p\,h_p\int_0^{2\pi}\int_{r_i}^{r_o}\left[\frac{\partial w_0(r,\theta,t)}{\partial t}\right]^2 r\,dr\,d\theta \tag{3.57}$$

Discretizing equation (3.57) yields the piezoceramic element kinetic energy

$$T_p = \frac{1}{2}\left\{\dot{\Delta}^{e}\right\}^{T}\left(\rho_p\,h_p\int_0^{\beta_p}\int_{r_{i_p}}^{r_{o_p}}\{N\}^{T}\{N\}\,r\,dr\,d\theta\right)\left\{\dot{\Delta}^{e}\right\} \tag{3.58}$$

where r_{i_p} and r_{o_p} are the inner and outer radiuses of a single piezoceramic plate element and β_p is the element contact angle.

The potential energy U_p of the piezoceramic plate is derived as

$$U_p = \frac{1}{2}\iiint_V \{S\}^{T}\,\{T\}\,dV + \frac{1}{2}\iiint_V D_3\,\mathbb{E}_3\,dV \tag{3.59}$$

$$U_p = \frac{1}{2}\iiint_V \{S\}^T\,[c^D]\,\{S\}\,dV + \iiint_V \{S\}^T\,\{h_{31}\}\,D_3\,dV$$

$$+\frac{1}{2}\iiint_V \varepsilon\varepsilon_{33}^T\,D_3^2\,dV$$

Expanding the potential energy of the piezoceramic plate yields three terms. The first term is due to the mechanical strain of the piezoceramic plate, the second term is due to the coupling between the electrical and mechanical degrees of freedom, and the third term is associated with the electrical potential energy. Discretizing the three potential energy terms yields

$$U_{p_1} = \frac{1}{2}\,\{\Delta^e\}^T\left(I_z\int_0^{\beta_p}\int_{r_{i_p}}^{r_{o_p}}\{\bar{\varepsilon}^e\}^T\,[c^D]\,\{\bar{\varepsilon}^e\}\,r\,dr\,d\theta\right)\{\Delta^e\} \tag{3.60}$$

$$U_{p_2} = \{\Delta^e\}^T\left(-\frac{II_z}{A_{12}^e}\int_0^{\beta_p}\int_{r_{i_p}}^{r_{o_p}}\{\bar{\varepsilon}^e\}^T\{h_{31}\}\,r\,dr\,d\theta\right)Q_3^e \tag{3.61}$$

$$U_{p_3} = \frac{1}{2}\left(\frac{h_p\varepsilon\varepsilon_{33}^T}{A_{12}^e}\right)(Q_3^e)^2 \tag{3.62}$$

where I_z and II_z are obtained from integrating the potential energy with respect to the z axis and considering the piezoceramic patch to be on top of the brake disc

$$I_z = \frac{1}{12}h_p\left(4\,h_p^2 + 6\,h_p\,h_{pl} + 3\,h_{pl}^2\right)$$
$$II_z = \frac{1}{2}h_p\left(h_p + h_{pl}\right) \tag{3.63}$$

and A_{12}^{e} is the surface area of a single element of the piezoceramic patch

$$A_{12}^{e} = \int_{0}^{\beta_p} \int_{r_{i_p}}^{r_{o_p}} r \, dr \, d\theta \tag{3.64}$$

The virtual work δW_{shunt} associated with the shunted network is given by

$$\delta W^{e} = -\left(L^{e} \ddot{Q}^{e} + R^{e} \dot{Q}^{e} + \frac{1}{C^{e}} \, Q^{e} \right) \delta Q^{e} \tag{3.65}$$

Now, the equations governing the dynamics of the shunted piezoceramic network can be extracted using the Lagrangian dynamics as

$$\begin{gathered} \frac{d}{dt}\left[\frac{\partial \mathcal{L}}{\partial\{\dot{\Delta}^{e}\}}\right] - \left[\frac{\partial \mathcal{L}}{\partial\{\Delta^{e}\}}\right] = \{f^{e}\} \\ \frac{d}{dt}\left[\frac{\partial \mathcal{L}}{\partial\{\dot{\mathrm{Q}}^{e}\}}\right] - \left[\frac{\partial \mathcal{L}}{\partial\{\mathrm{Q}^{e}\}}\right] = -\left(L^{e} \ddot{Q}^{e} + R^{e} \dot{Q}^{e} + \frac{1}{C^{e}} \, Q^{e} \right) \end{gathered} \tag{3.66}$$

Utilizing the Lagrangian dynamics result in the following element matrix form

$$\begin{gathered} \begin{bmatrix} [M_p^e] & \{0\} \\ \{0\} & L^e \end{bmatrix} \begin{Bmatrix} \{\ddot{\Delta}^e\} \\ \ddot{Q}^e \end{Bmatrix} + \begin{bmatrix} [0] & \{0\} \\ \{0\} & R^e \end{bmatrix} \begin{Bmatrix} \{\dot{\Delta}^e\} \\ \dot{Q}^e \end{Bmatrix} \\ + \begin{bmatrix} [K_p^e] & \{K_c^e\} \\ \{K_c^e\}^T & \left(\frac{1}{C^{s^e}} + \frac{1}{C^e}\right) \end{bmatrix} \begin{Bmatrix} \{\Delta^e\} \\ Q^e \end{Bmatrix} = \begin{Bmatrix} \{f^e\} \\ 0 \end{Bmatrix} \end{gathered} \tag{3.67}$$

where

$$[M_p^e] = \rho_p \, h_p \int_{0}^{\beta_p} \int_{r_{i_p}}^{r_{o_p}} \{N\}^T \{N\} \, r \, dr \, d\theta$$

$$\left[K_p^e\right] = I_z \int_0^{\beta_p} \int_{r_{i_p}}^{r_{o_p}} \{\bar{\varepsilon}^e\}^T \left[c^D\right] \{\bar{\varepsilon}^e\}\, r\, dr\, d\theta$$

$$\{K_c^e\} = -\frac{II_z}{A_{12}^e} \int_0^{\beta_p} \int_{r_{i_p}}^{r_{o_p}} \{\bar{\varepsilon}^e\}^T \{h_{31}\}\, r\, dr\, d\theta$$

$$\frac{1}{C^{s^e}} = \left(\frac{h_p \varepsilon \varepsilon_{33}^T}{A_{12}^e}\right)$$

The global equations of motion of the shunted piezoceramic network can then be determined by assembling the element matrices as

$$\begin{bmatrix} [M_p] & [0] \\ [0] & [L^e] \end{bmatrix} \begin{Bmatrix} \{\ddot{\Delta}\} \\ \{\ddot{Q}\} \end{Bmatrix} + \begin{bmatrix} [0] & [0] \\ [0] & [R^e] \end{bmatrix} \begin{Bmatrix} \{\dot{\Delta}\} \\ \{\dot{Q}\} \end{Bmatrix} + \begin{bmatrix} [K_p] & [K_c] \\ [K_c]^T & \left[\frac{1}{C^s} + \frac{1}{C}\right] \end{bmatrix} \begin{Bmatrix} \{\Delta\} \\ \{Q\} \end{Bmatrix} = \begin{Bmatrix} \{F\} \\ \{0\} \end{Bmatrix} \tag{3.68}$$

Integrating the shunted piezoceramic network with the disc brake system derived in Chapter 2 result in the following matrix form

$$[M^T]\{\ddot{X}\} + [C^T]\{\dot{X}\} + [K^T]\{X\} = \{F\} \tag{3.69}$$

where $[M^T]$, $[C^T]$, and $[K^T]$ are the global mass, damping, and stiffness matrices of the integrated shunted piezoceramic network with the disc brake system. Also, $\{X\}$ and $\{F\}$ denote the structural and electrical degrees of freedom as well as load vectors applied to the assembly.

The total system matrices are expressed as

$$[M^T] = \begin{bmatrix} ([M_{pl}] + [M_p]) & [0] \\ [0] & [L^e] \end{bmatrix}$$

$$[C^T] = \begin{bmatrix} [G_{pl}] & [0] \\ [0] & [R^e] \end{bmatrix}$$

$$[K^T] = \begin{bmatrix} ([K_{pl}] + [A] + [B] - [R] + [K_p]) & [K_c] \\ [K_c]^T & \left[\frac{1}{C^s} + \frac{1}{C}\right] \end{bmatrix}$$

Note that bonding the shunted piezoceramic patch to the disc brake system has resulted in adding damping as quantified by the damping matrix $[C^T]$. It has also modified the stiffness and mass matrices of the assembly. The final step is to apply the boundary conditions on the structure to eliminate the rigid body modes and then the remaining system is expressed as

$$[M_o]\{\ddot{X}\} + [C_o]\{\dot{X}\} + [K_o]\{X\} = \{F_o\} \tag{3.70}$$

3.4.4 Piezoceramic Sensors and Energy Harvesting

Piezoceramic patch bonded to a vibrating disc can be used to monitor its vibration and generate charge. This section will discuss the work of piezoceramics as sensors and energy harvesters.

Equation (3.56) describes the relation between mechanical stresses and strains and between electric field and electric displacement in 3 direction. Eliminating the stresses and applying short-circuit conditions $\mathbb{E}_3 = 0$ yields

$$h_{31}\{(s_{11}^{\mathbb{E}} + s_{12}^{\mathbb{E}})\, D_3 - d_{31}\,(S_1 + S_2)\} = 0 \tag{3.71}$$

Or

$$D_3 = \bar{e}_{31}(S_1 + S_2) = -z\,\bar{e}_{31}\left[\frac{\partial^2 w_0}{\partial r^2} + \frac{1}{r}\frac{\partial w_0}{\partial r} + \frac{1}{r^2}\frac{\partial^2 w_0}{\partial \theta^2}\right]$$

where $\bar{e}_{31}$is the piezoceramic stress constant

$$\bar{e}_{31} = \frac{d_{31}}{(s_{11}^{\mathbb{E}} + s_{12}^{\mathbb{E}})}$$

Since the piezoceramic patch will be bonded on the top surface of the brake disc

$$z^{top} = \frac{h_{plate}}{2}$$

and therefore

$$D_3 = -\left(\frac{h_{pl}}{2}\right)\bar{e}_{31}\left[\frac{\partial^2 w_0}{\partial r^2} + \frac{1}{r}\frac{\partial w_0}{\partial r} + \frac{1}{r^2}\frac{\partial^2 w_0}{\partial \theta^2}\right] \tag{3.72}$$

Discretizing equation (3.72) yields the element electric displacement

$$D_3^e = -\left(\frac{h_{pl}}{2}\right)\bar{e}_{31}\left[\frac{\partial^2 \{N\}}{\partial r^2} + \frac{1}{r}\frac{\partial \{N\}}{\partial r} + \frac{1}{r^2}\frac{\partial^2 \{N\}}{\partial \theta^2}\right]\{\Delta^e\} \tag{3.73}$$

Once the element electric displacement is determined, the total electric charge is calculated as

$$Q_3^e = \int_0^{\beta_p}\int_{r_{i_p}}^{r_{o_p}} D_3^e\; r\, dr\, d\theta$$

and the element generated electrical voltage is calculated as

$$V_3^e = \frac{Q_3^e}{C^{T^e}}$$

where C^{T^e} is the capacitance of a single element and is given as

$$C^{T^e} = \frac{\varepsilon_{33}^T}{t_{p_3}} A_{12}^e = \frac{\varepsilon_{33}^T}{t_{p_3}} \int_0^{\beta_p} \int_{r_{i_p}}^{r_{o_p}} r \, dr \, d\theta$$

The element voltage is then assembled to calculate the total voltage of the piezoceramic patch and the generated power is determined using

$$P = \frac{V^2}{R} \tag{3.74}$$

where *R* is the shunt resistor.

3.5 Numerical Analysis

The effect of integrating shunted piezoceramic network with disc brake systems is investigated in this section using two different models discussed in section 3.4.

3.5.1 Analysis I

The shunted system equations of motion were developed in section 3.4.1. The parameters used in this analysis are summarized in Table 3.2.

Table 3.2: System parameters

Parameter	Symbol	Value
Mass	m	1 kg
Stiffness of spring 1	k_1	1.5 N/m
Stiffness of spring 2	k_2	1 N/m
Stiffness of spring 3	k_3	1 N/m
Angle 1	α_1	30^o
Angle 2	α_2	150^o
Shunt parameter	τ	1000 s
Electromechanical coupling coefficient	k_{33}^2	0.5

Figures 3.8 and 3.9 illustrate the stability of the system with the corresponding mode-coupling frequency behavior. The critical value of the coefficient of friction μ_{cr} for the conventional system is 0.288 which is a typical value for squeal whereas in the shunted system $\mu_{cr} = 1.15$. This example demonstrates the effectiveness of shunted piezoceramic networks in suppressing squeal and flutter instability.

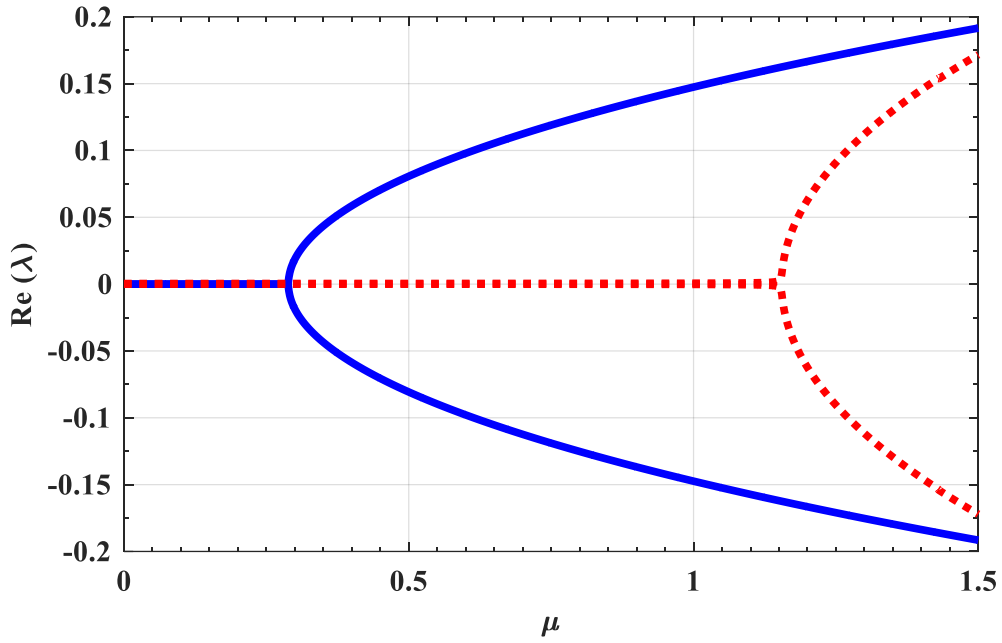

Figure 3.8: Stability of minimal model modes; (–) conventional system (. . .) tuned system with resistive shunt

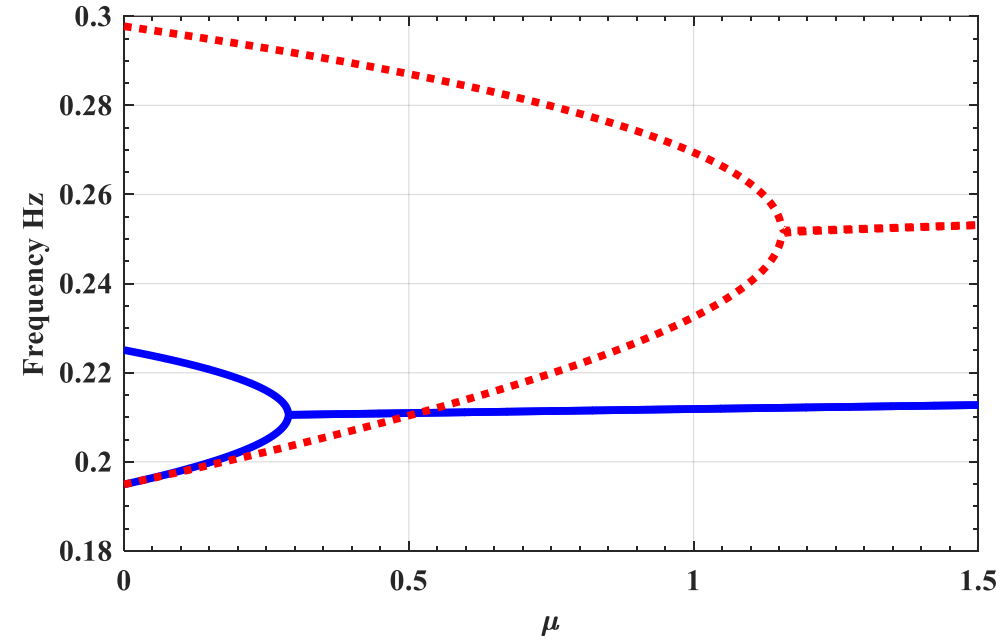

Figure 3.9: Frequency plot of minimal model modes; (–) conventional system (. . .) tuned system with resistive shunt

3.5.2 Analysis II

In this analysis the *FEM* developed in section 3.4.2 is considered. System parameters are given in Table 3.3 and the mesh details are summarized in Table 2.4.

Table 3.3: Nominal values of system parameters

Parameter	Symbol	Value
Outer radius of the disc	r_o	150 mm
Inner radius of the disc	r_i	40 mm
Outer radius of contact area	r_{c_o}	142 mm
Inner radius of contact area	r_{c_i}	100 mm
Thickness of the disc	h	26 mm
Contact angle	θ_c	60^o
Young's modulus	E	88.9 GPa
Density	ρ	7150 kg/m^3
Poisson's ratio	ν	0.285
Nominal contact stiffness	k_{nom}	0.35 x 10^{11} N/m^3
Shunt parameter	τ	4.7853 x 10^{-5} s
Electromechanical coupling coefficient	k_{33}^2	0.56

The shunted network used in this analysis is designed based on mode 4 frequency. The mode-coupling frequency (squeal frequency) was obtained in section 2.5.1.2 to be 4444.4 Hz for mode 4. Therefore, to target this frequency, equation (3.48) was used which results in tuning parameter $\tau = 4.7853 \text{ x } 10^{-5}$ s.

The effect of the shunted network on the system stability can be seen in Figures 3.10 and 3.12. The critical values of the coefficient of friction μ_{cr} for mode 4 without tuning is 0.33 and for mode 5 is 0.36 which are typical values for squealing. The improved critical values of coefficient of friction for modes 4 and 5 are 1.28 and 0.94, respectively.

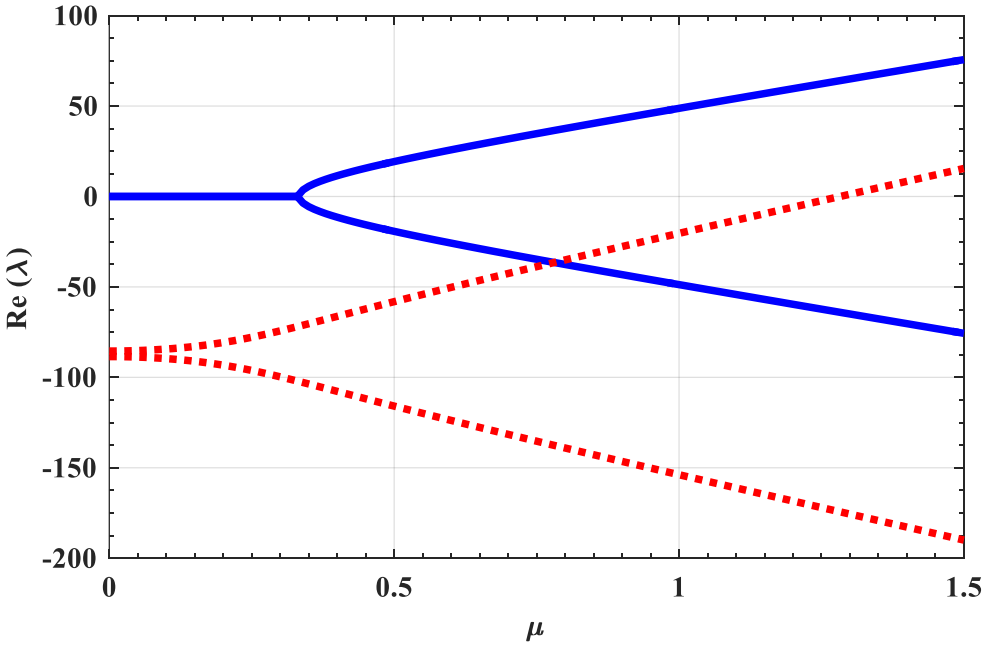

Figure 3.10: Stability of transverse doublet mode 4; (–) conventional system (. . .) tuned system with resistive shunt

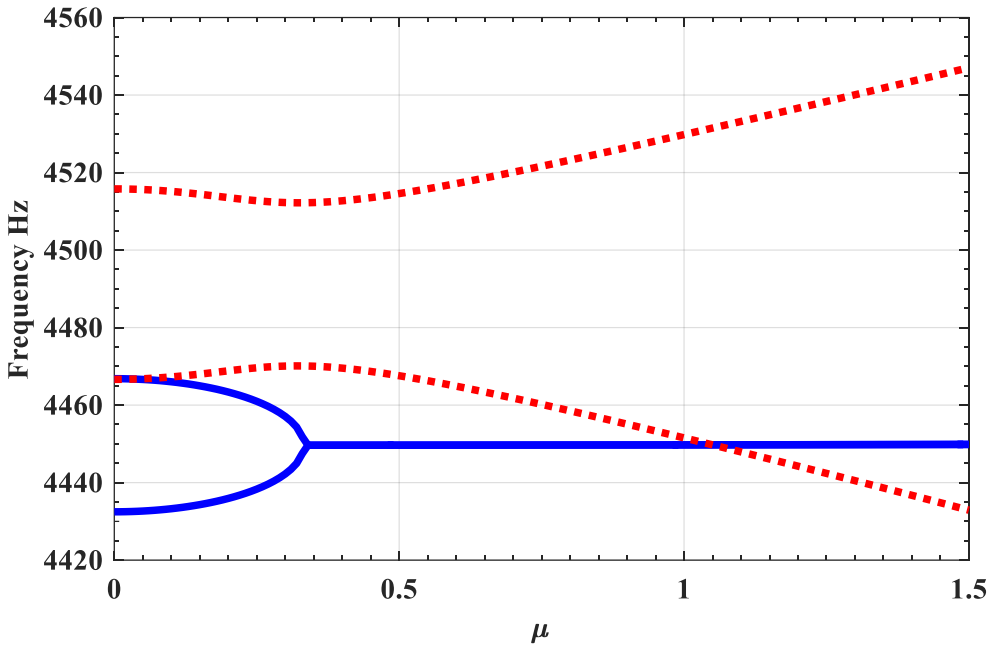

Figure 3.11: Frequency plot of mode 4; (–) conventional system (. . .) tuned system with resistive shunt

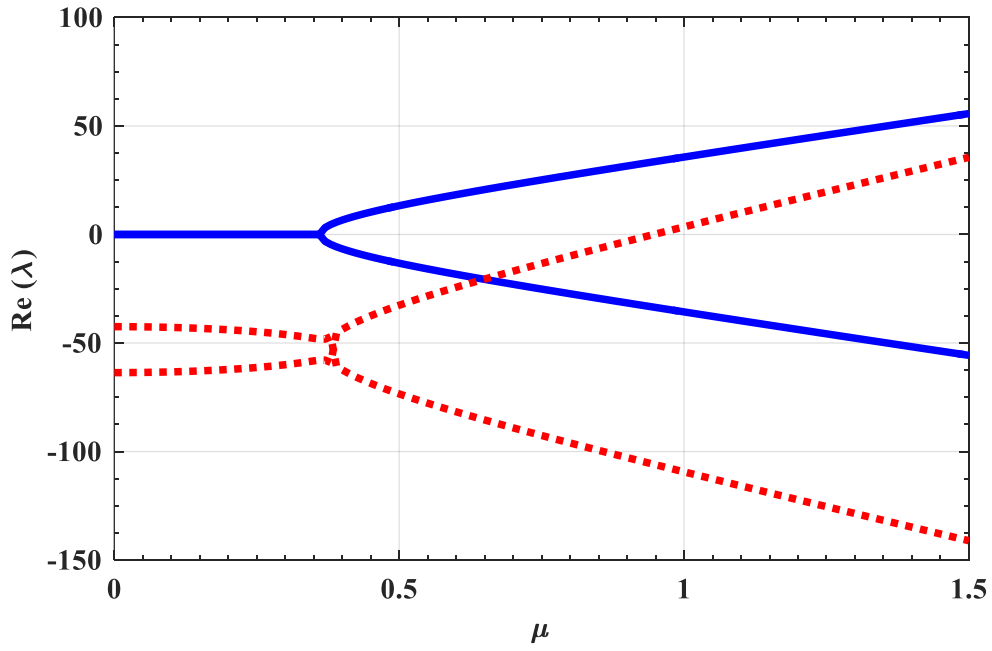

Figure 3.12: Stability of transverse doublet mode 5; (–) conventional system (. . .) tuned system with resistive shunt

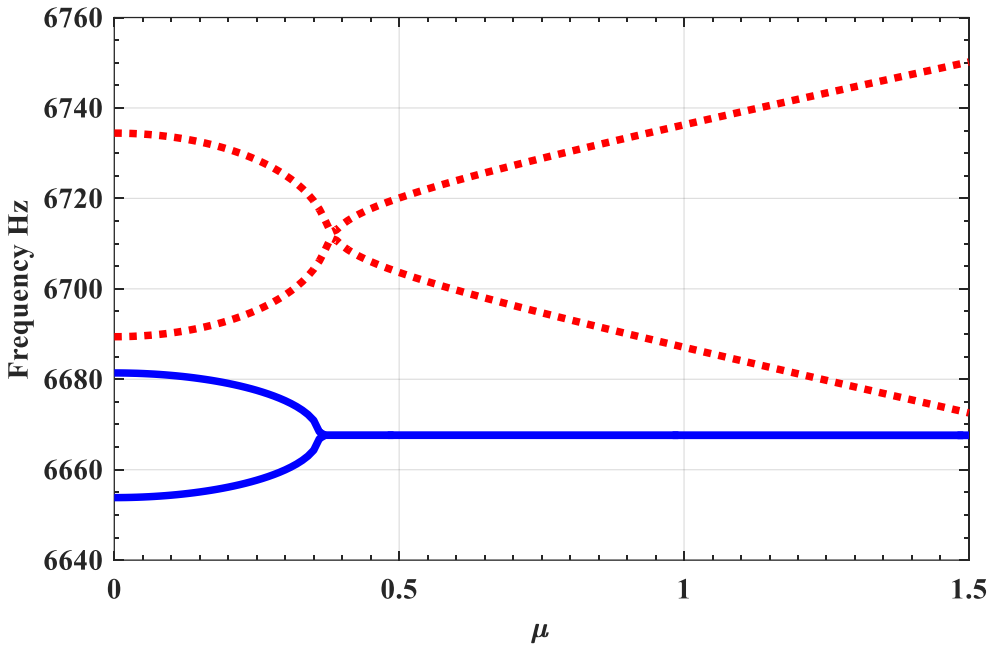

Figure 3.13: Frequency plot of mode 5; (–) conventional system (. . .) tuned system with resistive shunt

3.6 Design of Disc Brake System Prototype with Integrated Piezoceramic Patch

This section aims at integrating piezoceramic patch with the new disc brake system prototype discussed in Chapter 2 in order to establish practical comparison between conventional disc brake systems and the proposed design of disc brake system that is shunted with piezoceramics. *FEM* formulation discussed in 3.4.3 are used to analyze the new proposed design. The section includes modal analysis of the new disc brake system prototype with shunted piezoceramic patch using both FEM and *ANSYS*® Workbench.

3.6.1 Design of Stationary Brake Disc with Integrated Piezoceramic Patch

Piezoceramic sheet is used in this study to generate electrical energy and increase the stability of disc brake systems. These sheets are available in the market with specific dimensions and are very brittle which makes them hard to shape in laboratories. The reason to reshape the piezoceramic patch is to accommodate the shape of annular sectors in the finite element mesh as shown in Figure 2.8. The piezoceramic patch used in the new prototype is made out of PZT-5A and the properties and dimensions are summarized in Table 3.4.

The piezoceramic patch is subjected to short and open circuit electrical boundary conditions. The natural frequencies of the brake disc with the attached piezoceramic patch subject to different boundary conditions are presented in Table 3.5 using developed *FEM* and also compared against numerical solution of *ANSYS*® Workbench. Figures 3.14 and 3.15 show the frequency response of the system when subjected to a harmonic unit force at the outer edge under short and open circuit boundary conditions, respectively.

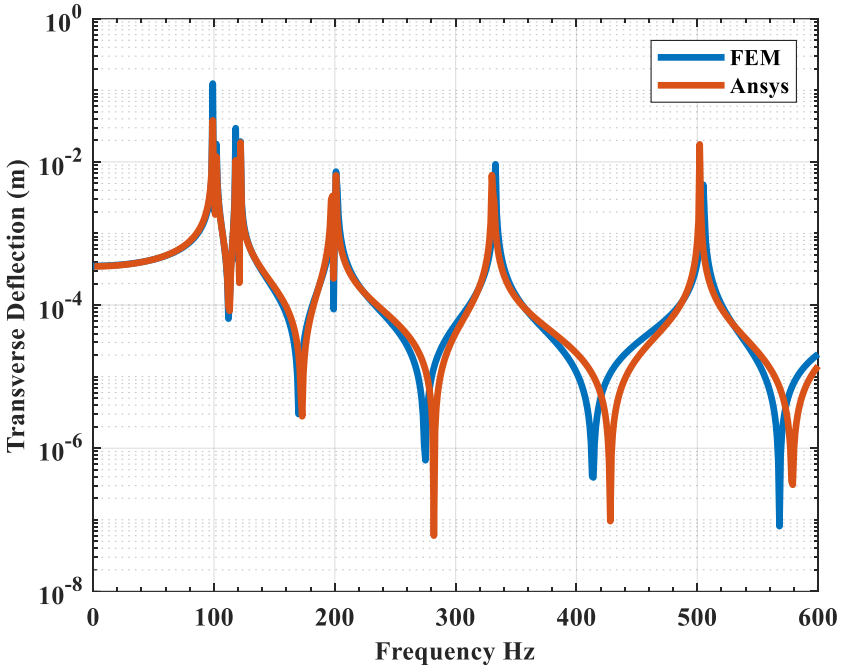

Figure 3.14: Collocated frequency response of brake disc prototype with integrated piezoceramic patch (short circuited)

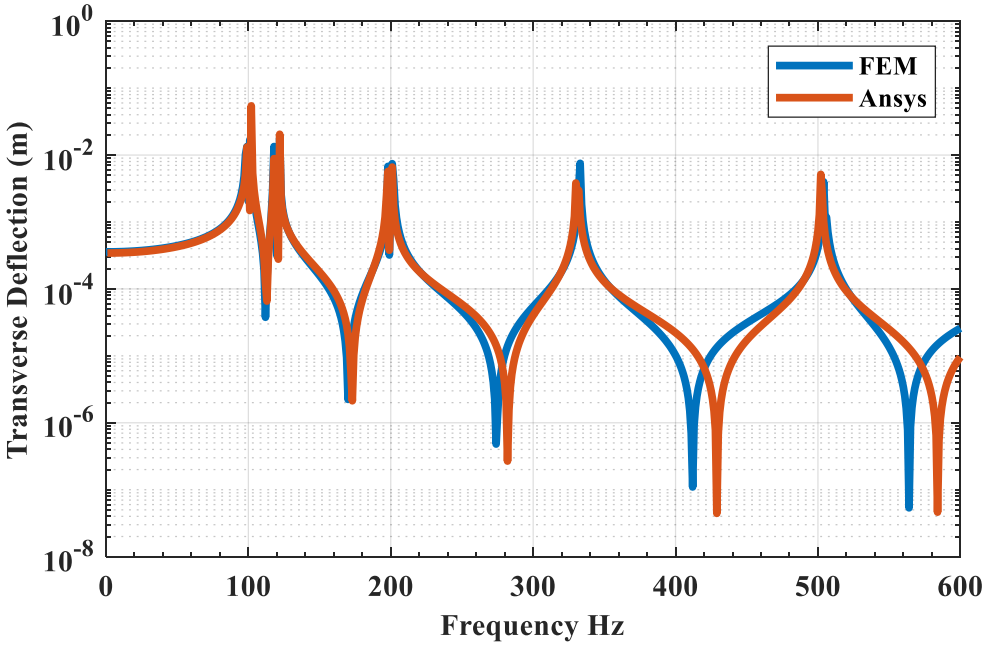

Figure 3.15: Collocated frequency response of brake disc prototype with integrated piezoceramic patch (open circuit)

Table 3.4: Piezoceramic patch properties and dimensions [65]

Parameter	Symbol	Value
Outer radius of the patch	r_{p_o}	100 mm
Inner radius of the patch	r_{p_i}	50 mm
Patch contact angle	θ_p	30^0
Thickness of the patch	h_p	0.2667 mm
Elastic compliance in 1-1 direction	$s_{11}^{\mathbb{E}}$	16.4 (pm^2/N)
Elastic compliance in 1-2 direction	$s_{12}^{\mathbb{E}}$	-5.74 (pm^2/N)
Elastic compliance in 1-3 direction	$s_{13}^{\mathbb{E}}$	-7.22 (pm^2/N)
Elastic compliance in 3-3 direction	$s_{33}^{\mathbb{E}}$	18.8 (pm^2/N)
Elastic compliance in 5-5 direction	$s_{55}^{\mathbb{E}}$	47.5 (pm^2/N)
Elastic compliance in 6-6 direction	$s_{66}^{\mathbb{E}}$	44.3 (pm^2/N)
Piezoelectric coefficient in 3-1	d_{31}	-171 (pm/V)
Piezoelectric coefficient in 3-3	d_{33}	374 (pm/V)
Piezoelectric coefficient in 1-5	d_{15}	584 (pm/V)
Electric permittivity in 1-1	ε_{11}^{T}	15,317 (pF/m)
Electric permittivity in 3-3	ε_{33}^{T}	15,051 (pF/m)
Density	ρ_p	7750 kg/m^3

Table 3.5: Natural Frequencies of brake disc prototype with integrated piezoceramic patch subject to different electrical BC and clamped-free mechanical BC

	Natural Frequency $f\ (Hz)$			
Doublet Modes	Short Circuit		Open Circuit	
n	*ANSYS*®	*FEM*	*ANSYS*®	*FEM*
1	99.18	99.03	99.482	98.66
	100.27	99.73	100.28	99.72
2	118.3	117.92	118.36	117.83
	121.93	121.89	121.94	121.88
3	197.6	198.31	197.75	198.11
	200.73	201.35	200.73	201.35
4	329.91	332.07	330.28	331.58
	331.36	332.74	331.4	332.68
5	502.08	504.64	502.33	504.45
	502.45	505.88	502.99	505.04

This section serves as a model verification where the developed *FEM* is compared against another numerical software *ANSYS*® Workbench. The comparison shows good agreement and therefore both numerical results can be used in comparison with experimental results in Chapter 4.

3.7 Summary

This chapter introduced the theory governing the shunted piezoelectric networks in order to demonstrate their merit and significance in enhancing the stability of disc brake systems. It has been concluded from section 3.4.3 that the effect of attaching piezoceramic springs with resistive shunt enhance the stability of the flutter modes. The chapter has also presented the finite element formulation of disc brake systems with integrated piezoceramic patch in which the developed charge of a vibrating system can be collected and harvested. A new disc brake system prototype was introduced and its modal analysis was performed using *FEM* and *ANSYS*® Workbench.

Chapter 4: Experimental Results

4.1 Overview

This chapter presents the different experiments carried out for the disc brake system prototype discussed in Chapter 2 in the conventional case and the newly proposed disc brake system with integrated shunted piezoceramic networks covered in Chapter 3. The experimental work attempts to validate the theoretical predictions of chapters two and three. The laboratory experimental setup along with a detailed description is provided. Also, the experimental dynamic characteristics of the disc brake system are compared with those obtained previously from the finite element modeling described in chapters two and three in three different tests.

4.2 Experimental Set-up

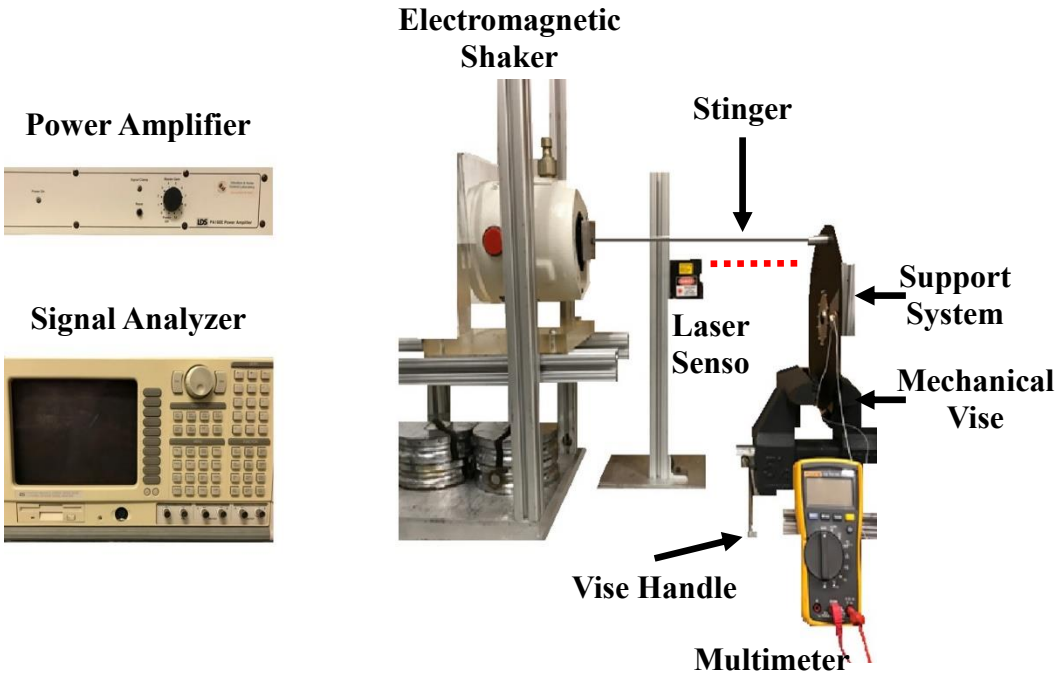

Figure 4.1: Disc brake system experimental setup

The experimental arrangement construction along with equipment used are described in this section. Using a laboratory scale model, the experimental setup of the proposed concept of disc brake system is displayed in Figure 4.1. The brake disc shown in Figure 4.2 is made out of aluminum and is connected to a hub which is attached to the support system.

Figure 4.2: Brake disc prototype

Figure 4.3 shows 3D printed brake pads which are attached to a vise in the experimental setup. The vise controls the distance between the brake disc and the contact pads. The newly proposed disc brake system with integrated piezoceramic patch is shown in Figure 4.4.

The brake disc used in this experiment is fixed to the support system at the inner raduis and is excited using an electromagnetic shaker connected via a stainless

steel stinger. The electromagnetic shaker is connected to a power amplifier and their specifications are listed in Tables 4.1 and 4.2, respectively.

A displacement laser sensor, LM 200 (ANL2535REC) is installed against the brake disc about 5 mm away and is connected to a dynamic signal analyzer, Stanford Research System (Model SR780) where the experimental data are acquired.

The acceleration input of the electromagnetic shaker is measured using shear accelerometer, (PCB Piezotronics 352C68) at different excitation frequencies and the accelerometer specifications are presented in Table 4.3.

A laser vibrometer, (VibraScan Polytec OFV 055) is used to capture the modes of vibration of the system. Such a device is of high importance since the modes of vibration are extremely hard to distinguish visually.

Figure 4.3: 3D printed brake pads

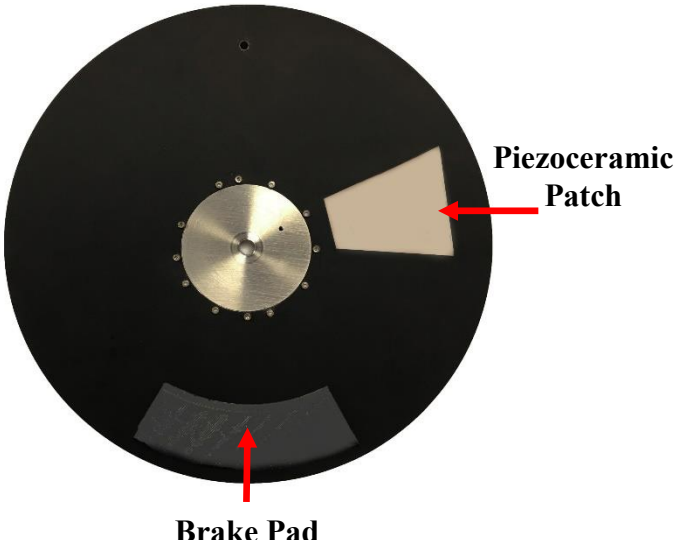

Figure 4.4: Newly proposed disc brake system

Table 4.1: Electromagnetic shaker specifications (V408 – LDS Test and Measurement LLC, Middleton, WI)

Shaker Properties	Value	
System sine force peak (naturally cooled)	98	N
System sine force peak (forced cooling)	196	N
Shaker max random force rms	89	N
Max acceleration sine peak	100	g
System velocity sine peak	1.78	m/s
System continuous displacement (pk-pk)	17.6	mm
Moving element mass	0.2	kg
Usable frequency rang	5-9,000	Hz

Table 4.2: Shaker power amplifier specifications, (PA100E – LDS Test and Measurement LLC, Middleton, WI)

Power Amplifier Properties	Value	
Rated sinusoidal power output matched	147	W
Resistive load	2.9	Ω
Max. continuons sinusoidal VA output, 0.5pf	147	VA
Frequency range at rated power	10 Hz–10 kHz	
Total harmonic distortion at rated output 20Hz-10kHz	Type 0.5	%
Max. output voltage	20	Vrms
Max. no load voltage	32	Vrms
Voltage regulations	3	%
Output current at rated VA	7A	rms
Random output	14 A	pk
Over-current trip level	10A	rms
Input sensitivity for max output (4kHz)	1 V	rms
Signal to noise ratio	>75	dB
Amplifier efficiency	58	%

Table 4.3: Accelerometer specifications, (PCB Piezotronics 352C68)

Shear Accelerometer specifications	Value	
Voltage sensitivity	94.1	mV/g
Frequency range	0.5-10,000	Hz
Output bias level	10.8	V

4.3 Experimental Tests

This section covers the performance of different experimental tests in order to demonstrate the merit of the work discussed in this dissertation. Both the conventional and the newly proposed prototypes are tested under different conditions.

4.3.1 Test 1: Stationary Brake Disc

The dynamic characteristics of the stationary brake disc are measured in the frequency domain by subjecting the brake disc to swept sine wave excitation. The natural frequencies of the brake disc are presented in Table 4.4 and the non-collocated frequency response is shown in Figure 4.5.

Table 4.4: Natural frequencies of the transverse doublet modes of the brake disc prototype

	Natural Frequency $f\ (Hz)$				
n	Experiment	*ANSYS*®	Difference %	*FEM*	Difference %
1	96	100.74	4.94	100.10	4.28
2	118	111.53	5.48	110.84	6.07
3	169	174.13	3.04	173.62	2.73
4	288	291.7	1.28	291.68	1.28

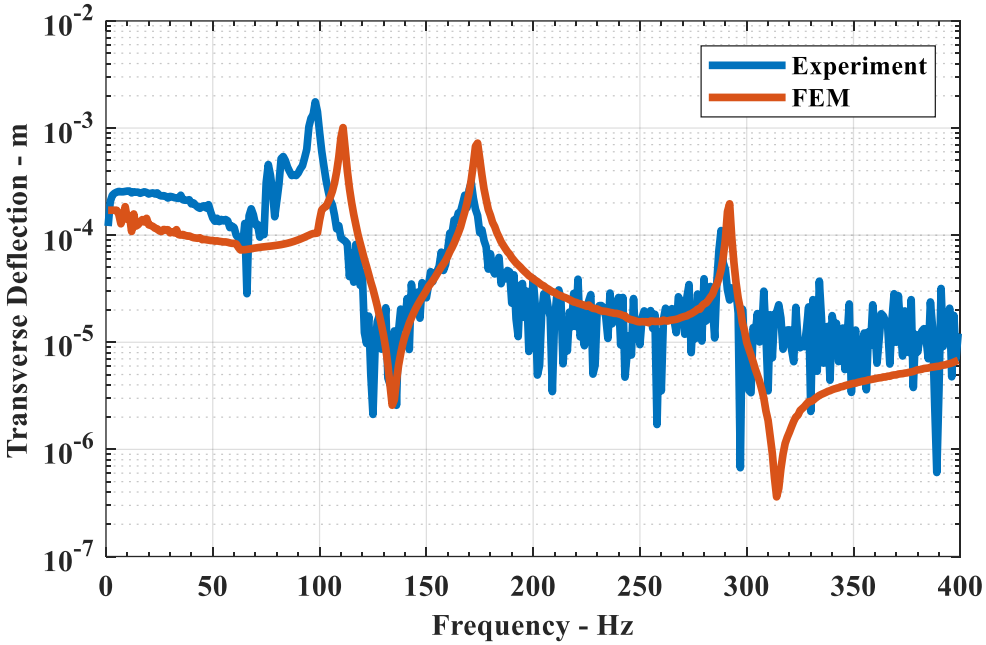

Figure 4.5: Non-collocated frequency response of the brake disc prototype

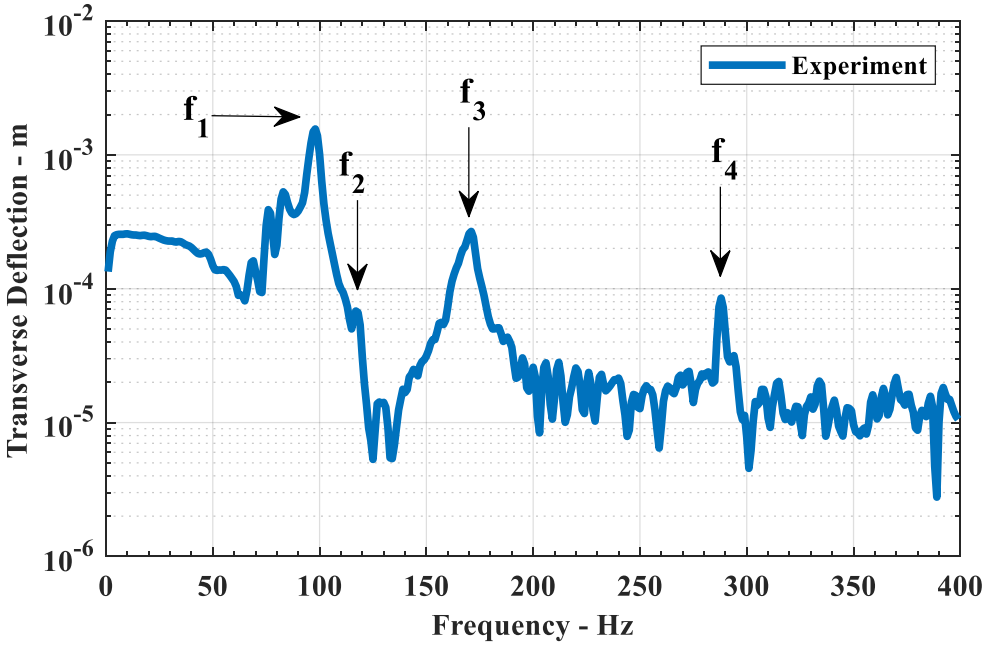

Figure 4.6 : Experimental frequency response of the brake disc prototype

It is obvious from Table 4.4 and Figure 4.5 that the predictions of the *FEM* are in good agreement with the experimental results at resonant frequencies. However, doublet mode n = 2 is hard to identify experimentally as shown in Figure 4.6 because the laser sensor is placed on the nodal line. The use of *FEM* allows to obtain the second doublet mode as was shown in Figure 2.17 but its deflection reduces significantly when damping is added to the system.

4.3.2 Test 2: Stationary Disc Brake System

This section examines the effect of attaching the contact pads to the brake disc. The brake pads shown in Figure 4.3 are manufactured from ABS plastic and have two different surfaces. One face has a smooth surface and the other has a rough surface. The vibrating disc is pressed by the brake pads via a vise and the contact takes place on the smooth face. The goal here is to make coefficient of friction between the disc and the pads to be as small as possible to obtain the highest separation in frequencies as discussed earlier in Chapter 2. The vise and the connected pads are pressed slowly until complete contact with the stationary disc. After that, the electromechanical shaker is turned on and the system is subjected to swept sine wave excitation. Figure 4.7 and Figure 4.8 show the non-collocated frequency response of the disc brake system with excitation frequencies division of 1 Hz and 0.25 Hz, respectively.

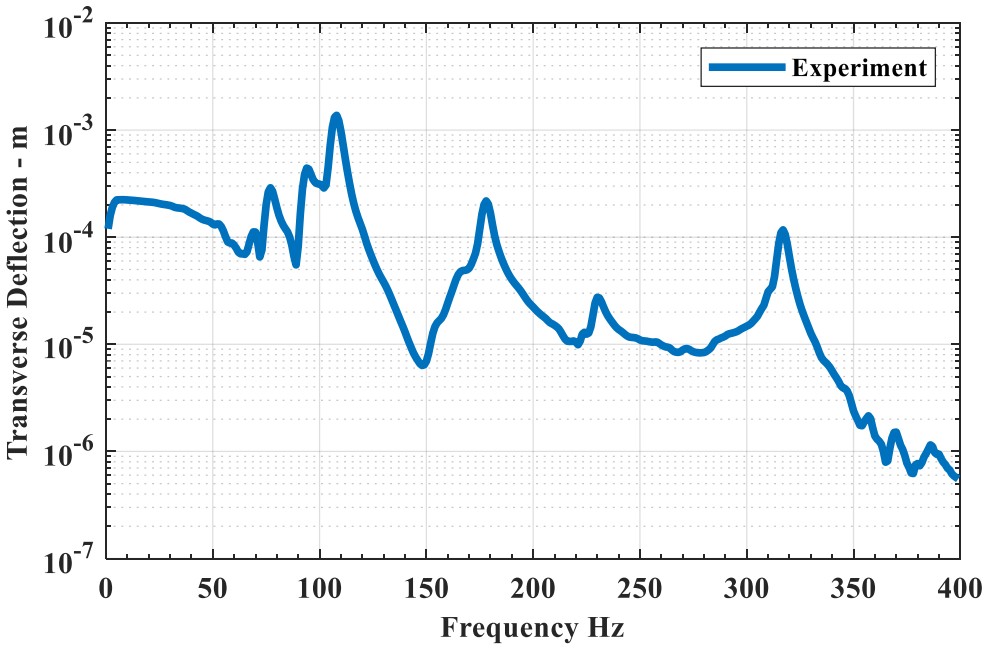

Figure 4.7: Non-collocated frequency response of disc brake system prototype with contact pads using 1 Hz division

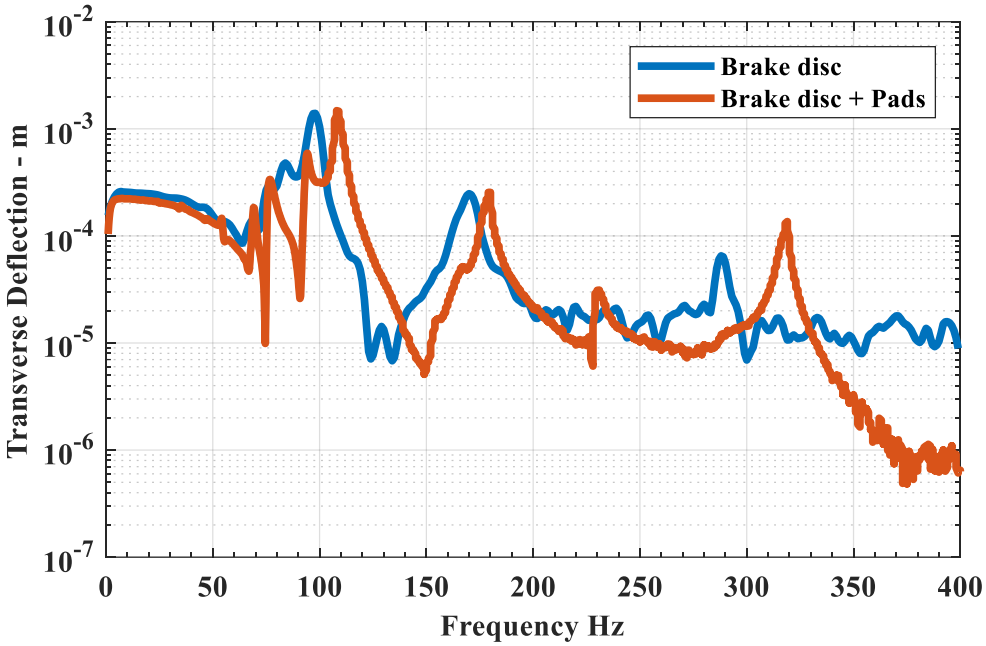

Figure 4.8: Non-collocated frequency response of disc brake system prototype with contact pads using 0.25 Hz division

The disc brake system exhibits frequency separation at mode 3 as was predicted by the *FEM* in section 2.6.2 however, that split requires a very high number of divisions to obtain. It should also be mentioned that the experimental runs took place under different pre-stress conditions and that the effect of the prestress was negligible.

Figure 4.9 shows frequency separation of transverse doublet mode 3 using 0.25 Hz division. The mode frequency was found to be 169 Hz before contact as mentioned in Table 4.4 and the effect of contact splits the frequency to 167 Hz and 181 Hz. The difference is 14 Hz which is higher than what the model predicted in Chapter 2. This is one of the limitations of the model, which ignores the thickness of the pads and the material density.

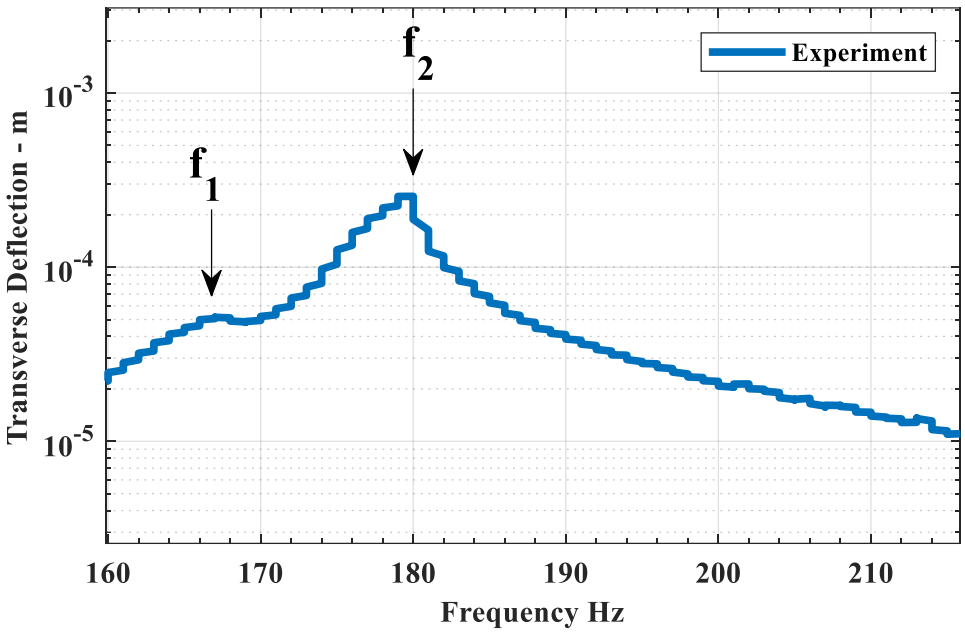

Figure 4.9: Frequency separation of transverse doublet mode 3 of disc brake system prototype with contact pads using 0.25 Hz division

4.3.3 Test 3: Stationary Disc Brake System with Integrated Piezoceramic Patch

The performance of the new disc brake system with integrated piezoceramic patch is studied and analyzed in this section. The new proposed disc brake system prototype is shown in Figure 4.10.

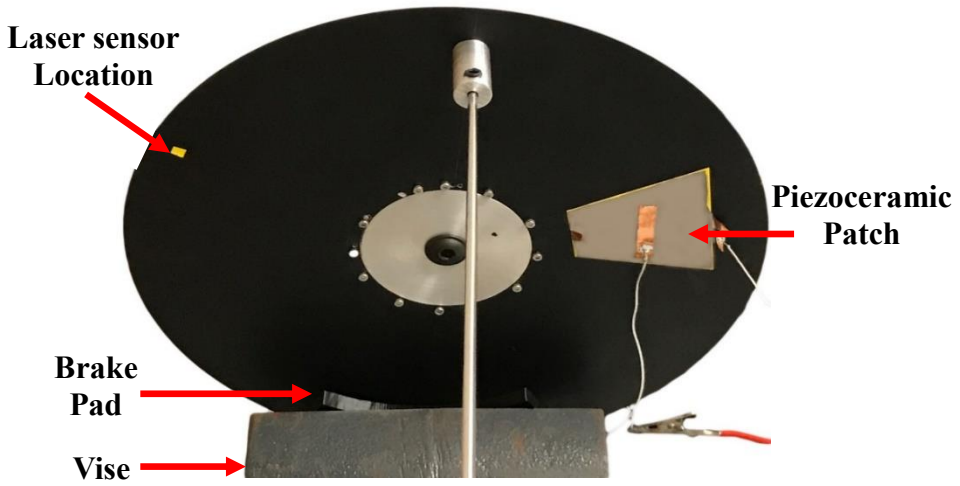

Figure 4.10: Newly proposed disc brake system in test 3

An isolating layer is first glued to the surface of the brake disc and the piezoceramic patch is then bonded to prevent the patch from undergoing short circuit. The resonant frequencies of the transverse doublet modes are presented in Table 4.5 and the non-collocated frequency response of the brake disc is shown in Figure 4.11.

The numerical results appear to be in good agreement with the experimental results apart from the shift of the first resonant frequency. This may be due to the effect of bonding and the added layer which has not been considered in the developed *FEM*.

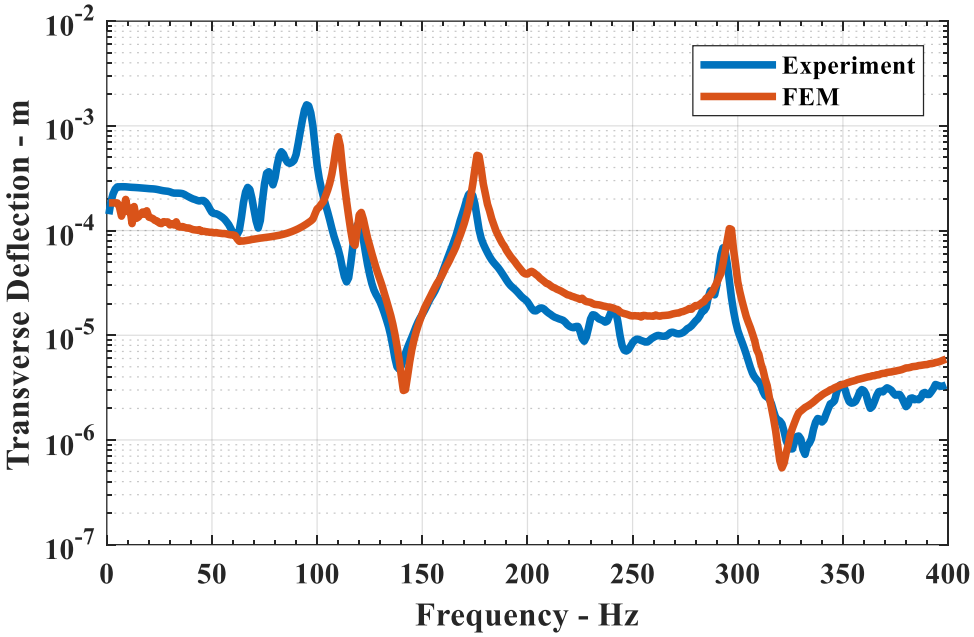

Figure 4.11: Non-collocated frequency response of the brake disc with integrated piezoceramic patch

Table 4.5: Natural Frequencies of transverse doublet modes of the brake disc with integrated piezoceramic patch under short circuit electrical boundary condition

	Natural Frequency $f\ (Hz)$		
Doublet Modes	Short Circuit Boundary Condition		
n	Experiment	*ANSYS*®	*FEM*
1	96	99.262	99.05
		101.19	100.90
2	120	110.47	110.21
		120.58	120.25
3	173	176.45	176.49
		199.99	200.85
4	293	294.92	296.48
		330.03	332.08

Each transverse doublet mode has two natural frequencies which are challengeable to measure experimentally due to . It should also be noted that stinger modes are present in the range of 50 Hz to 90 Hz as shown in Figure 4.11. Figure 4.12 shows the different transverse doublet modes obtained graphically from *ANSYS*® Workbench**.**

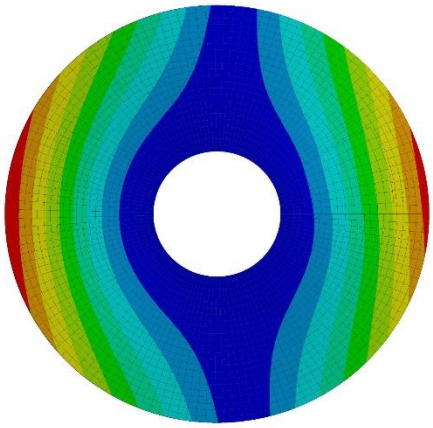

$$\boldsymbol{f = 99.262\ Hz}$$

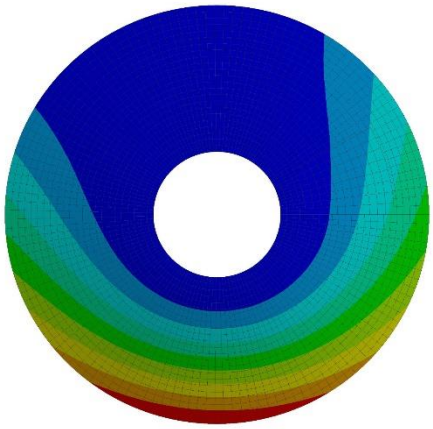

$$\boldsymbol{f = 101.19\ Hz}$$

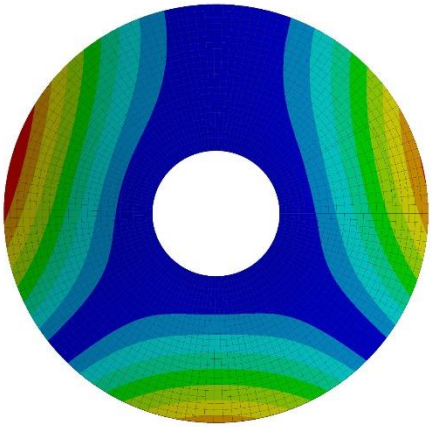

$$f = 110.47\ Hz$$

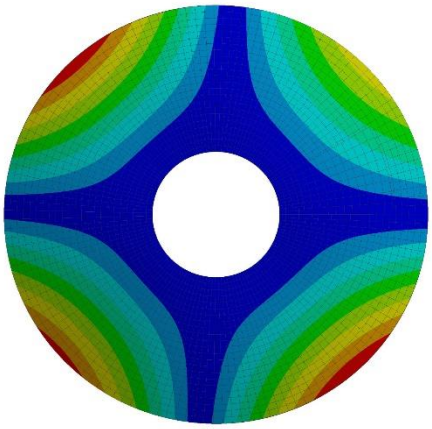

$$f = 120.58\ Hz$$

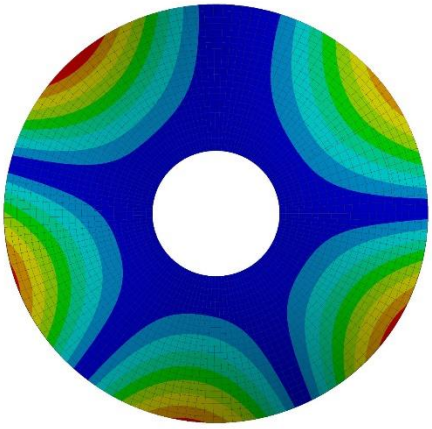

$$f = 176.45\ Hz$$

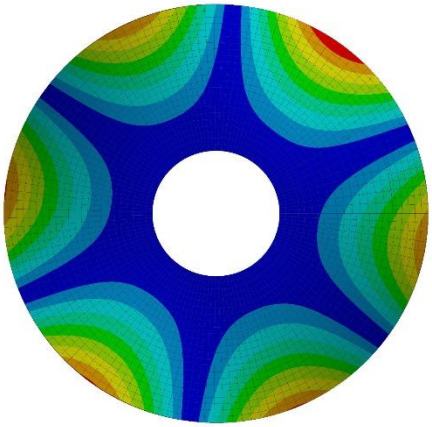

$$f = 199.99\ Hz$$

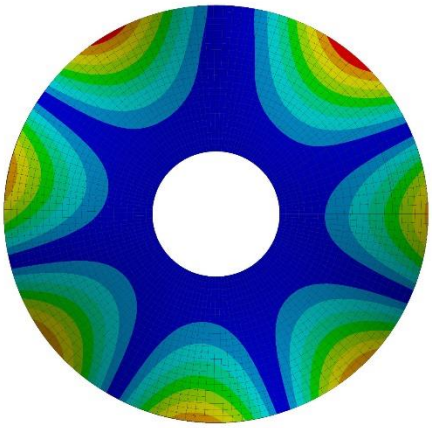

$$f = 294.92\ Hz$$

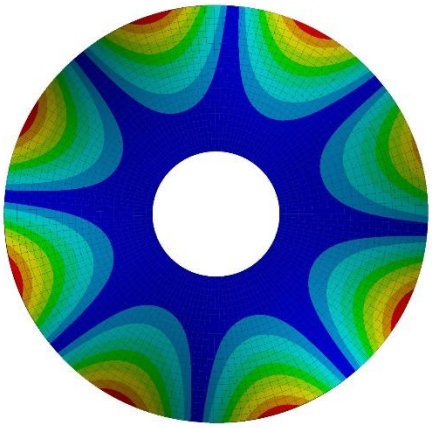

$$f = 330.03\ Hz$$

Figure 4.12: Transverse doublet mode shapes using *ANSYS*® Workbench

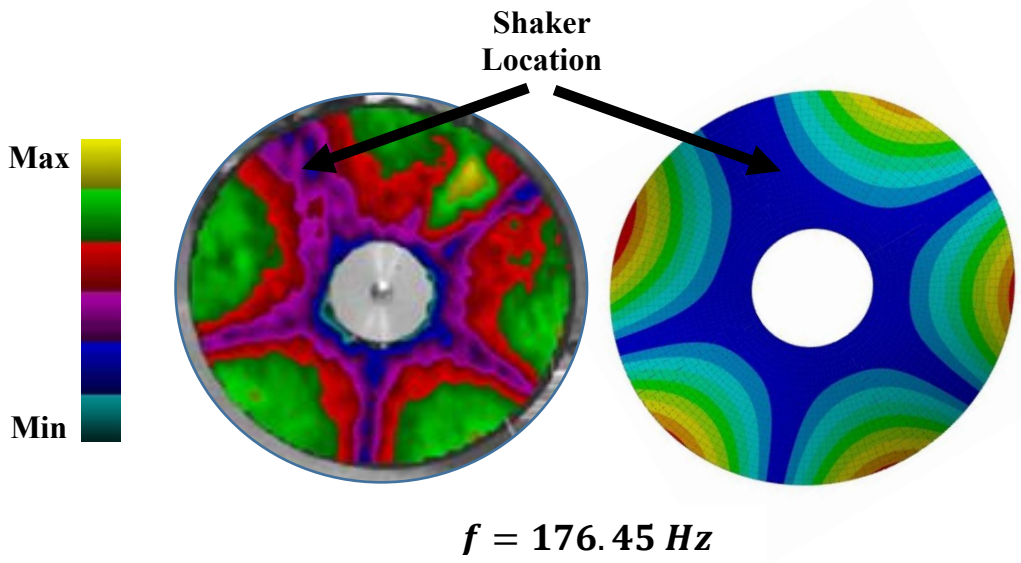

Figure 4.13: Experimental transverse doublet mode n = 3 of the brake disc using laser vibrometer scanner

A laser vibrometer scanner is used to identify the modes of vibration experimentally and Figure 4.13 shows the third transverse doublet mode.

The voltage output of the vibrating piezoceramic patch is measured with a multimeter and is compared with numerical results in Table 4.6 at different frequencies. The piezoceramic voltage output and the energy harvested at different frequencies using *FEM* are displayed in Figures 4.14 and 4.15, respectively.

Table 4.6: Voltage output of vibrating piezoceramic patch attached to a brake disc

	Voltage Output $V_{rms}\ (volt)$	
$f\ (Hz)$	Experiment	*FEM*
110	9.2	8.146
176	6.1	6.672
296	8.14	9.174

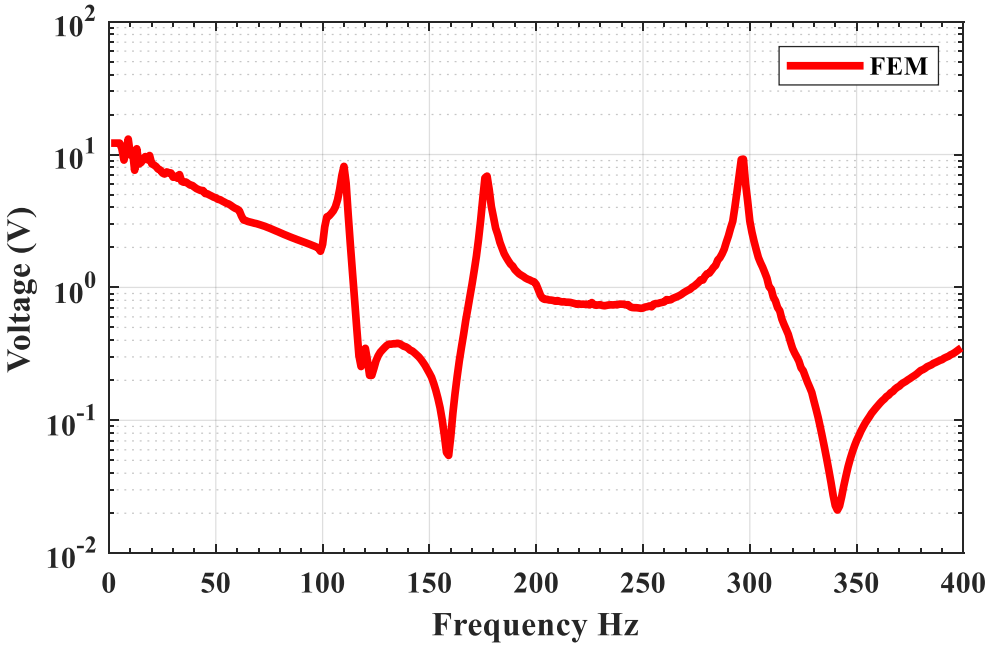

Figure 4.14: Piezoceramic voltage output at different operating frequencies

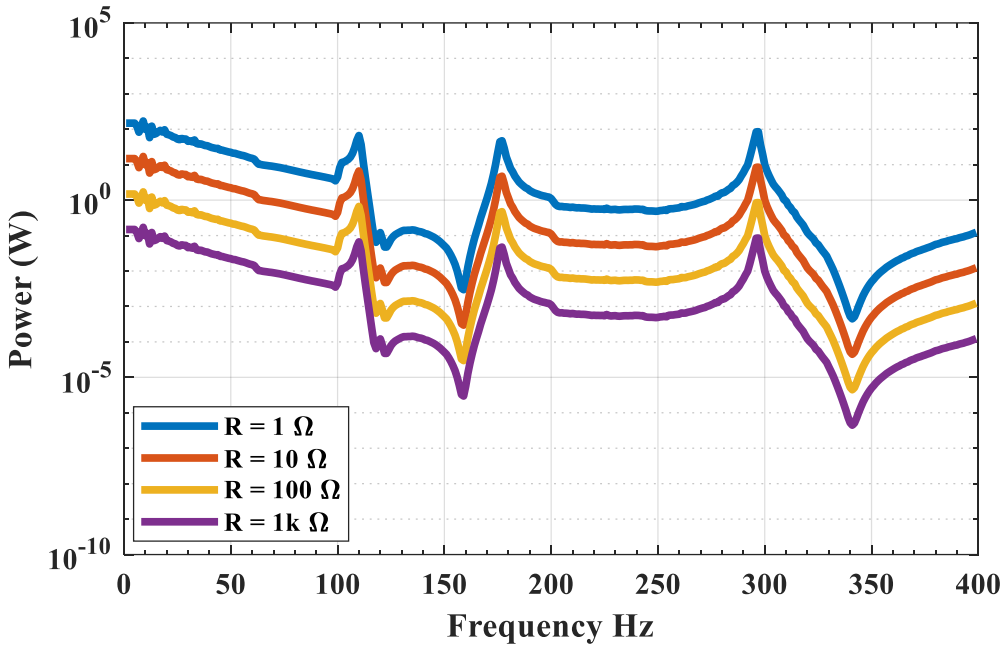

Figure 4.15 : Output power at different shunt resistors

Based on the results presented in section 2.6.2 and Figure 4.9, the dynamic instability and frequency separation occurs at doublet mode n = 3 which is in the frequency range of 150 Hz to 180 Hz. Therefore to enhance the stability of the brake disc, the piezoceramic patch is connected to a resistive shunt which adds damping to the system as was presented in equation (3.68). The output power resulted from connecting the piezoceramic patch to a resistive shunt is shown in Figure 4.16.

The effect of contact pads on one of the transverse doublet modes is depicted in Figure 4.17. The third transverse mode of the new brake disc prototype occurs at frequency of 173 Hz in case (a) whereas in case (b) the brake system exhibits frequency separation due to the effect of pads contact stiffness and the obtained mode has a frequency of 175 Hz.

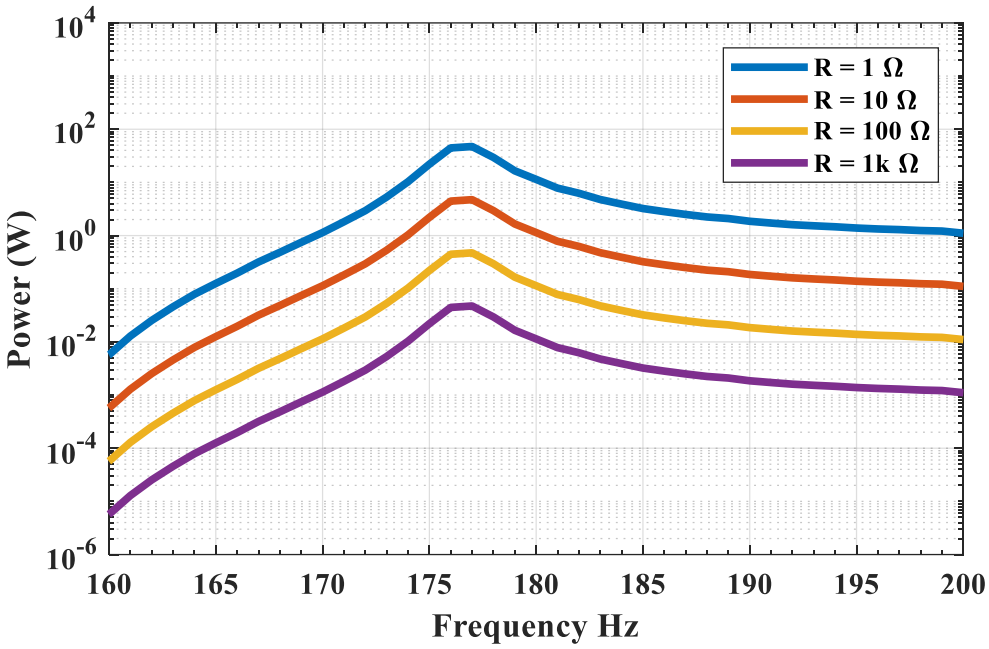

Figure 4.16 : Output power at transverse doublet mode 3

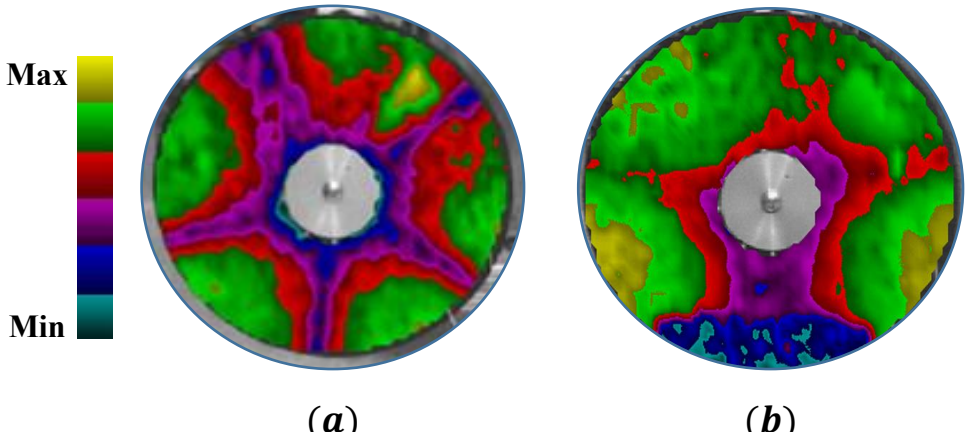

Figure 4.17: Experimental transverse doublet mode n = 3 of the newly proposed disc brake system using laser vibrometer scanner; (a) without contact (b) with contact

4.4 Summary

This chapter has presented an experimental realization of the proposed concept of brake squeal. The experimental dynamic performance characteristics of a laboratory prototype of disc brake system integrated with piezoceramic patch are determined. These characteristics are utilized to validate the predictions of the theoretical finite element model. Furthermore, the experimental results are determined also for conventional disc brake systems in order to provide basis for establishing the merits and effectiveness of the new design in eliminating dynamic instability the system.

It has been demonstrated through the set of experimental results obtained by using prototype of the proposed concept of brake systems with integrated piezoceramic patch that the model is capable of predicting the resonant frequencies, frequency responses and voltage output of the piezoceramic patch very accurately.

Chapter 5: Conclusions and Recommendations

5.1 Overview

This chapter summarizes the conclusions discovered in this dissertation. It also presents recommended ideas, which may be needed to expand the concepts, proposed in this study. Included also in this chapter are the major contributions of the dissertation in relation to the current state-of-the-art.

5.2 Conclusions

The conclusions obtained from both theoretical modeling and experimentation in this dissertation are covered in this section.

The dissertation has presented an approach for determining the brake squeal and its dynamic instability characteristics. The brake system equations are formulated based on an adopted model from the literature and discretized to form *FEM* that is capable of simulating dynamic instability in disc brake systems. The disc brake system is integrated with shunted piezoceramic patch and the *FEM* is modified accordingly in a coupled electromechanical finite element model. The dynamic instability characteristics of the new design are compared with those obtained in conventional disc brake systems. It has been found that the new design broadens the stability range of operation of disc brake systems.

An experimental prototype has been designed and manufactured to produce significant dynamic instability features of conventional disc brake systems. The prototype is then modified by integrating a shunted piezoceramic patch with the brake system. It has been concluded through a set of tests that the adopted disc brake model

is able to correctly predict resonant frequencies of transverse doublet modes as well as the frequency response of each test. The limitations of the adopted model has been demonstrated in one of the tests where the predicted frequency separation range related to the third transverse doublet mode is far from the experimental obtained range.

Shunted piezoceramics have been proposed in the literature to be an alternative to suppress brake squeal. The new design allowed the dissipated energy resulting from integrating shunted piezoceramic patch with the brake system to be harvested. The developed *FEM* is exercised and showed excellent agreement when compared to results obtained from experimental tests.

5.3 Recommendations

This dissertation has attempted to establish the fundamentals governing the operation of a new class of disc brake systems. The process opened up the door for unanswered questions that need to be addressed in future studies. Distinct among these issues is the need to adopt or design a new disc brake model that takes into account the effect of negative friction and the geometry and material properties of the contact pads. This allows the study of disc brakes in contact with brake pads at different angles and to correctly predict the onset of brake squeal. The new model or design should be modified with shunted piezoceramic patches placed at different locations on the disc brake system as in actual discs the space may be limited. Also, the model should study the effect of different shunts on the generated output power. Another natural extension of this work is the study of temperature effects and wear on the operation of disc brake systems with shunted piezoceramics since the braking action results in high temperature which limits the operation of piezoceramics.

More work is needed on the experimental side which can be done by considering an actual disc brake system. This will allow the study of brake squeal noise and to examine the gyroscopic effects on disc brakes.

5.4 Major Contributions of the Dissertation

This dissertation has presented the concept of disc brake systems with shunted piezoceramic networks and their performance characteristics.

The comprehensive presentation of the disc brake systems with shunted piezoceramic networks through mathematical modeling and experimental realization and evaluation emphasizes the following major contributions of the work to the current state-of-the-art of vibration mitigation of brake squeal:

1. The concept of brake systems with shunted piezoceramic networks for simultaneous energy harvesting and energy dissipation is original and has not been considered at all in the open-literature for application to mitigation of disc brake squeal.
2. The comprehensive theoretical and experimental demonstration of the effectiveness of the concept of brake systems with shunted piezoceramic networks in mitigating the brake squeal phenomenon is one of the major contributions of this dissertation.
3. The ability of the brake systems with shunted piezoceramic networks in expanding the stability boundaries of operating without the occurrence of squeal as compared to those of conventional disc brake systems is another important contribution of the dissertation.

5.5 Summary

This chapter has summarized the conclusions discovered in this dissertation. The chapter has included also the major contributions of the dissertation in relation to the current state-of-the-art and possible recommendations for potential directions.

References

[1] A. Papinniemi, J. C. S. Lai and J. Zhao, "Brake squeal: a literature review," *Applied Acoustics,* vol. 63, no. 4, pp. 391-400, 2002.

[2] N. M. Kinkaid, O. M. O'Reilly and P. Papadopoulos, "Automotive disc brake squeal," *Journal of Sound and Vibration,* vol. 267, no. 1, pp. 105-1666, 2003.

[3] D. Dawson, History of Tribology, 2nd Edition ed., Edmunds: Professional Engineering Publishing, 1998.

[4] I. V. Kragelskii, Friction and Wear, London: Butterworths, 1965.

[5] R. A. Ibrahim, "Friction-induced vibration, chatter, squeal, and chaos part I: Mechanics of contact and friction," *Applied Mechanics Reviews,* vol. 47, no. 7, pp. 209-226, 1994.

[6] R. A. Ibrahim, "Friction-induced vibration, chatter, squeal, and chaos part II: Dynamics and modelling," *Applied Mechanics Reviews,* vol. 47, no. 7, pp. 227-253, 1994.

[7] H. Ziegler, Principles of Structural Stability, Waltham, MA: Blaisdell Pub. Co. , 1968.

[8] J. P. Den-Hartog, "Forced vibrations with combined coulomb and viscous damping," *Journal of Applied Mechanics,* vol. 53, no. 9, pp. 107-115, 1931.

[9] M. R. North, "A survey of published work on vibration in braking systems," Motor Industry Research Association (M.I.R.A), 1969.

[10] J. Hulten, "Brake squeal - a self exciting mechanism with constant friction," in *SAE Truck and Bus Meeting,* Detroit, MI, USA, 1993.

[11] M. Eriksson and S. Jacobson, "Friction behavior and squeal generation of disc brakes at low speeds," *Proceedings of the Institution of Mechanical Engineers,* vol. 215, pp. 1245-1256, 2001.

[12] G. X. Chen, Z. R. Zhou, P. Kapsa and L. Vincent, "Expreimental investigation into squeal under reciprocating sliding," *Tribology International,* vol. 36, no. 12, pp. 961-971, 2003.

[13] A. J. Day, M. Tirovic and T. P. Newcomb, "Thermal effects and pressure distributions in brakes," *Proceedings of the Institution of Mechanical Engineers,* vol. 205, pp. 199-205, 1991.

[14] C. Hohmann, K. Schiffner, K. Oerter and H. Reese, "Contact analysis for drum brakes and disk brakes using ADINA," *Computers and Structures,* Vols. 1-3, pp. 185-198, 1999.

[15] M. Tirovic and A. J. Day, "Disc Brake interface pressure distributions," *Proceedings of the Institution of Mechanical Engineers,* vol. 205, pp. 137-146, 1991.

[16] U. von Wagner, D. Hochlenert and P. Hagedorn, "Minimal models for disk brake squeal," *Journal of Sound and Vibration,* vol. 302, no. 3, pp. 527-539, 2007.

[17] N. Hoffmann, M. Fischer, R. Allgaier and L. Gaul, "A minimal model for studying properties of the mode-coupling type instability in friction induced oscillations," *Mechanics Research Communications,* vol. 29, no. 4, pp. 197-205, 2002.

[18] J. O. Hulten and J. Flint, "An assumed modes method approach to disc brake squeal analysis," SAE, Warrendale, PA, 1999.

[19] U. von Wagner, D. Hochlenert, T. Jearsiripongkul and P. Hagedorn, "Active Control of Brake Squeal Via "Smart Pads"," *SAE International,* vol. 113, no. 6, pp. 1186-1192, 2004.

[20] T. Jearsiripongkul and P. Hagedorn, "Active Control of Disk Brake Squeal," in *Conference of Mechanical Engineering Network of Thailand*, Nakhon Ratchasima, Thiland, 2006.

[21] T. Jearsiripongkul and P. Hagedorn, "Parameter Estimation of the Disk in a Floating Caliper Disk Brake Model with respect to Squeal," *Proceedings in Applied Mathematics and Mechanics,* vol. 4, no. 1, pp. 93-94, 2004.

[22] T. Jearsiripongkul and D. Hochlenert, "Disk Brake Squeal: Modeling and Active Control," in *IEEE Conference on Robotics, Automation and Mechatronics*, Bangkok, Thialand, 2006.

[23] D. Hochlenert and P. Hagedorn, "Control of disc brake squeal – modelling and experiments," *Structural Control and Health Monitoring,* vol. 13, no. 1, pp. 260-276, 2006.

[24] D. Hochlenert, G. Spelsberg-Korspeter and P. Hagedorn, "Friction Induced Vibrations in Moving Continua and Their Application to Brake Squeal," *Journal of Applied Mechanics,* vol. 74, no. 3, pp. 542-549, 2007.

[25] G. Spelsberg-Korspeter, O. N. Kirillov, D. Hochlenert and P. Hagedorn, "In- and Out-of-Plane Vibrations of a Rotating Plate With Frictional Contact: Investigations on Squeal Phenomena," *Journal of Applied Mechanics,* vol. 76, no. 4, p. 041006, 2009.

[26] G. Spelsberg-Korspeter, "Eigenvalue optimization against brake squeal: Symmetry, mathematical background and experiments," *Journal of Sound and Vibration,* vol. 331, no. 19, pp. 4259-4268, 2012.

[27] J. Kang, C. M. Krousgrill and F. Sadeghi, "Dynamic instability of a thin circular plate with friction interface and its application to disc brake squeal," *Journal of Sound and Vibration,* vol. 316, no. 1, pp. 164-179, 2008.

[28] J. Kang, C. M. Krousgrill and F. Sadeghi, "Analytical formulation of mode-coupling instability in disc–pad coupled system," *International Journal of Mechanical Sciences,* vol. 51, no. 1, pp. 52-63, 2009.

[29] J. Kang, C. M. Krousgrill and F. Sadeghi, "Comprehensive stability analysis of disc brake vibrations including gyroscopic, negative friction slope and mode-coupling mechanisms," *Journal of Sound and Vibration,* vol. 324, no. 1, pp. 387-407, 2009.

[30] J. E. Mottershead, "Vibration - and Friction-Induced Instability in Disks," *Shock and Vibration Digest,* vol. 30, no. 1, pp. 14-31, 1998.

[31] Q. Cao, H. Ouyang, M. I. Friswell and J. E. Mottershead, "Linear eigenvalue analysis of the disc-brake squeal problem," *International Journal for Numerical Methods in Engineering,* vol. 61, no. 9, pp. 1546-1563, 2004.

[32] H. Ouyang and J. E. Mottershead, "Dynamic Instability of an Elastic Disk Under the Action of a Rotating Friction Couple," *Journal of Applied Mechanics,* vol. 71, no. 6, pp. 753-758, 2004.

[33] J. Kang, "Squeal analysis of gyroscopic disc brake system based on finite element method," *International Journal of Mechanical Sciences,* vol. 51, no. 4, pp. 284-294, 2009.

[34] J. Kang, "Effect of contact area variation on squeal propensity of disc modes," *Journal of Mechanical Engineering Science,* vol. 226, no. 10, pp. 2467-2473, 2012.

[35] J. Kang, "Finite element modelling for the investigation of in-plane modes and damping shims in disc brake squeal," *Journal of Sound and Vibration,* vol. 331, no. 9, pp. 2190-2202, 2012.

[36] J. Kang, "Finite element modeling for stick-slip pattern of squeal modes in disc brake," *Journal of Mechanical Science and Technology,* vol. 28, no. 10, pp. 4021-4026, 2014.

[37] H. Ouyang, W. Nack, Y. Yuan and F. Chen, "Numerical analysis of automotive disc brake squeal: a review," *International Journal of Vehicle Noise and Vibration,* vol. 1, no. 3-4, pp. 207-231, 2005.

[38] P. Hagedorn, M. Eckstein, E. Heffel and A. Wagner, "Self-Excited Vibrations and Damping in Circulatory Systems," *Journal of Applied Mechanics,* vol. 81, no. 10, p. 101009, 2014.

[39] J. Kang, "Automotive brake squeal analysis with rotating finite elements of asymmetric disc in time," *Journal of Sound and Vibration,* vol. 393, pp. 388-400, 2017.

[40] A. Wagner, G. Spelsberg-Korspeter and P. Hagedorn, "Structural optimization of an asymmetric automotive brake disc with cooling channels to avoid squeal," *Journal of Sound and Vibration,* vol. 333, no. 7, pp. 1888-1898, 2014.

[41] P. Bedard, "Comparison test—little cars 6.1," *Car and Driver,* vol. 45, no. 12, pp. 54-81, 2000.

[42] F. Markus, "Road test–2002 Ford Explorer Eddie Bauer 4 x 4," *Car and Driver,* vol. 46, no. 7, pp. 74-78, 2001.

[43] T. Swan, "Comparison test—fanzy panzers," *Car and Driver,* vol. 46, no. 2, pp. 46-59, 2000.

[44] R. A. C. Fosberry and Z. Holubecki, "Interim report on disc brake squeal," Motor Industry Research Association, Warwickshire, England, 1959.

[45] R. A. C. Fosberry and Z. Holubecki, "Disc brake squeal: its mechanism and suppression," Motor Industry Research Association, Warwickshire, England, 1961.

[46] J. D. Fieldhouse, "A proposal to predict the noise frequency of a disc brake based on the friction pair interface geometry," SAE, Warrendale, PA, 1999.

[47] S. K. Rhee, M. G. Jacko and P. H. S. Tsang, "The role of friction film in friction, wear, and noise of automotive brakes," SAE, Warrendale, PA, 1990.

[48] P. DiLisio, R. Parisi, J. Rieker and W. Stringham, "Brake noise resolution on the 1998 Mercedes-Benz M-Class," SAE, Warrendale, PA, 1998.

[49] K. A. Cunefare and A. J. Graf, "Experimental active control of automotive disc brake rotor squeal using dither," *Journal of Sound and Vibration,* vol. 250, no. 4, p. 579–590, 2002.

[50] H. Baba, T. Wada and T. Takagi, "Study on reduction of brake squeal caused by in-plane vibration on rotor," SAE, Warrendale, PA, 2001.

[51] N. W. Hagood and A. von Flotow, "Damping of Structural Vibrations with Piezoelectric Materials and Passive Electrical Networks," *Journal of Sound and Vibration,* vol. 146, no. 2, pp. 243-268, 1991.

[52] S. Behrens, S. O. R. Moheimani and A. J. Fleming, "Multiple mode current flowing passive piezoelectric shunt controller," *Journal of Sound and Vibration,* vol. 266, no. 5, pp. 929-942, 2003.

[53] M. Neubauer, R. Oleskiewicz, K. Popp and T. Krzyzynski, "Optimization of damping and absorbing performance of shunted piezo elements utilizing negative capacitance," *Journal of Sound and Vibration,* vol. 298, no. 1-2, pp. 84-107, 2006.

[54] M. S. Tsai and K. W. Wang, "On the Structural Damping Characteristics of Active Piezoelectric Actuators with Passive Shunt," *Journal of Sound and Vibration,* vol. 221, no. 1, pp. 1-22, 1999.

[55] D. Hochlenert, G. Spelsberg-Korspeter and P. Hagedorn, "A note on safety-relevant vibrations induced by brake squeal," *Journal of Sound and Vibration,* vol. 329, no. 19, pp. 3867-3872, 2010.

[56] M. Neubauer and R. Oleskiewicz, "BRAKE SQUEAL SUPPRESSION WITH SHUNTED PIEZOCERAMICS - A CONTROL FORMALISM," *IFAC Proceedings,* vol. 39, no. 16, pp. 520-525, 2006.

[57] M. Neubauer and R. Oleskiewicz, "Brake squeal control with shunted piezoceramics – efficient modelling and experiments," *Journal of Automobile Engineering,* vol. 222, no. 7, pp. 1141-1151, 2008.

[58] M. Neubauer and R. Oleskiewicz, "Suppression of Brake Squeal Using Shunted Piezoceramics," *Journal of Vibration and Acoustics,* vol. 130, no. 2, p. 021005, 2008.

[59] S. S. Rao, Vibration of Continuous Systems, Hoboken, NJ: Wiley, 2007.

[60] J. N. Reddy, Energy Principles and Variational Methods in Applied Mechanics, Hoboken, NJ: Wiley, 2002.

[61] M. D. Olson and G. M. Lindberg, "Annular and circular sector finite elements for plate bending," *International Journal of Mechanical Sciences,* vol. 12, no. 1, pp. 17-33, 1970.

[62] T. B. Gabrielson, "Frequency constants for transverse vibration of annular disks," *Journal of the Acoustical Society of America,* vol. 105, no. 6, pp. 3311-3317, 1999.

[63] R. D. Blevins, Formulas for natural frequency and mode shape, New York: Van Nostrand Reinhold Co., 1979.

[64] I. Chopra and J. Sirohi, Smart Structures Theory, New York, NY: Cambridge University Press, 2014.

[65] A. Erturk and D. Inman, Piezoelectric Energy Harversting, Chichester: John Wiley & Sons, Ltd, 2011.